Molecular Simulation of Adsorption and Diffusion in a Microporous Carbon Membrane

Alexandre Manuel Vieira Linhares

Institute for Material and Processes
School of Engineering and Electronics
The University of Edinburgh

Thesis submitted for the degree of Doctor of Philosophy

October 2003

Abstract

Increasingly the recovery of hydrogen from refinery gases represents an important operation in the oil & gas industry, particularly as hydrogen is being seen as an energy of the future. Membrane separations are an economic alternative to either pressure swing adsorption separations or cryogenic separations. Transport across thin membranes can produce chemical and physical separations at a relatively low cost. Thus, the diffusion of gas mixtures inside a porous material is an important factor in membrane separations. This research involves the mathematical modelling of adsorption and diffusion in microporous carbon membranes and particularly the Selective Surface Flow (SSF) carbon membranes developed by Air Products and Chemicals, Inc. Molecular simulations are used to predict the performance of the SSF membranes for hydrogen/hydrocarbon mixture separation under realistic conditions of temperature, pressure and bulk-gas composition. Non-Equilibrium Molecular Dynamics (NEMD) gives a fully rigorous account of the dynamics of adsorption and diffusion at an atomic level, by integrating the equations of motion of adsorbed molecules interacting with each other, and with the surface, according to specified intermolecular potentials. In our NEMD simulations, it is assumed that all the pores in the membranes are identical, unconnected and open to the surface. However, this single-pore assumption is unlikely to occur in a real material. A real membrane contains pores of different sizes, connected together in a pore network, allowing the possibility of connectivity effects that are not accommodated by a single-pore model. Thus, critical path analysis (CPA) is used to characterise the pore network structure. The CPA shows that species are selectively transported through essentially distinct sub-networks within the pore network of the membrane. The simulation results are compared with experimental permeabilities, obtained from the Air Products, for a mixture of hydrogen/methane relevant to *e.g.* the recovery of hydrogen from catalytic reformer offgas.

Declaration

The work presented in this thesis was carried out in the School of Engineering and Electronics, The University of Edinburgh. It is the original work of the author except where acknowledged in the text. This thesis was composed by the author and was not submitted in any form at another university.

Acknowledgements

I would like to thank my supervisor Nigel Seaton for all his excellent advice, trust and for his continued encouragement throughout all these years and for the highly challenging technical discussions relating to this thesis. Thanks are also due to Tim C. Golden, James M. D. MacElroy and Madhukar B. Rao for useful discussions.

I would like to thank Tim Golden and Catherine Golden for their warm welcome and support during my visit to Allentown. Many thanks my all my friends who provided a strong support throughout these years, in particular Lurdes Ferreira-Valado in Manchester, and all the members of Nigel's research group. Finally, special thanks to those that had the patience to proof-reading this thesis and for all their suggestions: Lurdes Ferreira-Valado and Paul A. Smith.

I would like to thank to Air Products and Chemicals, The Edinburgh University, The Royal Academy of Engineering and the Fundação Calouste Gulbenkian for their financial support of my Ph.D. and conference attendance.

Last, but not least, I would like to express my eternal gratitude to my family for always being there and for always believing in me.

Table of Contents

1. Introduction

Refinery off-gas streams that are currently flared or burned as low-grade fuel are a potentially viable source of hydrogen because industry is still not focused on the production or use of hydrogen as an energy carrier or a fuel for energy generation. The demand for hydrogen is increasing rapidly due to changes in government regulations affecting refiners. Hydrogen is a clean and affordable energy source with a low environmental impact. Thus, recovery of hydrogen from refinery off-gas for reuse as a higher value product is an opportunity for providing increased productivity, energy savings and reduced waste. One of the most promising uses of hydrogen is as a fuel for fuel cells for applications such as power generation and transportation. Present technologies for hydrogen recovery include pressure swing adsorption (PSA), cryogenic separation and membrane separation. All these three processes are efficient for high-hydrogen-content and high-pressure feeds, but are not efficient for low hydrogen content and low-pressure feeds. For PSA, the inefficiency is partly due to the fact that the absorbents, which include molecular sieves and activated carbons, preferentially adsorb the heavy impurities (Heung, 2003). Cryogenic separation is impeded by poorer reliability and flexibility and requires significant feed pre-treatment (Whysall & Picioccio, 1999). Transport across thin membranes can produce chemical and physical separations at a relatively low price. These lower costs were the impulse for a rapid development of membrane technology over the last decades. Nowadays, industry demands better quality separation membranes with characteristics such as high fluxes and high selectivities (Seader & Henley, 1998). To separate effectively a mixture, a membrane must possess both high permeability and a high selectivity.

1.1 Mass Transport Mechanisms across Membranes

Mass transfer of a gas though a porous material can involve several processes, depending on the nature of the pore structure and the solid. Porous membranes are

classified as microporous and macroporous according to their porous structure. However, only the first type of porous membrane is selective. The pore size, and therefore the diffusion of fluid mixtures inside a porous material, is an important factor in membrane separations. The relative importance of macropore and micropore diffusion depends on the pore size distribution within the membrane. Micropores have diameters smaller than 20 Å; macropores have diameters greater than 500 Å and mesopores are in the size range 20 - 500 Å (Gregg & Sing, 1982). Macroporous materials are widely used as a support for thin microporous membranes (see Figure 1.1). This macroporous layer provides support and mechanical resistance to the membrane and gives a high flux. On the other hand, the microporous layer (a few micrometers thick) gives high selectivity but a low flux. Thus, the resulting flux rate is controlled by the permeance of the thin selective skin (Seader & Henley, 1998).

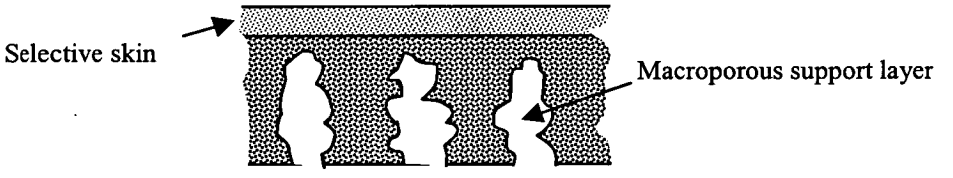

Figure 1.1 – Porous membrane schematic representation.

According to Seader & Henley (1998) and Cussler (1997) five different basic transport mechanisms can occur in a microporous membrane:

(a) If the pore diameter is large compared to the molecular diameter and a pressure gradient is present, convective flow through the pores occurs (as shown in Figure 1.2a). Such flow is generally undesirable because it is not selective and is characterised by bulk or free molecular diffusion. Here, molecule/molecule collisions are dominant over molecule/wall collisions.

(b) If the total pressure is constant on both sides of the membrane but a chemical potential gradient is present across the membrane, selective diffusion will occur (see Figure 1.2b). When the mean free path of the molecular species is much larger than the pore diameter, Knudsen diffusion becomes predominant. Here, molecule/wall collisions are dominant.

(c) If one of the mixture components is more strongly adsorbed onto the pore surface, the surface diffusion of these species becomes dominant (see Figure 1.2c). This mechanism of transport is normally dominant for micropores.

(d) If the partial pressure in the pore of one component is greater that its saturation pressure this species will condense resulting in the exclusion of the others species (see Figure 1.2d).

(e) If the pores are of the same order as the molecular size for at least one of the components (as for example in a carbon molecular sieve) the diffusion of those components will be restricted as shown in Figure 1.2e, resulting in an improved separation. Molecules with diameter larger than the pores are stopped from diffusing into the pores.

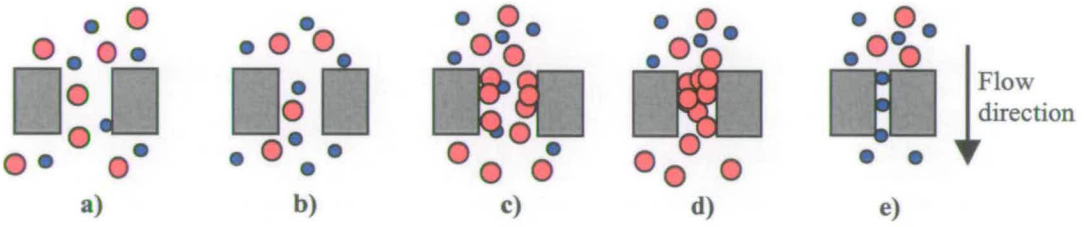

Figure 1.2 – Mechanisms of mass transport in membranes: (a) Bulk flow; (b) Diffusion through the pores; (c) Surface diffusion; (d) Partial condensation; (e) Molecular sieving

In this thesis, we have particular interest in the hydrogen recovery from a hydrogen/hydrocarbon refinery waste mixture. Typical catalytic reformer off-gas hydrogen compositions are between 65 % and 80 % (Yang, 1987) and many off–gas streams containing hydrogen up to 50% are discarded for economic reasons. Hydrocarbons adsorb more strongly than hydrogen on carbons due to their high molecular weight. Thus, the third mechanism is the most attractive because of the selective adsorption of hydrocarbons. According to Sedigh *et al.* (1999), carbon membranes have been studied in the last few years as a promising alternative to both inorganic and polymeric membranes. Carbon membranes are in general prepared by

the carbonisation of polymeric precursors in an inert atmosphere. These membranes have been shown to have, for many commercially interesting separations, similar or higher selectivity than polymeric membranes and high permeabilities, comparable to those reported with microporous inorganic membranes (Sedigh *et al.*, 1999). These characteristics make them potentially attractive for an increasing number of industrial applications (Rao & Sircar, 1993b; Sircar, Rao Thaeron, 1999; Sedigh *et al.*, 1999). Selective adsorption of the more strongly adsorbed components of a gas mixture onto the pore surface followed by surface diffusion of the adsorbed molecules across the pore provides the most flexible and attractive choice for practical hydrogen/hydrocarbon gas separations (Sircar & Rao, 1993b). The separation selectivity is determined by preferential adsorption of certain components of the gas mixture on the surface of the membrane pores, as well as by selective diffusion of the adsorbed molecules. Both the pore size and the physicochemical nature of the pore surface play important roles in determining the separation efficiency of these membranes. Furthermore, the properties of these membranes may be adjusted by appropriate methods to a particular separation (Sircar & Rao, 1993b). Thus, the pore size can be adjusted to maximise the interaction with the larger molecule. Then, this species is preferentially adsorbed and blocks the access of the smaller molecules to the pore structure.

1.2. Selective Surface Flow Membranes

In 1993, Rao & Sircar (1993a, 1993b) published two papers in which they presented data for hydrogen/hydrocarbon separation using a novel carbon nanoporous membrane – the Air Products Selective Surface Flow (SSF) membrane. This membrane separates by selective adsorption followed by surface diffusion of the more strongly adsorbed species. Thus, from a mixture of hydrocarbons and hydrogen the hydrocarbons are preferentially adsorbed and the hydrogen is enriched on the feed side (Rao & Sircar, 1993b) and can subsequently be purified to a high purity H_2 stream using a PSA purification system (see, *e.g.*, Sircar & Golden, 2000). This is a distinct advantage of the SSF membrane because the desired product

(hydrogen) is produced at feed pressure, avoiding recompression. The separation mechanism of an SSF carbon membrane differs from that of a molecular sieving membrane, in which the separation is based on molecular size differences (see, *e.g.*, Koresh & Soffer, 1987), and the small hydrogen molecules pass preferentially through the small pores of the membrane to the effluent side. The SSF separation mechanism imparts separation properties not achievable in conventional glassy polymer membranes that are more widely used (Anand & Ludwig, 1996). According to Anand (1995), first-pass economics demonstrated that the overall cost for hydrogen production is reduced by 35 % versus on-purpose production of hydrogen by steam methane reforming. The hydrogen recovery process using the SSF membrane results in at least 15 % energy reduction and a significant decrease in CO_2 and NO_X emissions.

1.2.1 Preparation of the SSF Membrane

The SSF membrane studied by Rao and Sircar was produced by i) coating the bore side of an aluminium oxide tube with a thin layer of an aqueous emulsion of polyvinylidene chloride (*i.e.* latex); ii) drying the coat under an inert atmosphere; and iii) heating under a N_2 purge to 600 °C – 1000 °C to carbonise the polymer (Rao, Sircar & Golden, 1992). The process is repeated to add the desired number of layers. The porous structure in the membranes is formed during thermal treatment in an atmosphere of inert gas, due to small gas molecules channelling their way out of the solid during the pyrolysis (Rao & Sircar, 1993b; Rao, Sircar & Golden, 1992). Under suitable activation conditions, the porous structure of the membrane can be further developed to a functional separation layer with open micropores, or a support structure with macropores, depending on the oxidation conditions in the activation process (Shusen, Meiyun & Zhizhong, 1996). Rao, Sircar & Golden (1995) observed that increasing the oxidation time of an SSF membrane produces an increase in the permeabilities of all components, and a variation in the kinetic selectivity (*i.e.* the ratio of permeabilities). A gradual increase in pore size can be achieved by carefully controlling the oxidation at an elevated temperature (Soffer,

Koresh & Saggy, 1987), allowing the pore size to be optimised for a particular separation. On the other hand, excessive oxidation steps may excessively enlarge the pore size, leading to increased hydrogen transport and a reduction in selectivity.

1.2.2 Characterisation of the SSF Membrane

In their early work, Rao & Sircar (1993b, 1996) estimated a pore size of between 5 Å and 6 Å by comparing the experimental diffusivity of nitrogen and methane in the SSF membrane with data for activated diffusion of these species in zeolites. Table 1.1 shows a compilation of experimental pore sizes published by Air Products and Chemicals (Rao & Sircar, 1993a, 1993b, 1995).

Table 1.1 – SSF experimental pore size reported by Air Products and Chemical Inc.

Method used	Pore size (Å)	Reference
Nitrogen diffusivity [1]	5 – 6	Rao & Sircar (1993a)
N_2 and CH_4 diffusivities [1]	5.0 – 5.25	Rao & Sircar (1993b)
Atomic Force Microscopy [2]	5.3	Rao & Sircar (1995)
Scanning Tunnelling Microscopy [2]	4.5	Rao & Sircar (1995)
Methane diffusivity [1]	5.5 - 6.5	Rao & Sircar (1995)

[1] By comparing with diffusion in zeolites.

[2] Direct microscopic measurement

To estimate the pore size distribution (PSD) of the SSF membrane Rao & Sircar (1995) empirically fitted the SSF methane diffusivity to the methane diffusivity on zeolites (where the pore size is known). Figure 1.3 shows the PSD, approximated to a normalised gamma distribution, $f(w)$, reported by Rao & Sircar (1995). Their results show a very narrow PSD centred at 6 Å.

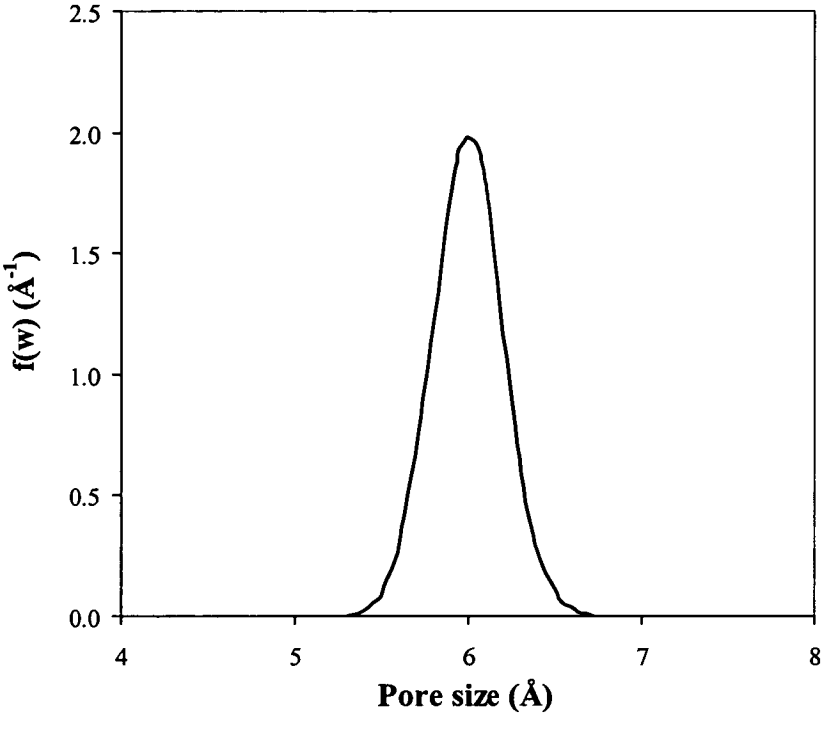

Figure 1.3 - Experimental pore size distribution reported by Air Products (adapted from Rao & Sircar, 1995).

Figure 1.4 shows the variation of selectivity and permeabilities (Golden, 2002; Rao & Sircar, 1993a, 1993b; Rao, Sircar & Golden, 1992) with the feed-side pressure, at a fixed temperature (295.1 K) and product-side pressure (1.7 bar) for a feed mixture of 50 % hydrogen/ 50 % methane. The kinetic selectivity decreases with increasing pressure. This is a clear contrast to what one would expect on the basis of pure-gas adsorption since methane is the more strongly adsorbing component; at higher pressure more methane should be absorbed, leading to higher selectivity.

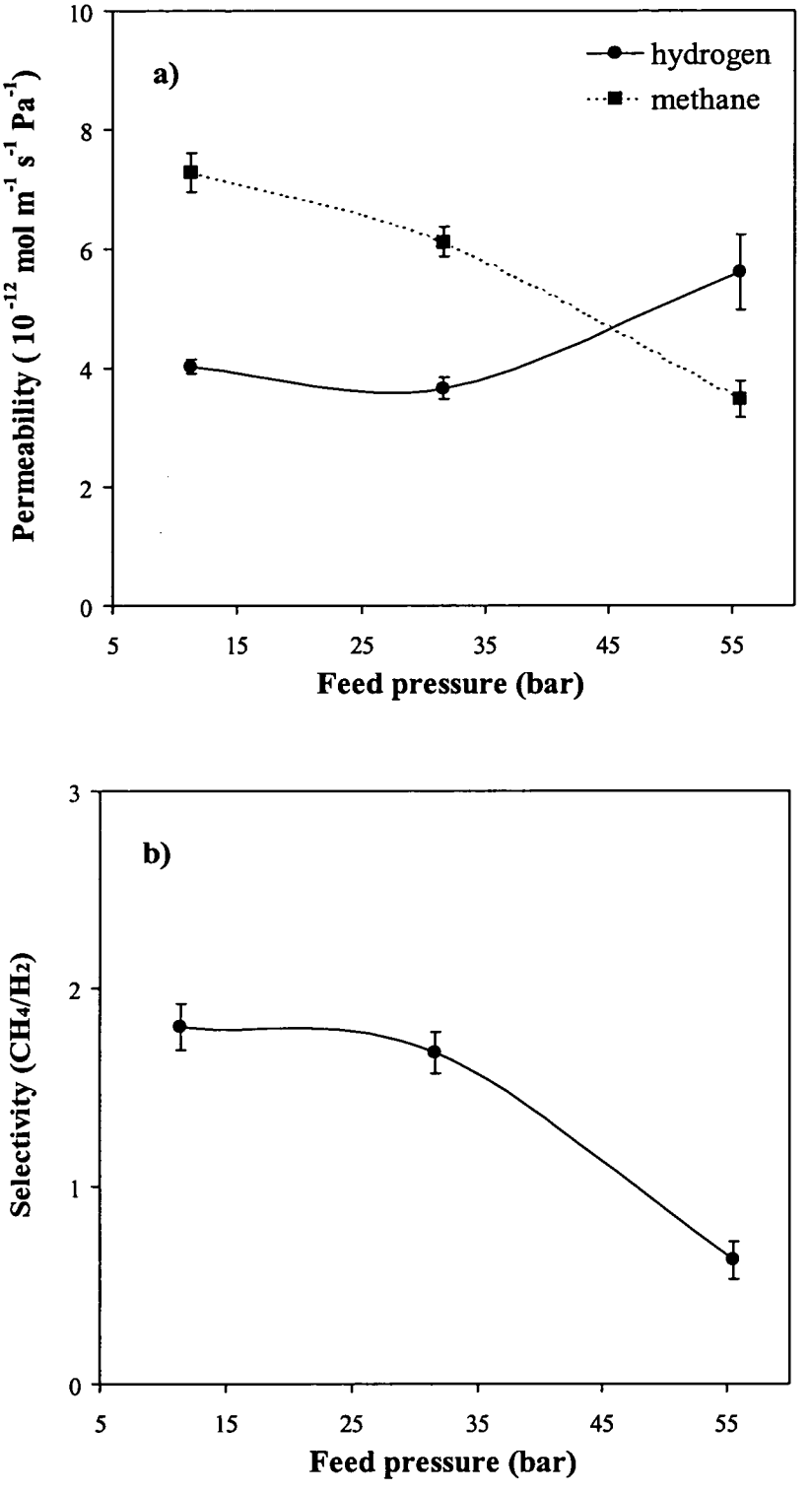

Figure 1.4 - Experimental SSF results: a) permeabilities and b) selectivity (Golden, 2002). Feed composition 50 % hydrogen/ 50 % methane, temperature 295.1 K and permeate pressure 1.7 bar.

Rao, Sircar & Golden (1995) looked at the influence of increasing the pore size, by means of oxidation, on permeability and selectivity, and found that the permeability increased with increasing oxidation time, and thus with increasing pore width, while the selectivity showed a maximum as a function of oxidation time (see Figure 1.5). The dependence of the selectivity on small variations in pore size is supported by observations (Rao, Sircar & Golden, 1992) of significant variations in selectivity between different batches of the same membrane material. This is illustrated by Figure 1.6, which shows that the pure component permeability varies by 20 % for hydrogen and 45 % for methane.

The following conclusions may be drawn from these experimental results:

i) high pressures (*i.e.* above 30 bar) causes the selectivity to fall to about half its value at 11.3 bar;

ii) there is a maximum in the separation selectivity as a function of the pore size.

These conclusions are the starting point and motivation of this research. The goal of this thesis is to identify the parameters that affect the separation performance of an SSF carbon membrane by using simulations at molecular level.

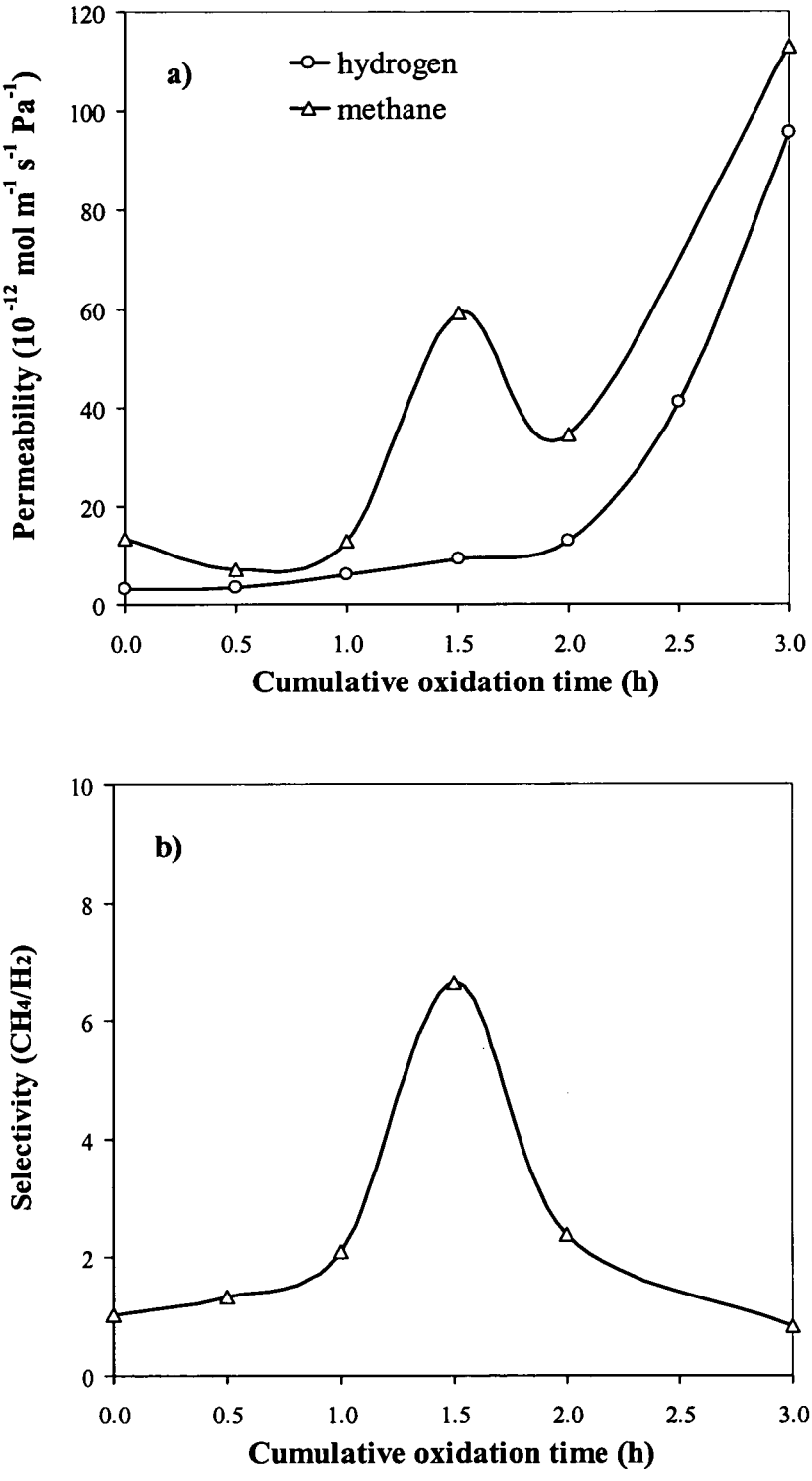

Figure 1.5 - Variation of the methane/hydrogen a) permeabilities and b) selectivity with the cumulative oxidation time, adapted from Rao, Sircar & Golden (1995). Feed pressure 4.5 bar, effluent pressure 1.1 bar, temperature 294 K.

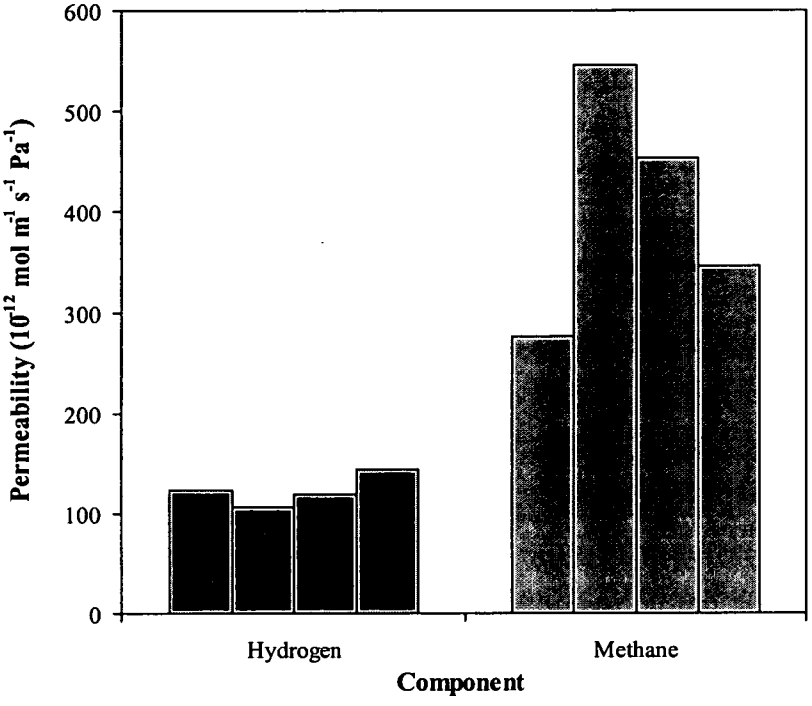

Figure 1.6 – Pure gas permeabilities in four different SSF membranes measured at 295 K and 1.83 bar on the high pressure side. Adapted from Rao, Sircar & Golden (1992).

1.2.3. Molecular Simulations of Adsorption and Diffusion in SSF Membranes

Molecular simulations have been widely used to study adsorption (*e.g.* Darkrim & Levesque, 1998; Davies, 1999; Nicolson & Cracknell, 1996), equilibrium diffusion (*e.g.* Cracknell, Nicholson & Gubbins, 1995; Nicholson, 1998a) and transport diffusion (*e.g.* MacElroy & Boyle, 1999; Nicholson, 1997; 1998a; 1998b, Travis & Gubbins, 2000) in porous materials. For example, Davies & Seaton (1999) have successfully applied Grand Canonical Monte Carlo simulation to characterise carbon adsorbents and to predict adsorption in these materials. Meanwhile, Thompson, Ford & Heffelfinger (1998) and McElroy & Boyle (1999) showed that Grand Canonical Molecular Dynamics (GCMD) simulation is a method suitable to describe some important industrial applications (*e.g.* membrane separations, diffusion in catalysts

and some adsorption processes) because of the presence of gradients of chemical potential (*i.e.* gradient of concentration or partial pressure) that exists across the material.

Since the publication of the first results by Rao & Sircar (1983a, 1993b), several authors have carried out molecular simulations of transport in membranes of this type. Furukawa & Nitta (1997) and Furukawa, Shigeta & Nitta (1996) studied the influence of pore width on methane/ethane permeation for both pure components and their mixture. Their simulated fluxes are very much larger than experimental values estimated from the permeabilities reported by Rao & Sircar (1993b). In a later paper, Furukawa, Hayashi & Nitta (1997) removed atoms from the surface carbon layer, and demonstrated that the permeability decreases with increasing heterogeneity. However, these permeabilities are still three orders of magnitude larger than experimental values. MacElroy & Boyle (1999) and MacElroy (2000) simulated the separation of methane and hydrogen in a single pore of width 7.5 Å by non-equilibrium molecular dynamics. They reported good qualitative agreement with experimental data for relative pure-gas permeabilities, although simulated absolute permeabilities were a few orders of magnitude higher than the experimental values. Seo, Kum & Seaton (2002a) obtained semi-quantitative agreement with published experimental data by using a dynamic Monte Carlo simulation method to calculate the relative rates of diffusion of hydrocarbons and hydrogen. [Because a dynamic Monte Carlo simulation, unlike a molecular dynamics simulation, does not have fully realistic dynamics, the absolute permeabilities could not be calculated.] In that paper experimental selectivities for all five components were bounded between two pore widths (12 Å and 14 Å). Seo, Kum & Seaton (2002b) subsequently used the united-atom model, which represents each methyl or methylene group in alkane chain as a single Lennard-Jones site, to describe the interaction between the hydrocarbons to refine their previous results. The calculated pure-gas permeability ratios at 14 Å pore width were in good agreement with the experimental data.

However, the results presented by those authors are described in terms of a single-pore model and the assumption that all pores are open to the surface is unlikely to

occur in a real material. A real membrane contains pores of different sizes, connected together in a pore network, allowing the possibility of connectivity effects that are not accommodated by a single-pore model. The pore network connectivity is a measurement of the internal topology of the material. It accounts for the fact that the pores in a real pore network are interconnected. The connectivity of a pore network can be quantified in terms of the mean co-ordination number, which is the average number of pores that meet at each pore intersection. Liu & Seaton (1994) and Seaton (1991) have developed a method to estimate the mean coordination number for mesoporous materials based on equilibrium adsorption measurements and concepts of percolation theory. A method to estimate the mean coordination number of microporous materials was later proposed by López-Ramón *et al.* (1997). The effect of the pore network connectivity in gas separation can be investigated by using *e.g.* the critical path analysis (CPA) of Ambegaokar, Halperin & Langer (1971).

1.3 Outline of the Thesis

This research involves the mathematical modelling, at molecular level, of adsorption and diffusion in microporous carbon materials and in particularly the SSF membrane. Carbon porous materials (*e.g.* activated carbons or carbon membranes) have a complex, interconnected pore network of pores of different sizes. Due to computer limitations, our molecular simulation analyses are confined to a single pore size of varying width for each simulation (because to compute directly adsorption and diffusion in even a simple pore network, one would take an extremely large amount of computer resources). In order to understand the mechanism behind mass transport in porous media, one must first understand the mechanism of mass transport in a single pore. Once one has understood these basic mechanisms, the behaviour of, in our case, the membrane can be predicted using a distribution of different pore sizes.

Figure 1.7 illustrates the applicability of molecular simulations to the understanding of the fundamentals of separation processes. Our molecular simulations provide

information about adsorption and diffusion in a single pore (*i.e.* a pore that is considered to be independent of the remaining pores). Since we are looking locally at individual pores, our simulations are independent of the overall structure of material. Connectivity effects relate the single pore properties with the pore network characteristics of the studied material (*e.g.* either an activated carbon or a carbon membrane), described by a pore size distribution.

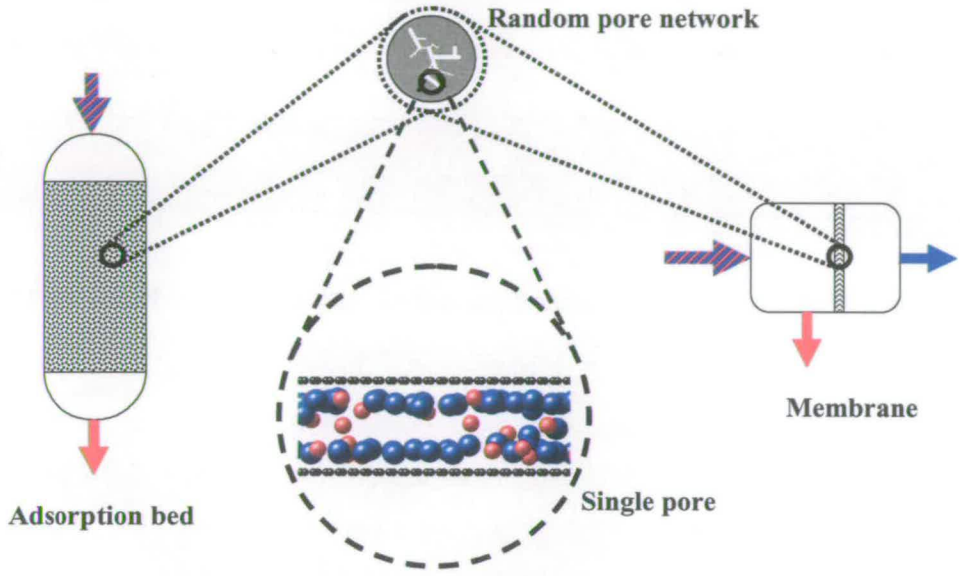

Figure 1.7 – Illustration of the applicability of single pore simulations onto separation processes.

Molecular simulation methods are used to predict the performance of carbon membranes for hydrogen/hydrocarbon mixture separation under realistic conditions of temperature, pressure and bulk gas composition. The remainder of this thesis is organised as follows:

- Chapter Two deals with molecular simulations and describes both the simulation model and algorithms used.
- Simulated adsorption and diffusion results are presented and discussed in Chapter Three. The concepts presented in this chapter are related to the theoretical

understanding of the fundamental characteristics of adsorption and diffusion in porous materials in general.

- In Chapters Four and Five, we compare our simulated permeability and selectivity results with experimental data obtained from Air Products. Pore network connectivity effects – *i.e.* the way in which pores in a pore network are interconnected - are addressed in Chapter Five.
- Chapter Six draws overall conclusions from this investigation and highlights important aspects that need to be considered in order to continue further this investigation.

The material contained in this thesis is in the process of being published. The relevant articles are:

Vieira-Linhares, A. M. & Seaton, N. A. (2002). Simulation of multicomponent diffusion in microporous carbon membranes. In: Kaneko, K., Kanoh, H. & Hanzawa, Y. (2002). *Fundamentals of Adsorption 7.* Chiba: IK International., pp 410-417.

Vieira-Linhares, A. M. & Seaton, N. A. (2003). Non-equilibrium molecular dynamics simulation of gas separation in a microporous carbon membrane. *Chemical Engineering Science*, 58 (18), 4129-4136.

Vieira-Linhares, A. M. & Seaton, N. A. Pore network connectivity effects on gas separation in a microporous carbon membrane. Submitted to the *Chemical Engineering Science.*

2. Simulation Methods

In this chapter, simulation methods are presented to calculate equilibrium adsorption, equilibrium diffusion and transport diffusion. The pore model and intermolecular potential are also presented. Equilibrium adsorption and diffusion can be calculated, in the absence of gradients of pressure, or concentration, by using two standard methods: Grand Canonical Monte Carlo (GCMC) and Equilibrium Molecular Dynamics (EMD), respectively. Several authors have used these two algorithms with satisfactory results for a wide range of cases. In Molecular Dynamics, the molecular positions are obtained by numerically solving Newton's equations of motions, while in Monte Carlo simulations, the positions are generated stochastically and are not temporally dependent. However, GCMC and EMD by themselves have practical limitations - they fail to describe some important industrial applications because of the presence of gradients of pressure or concentration: systems such as membranes, catalysts and some adsorbents cannot be described with conventional algorithms (Thompson, Ford & Heffelfinger, 1998; McElroy & Boyle, 1999). Dual Control Volume Grand Canonical Molecular Dynamics (DCV-GCMD) is uniquely suited for these systems as it can describe both transport (flow and diffusion) and equilibrium adsorption. DCV-GCMD is a combination between GCMC and EMD methods.

2.1 Monte Carlo

Monte Carlo (MC) is a method of calculating, for example material properties, using a random sampling. The use of MC methods to model physical problems allows us to examine more complex systems than we otherwise could. For example, solving equations that describe the interactions between two molecules is fairly simple; solving the same equations for a system of hundreds or thousands of molecules is impossible (because there is no analytical solution). The MC approach is based on

the concept of an ensemble of microstates. [A microstate is a system where all molecular positions and momenta are defined and an ensemble is defined as a collection of a large number of microstates (McQuarrie, 1976).] On the other hand, statistical mechanics provides a link between macroscopic properties measured in experiments and those calculated during simulations. Different ensembles are obtained by keeping different thermodynamic variables fixed. The most widely used ensembles are (see *e.g.*, Frenkel & Smit, 1996):

i) the microcanonical ensemble, in which the number of molecules, the energy and the volume are kept constant;
ii) the canonical ensemble, in which the number of molecules, the temperature and the volume are kept constant;
iii) the grand canonical ensemble, in which the chemical potential, the volume and the temperature are kept constant.

The choice of the ensemble depends thus on the thermodynamic properties of interest and also on the system studied. As will be shown next, the grand canonical ensemble is the most suitable to describe adsorption problems.

2.1.1 Grand Canonical Ensemble

In the grand canonical Monte Carlo ensemble (GCMC) the chemical potential, μ, the volume, V, and the temperature, T, are fixed. The system is open and isothermal and both the energy and the number of particles are free to fluctuate. This is the same as having a constant volume in contact with an infinite bath (at constant temperature) with which it can exchange matter and energy (see Figure 2.1). This reservoir imposes constant temperature and chemical potential on the system.

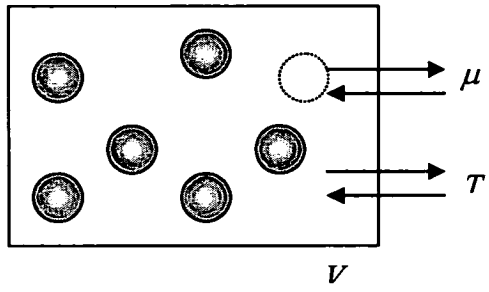

Figure 2.1 – Schematic representation of the grand canonical ensemble.

A microstate is a closed and isothermal system of $\mathcal{N}$ molecules, of volume V in contact with a large bath at temperature T. The probability $\mathcal{P}_i$ of finding a particular microstate i is given by (Hill, 1962):

$$\mathcal{P}_i = \frac{1}{\Xi} e^{-\beta E_i[\mathcal{N},V]} \cdot e^{\beta \mu_i \mathcal{N}_i} \tag{2.1}$$

where N_i and E_i is the number of molecules and the energy of the microstate respectively, $\beta = \frac{1}{k_B T}$ and k_B is the Boltzmann constant. Ξ is the grand partition function (*i.e.* the sum of all possible microstates) given by

$$\Xi = \sum^{microstates} e^{-\beta E_i[\mathcal{N},V]} \cdot e^{\beta \mu_i \mathcal{N}_i} \tag{2.2}$$

If the system is observed for an infinite time it will go through all possible microstates. A basic postulate of statistical mechanics says that the time averaging of one macroscopic property can be replaced by an ensemble average (Hill, 1962). Thus, to calculate the macroscopic property, $\mathcal{M}_{observed}$, one must average the product of that microstate property $\mathcal{M}$ and its microstate probability over all possible microstates,

$$\mathcal{M}_{observed} = \langle \mathcal{M} \rangle = \sum_{i}^{microstates} \mathcal{M}_i \mathcal{P}_i \tag{2.3}$$

where $\langle \mathcal{M} \rangle$ is the ensemble average of the property $\mathcal{M}$ over all microstates. Thus, for this method it is necessary to generate a new system for each microstate. The generation of new a microstate may be infeasible for large dense systems because of the increasing number of unphysical microstates produced.

Metropolis et al (1953) recognising than the generation of the new microstate may be unfeasible in dense systems, proposed an alternative technique based on the "importance of sampling". This technique is archived by generating a Markov Chain of microstates. The Markov Chain mainly implies that any new state should depend only on the previous one and must be microscopically reversible - the probability for the microstate to evolve forward must be the same as if it goes backwards.

The microstate probability given by Equation 2.1 uses quantum statistical mechanics. The classical equivalent of a microstate probability is referred to as the density probability, ρ_i. This density probability is obtained by replacing the summation in Equation 2.1 with an integral over all microstates. For a grand canonical ensemble of microstates of a system that contains a single adsorptive, the density probability of observing a microstate is given by (Nicholson & Parsonage, 1982):

$$\rho_i[\mathbf{r}] = \frac{1}{\Xi} \cdot \frac{1}{\mathcal{N}_i!} V_i^{\mathcal{N}_i} e^{\beta \mu_i \mathcal{N}_i} \Lambda_i^{-3\mathcal{N}_i} e^{-\beta U_i[\mathbf{r}]} \tag{2.4}$$

and for a multicomponent mixture,

$$\rho_i[\mathbf{r}] = \frac{1}{\Xi} \cdot \prod_{j=1}^{n} \left(\frac{1}{\mathcal{N}_j!} V^{\mathcal{N}_j} e^{\beta \mu_j \mathcal{N}_j} \Lambda_j^{-3\mathcal{N}_j} \right) e^{-\beta U_i[\mathbf{r}]} \tag{2.5}$$

where, $U_i[\mathbf{r}]$ is the potential energy which only depends on the positions of the molecules ($\boldsymbol{r}$) and Λ_i is the Broglie thermal wavelength. The Broglie wavelength can be related to the fugacity, f_i, by the equation (*e.g.* Allen & Tildesley, 1989):

$$\Lambda_i^{-3} = \frac{\beta f_i}{e^{-\beta \mu_i}} \tag{2.6}$$

2.1.2 Metropolis Monte Carlo

Since the Markov Chain implies that a new microstate depends only on its precedent microstate it is logical to consider how to construct such a chain of microstates. Thus, the new molecular positions (that define the microstate) are generated from the present microstate by randomly:

i) Moving a molecule by a given random amount;

ii) Inserting a molecule at a random position;

iii) Deleting a randomly chosen molecule.

In addition to these three trials of generating new states, additional states, for mixtures, can be achieved by swapping the identity of a molecule. According to Cracknell, Nicholson & Quirke (1993), swapping the identity of a molecule makes the simulation faster and more efficient. However, state transitions are only possible if the ratio between density probabilities allows this change. These changes are generated using the condition of microscopic reversibility, *i.e.* the probability of a change occurring from state *o* to state *n* must be same as the probability of a change occurring from state *n* to state *o*. In our simulations, we attempt to move, insert, delete and swap identity of molecules, selecting each type of move with the same probability of ¼ (although microscopic reversibility requires only that the number of trial of insertions and deletions to be equal). The criteria for accepting each trial $\frac{\rho(n)}{\rho(o)}$ are deduced from the density probabilities defined by Equation 2.4 (or by Equation 2.5). If the trial is rejected its old configuration is restored. The probability of accepting a random move is,

$$e^{-\beta \Delta U_i} \tag{2.7}$$

that of accepting a molecule insertion is,

$$\frac{f_i \beta V}{\mathcal{N}_i + 1} \cdot e^{-\beta \Delta U_i} \tag{2.8}$$

and that of accepting a molecule deletion is,

$$\frac{\mathcal{N}_i}{f_i \beta V} \cdot e^{-\beta \Delta U_i} \tag{2.9}$$

The probability of accepting the swapping of identities between two different molecules (this corresponds essentially to deleting a molecule of species i and inserting a molecule of species j at exactly the same position) is,

$$\frac{\mathcal{N}_i f_j}{(\mathcal{N}_j + 1) f_i} \cdot e^{-\beta \Delta U_i} \tag{2.10}$$

In the above expressions, i and j represent species; and ΔU_i is the potential change when the system goes from state o to state n. The calculation of ΔU_i is addressed in the section 2.4. Each Metropolis trial is accepted with probability $0 \leq \frac{\rho(n)}{\rho(o)} \leq 1$. If $\frac{\rho(n)}{\rho(o)} \geq 1$ then the new configuration is accepted unconditionally. If the ratio is less than one then the new configuration is accepted stochastically – *i.e.*, the new configuration is accepted, or rejected, in accordance with a random number chosen from a uniform distribution in the interval [0,1]. In an insertion trial, a new molecule is created at a random position in the pore, and the identity of the species is also chosen at random. However, for a deletion trial, simply selecting a molecule at random violates the criterion of microscopic reversibility. This is because the probability of deleting a particular species would depend on the composition of the

molecules in the pore, while in the creation trial all species are created with equal probability. Therefore, when selecting a molecule for a deletion trial, it is important to first select a species at random, and then randomly choose a molecule belonging to that species.

2.1.3 Simulation of Adsorption

Equilibrium adsorption is calculated using the GCMC simulation method. In this method, the temperature, volume and the chemical potentials of all species are kept constant, while the total number of molecules fluctuates during the course of the simulation. In the GCMC method, adsorbed molecules are in equilibrium with the bulk phase (*i.e.* the chemical potential of each species inside the pore is the same as outside). The chemical potential is related to the temperature and fugacity of the bulk gas phase:

$$\mu_i = \mu_i^0 + RT \ln\left(\frac{f_i}{f_i^0}\right) \tag{2.11}$$

where the superscript, *0*, in the above equation, denotes the standard state. The fugacity is related to the species partial pressure, P_i, by the Peng & Robinson (1976) equation of state:

$$P_i = \frac{RT}{\underline{V_i} - b_i} - \frac{a_i}{\underline{V_i}\left(\underline{V_i} + b_i\right) + b_i\left(\underline{V_i} - b_i\right)} \tag{2.12}$$

where is $\underline{V_i}$ is the partial volume molar, a_i and b_i are the equation of state parameters. The calculation of the fugacity from the partial pressure is described in detail elsewhere (*e.g.* Sandler, 1999).

Before collecting any results, the first 500,000 - 1,000,000 GCMC steps ($\mathcal{N}_{equilibrium}$) are discarded to allow the system to reach equilibrium. During this equilibration, the molecules will move from their initial assigned positions to more energetically favourable positions sampled from the equilibrium ensemble. Figure 2.2 illustrates a schematic representation of the GCMC method. In each simulation, data are collected over 20 blocks of 50,000 – 100,000 GCMC steps ($\mathcal{N}_{sample}$). We use 20 blocks to provide a set of independent samples from which an average and a standard deviation are calculated.

The density of each species – the property of interest - is calculated by averaging the number of molecules in each individual pore, $<\mathcal{N}_i>$, of each species along the simulation:

$$\rho_i = \frac{\langle \mathcal{N}_i \rangle}{N_A V} \tag{2.13}$$

where N_A is the Avogadro constant and V represents the volume of the simulation cell. For the density distribution density profile across the pore, the pore is divided in small bins and the average number of molecules in each bin is counted.

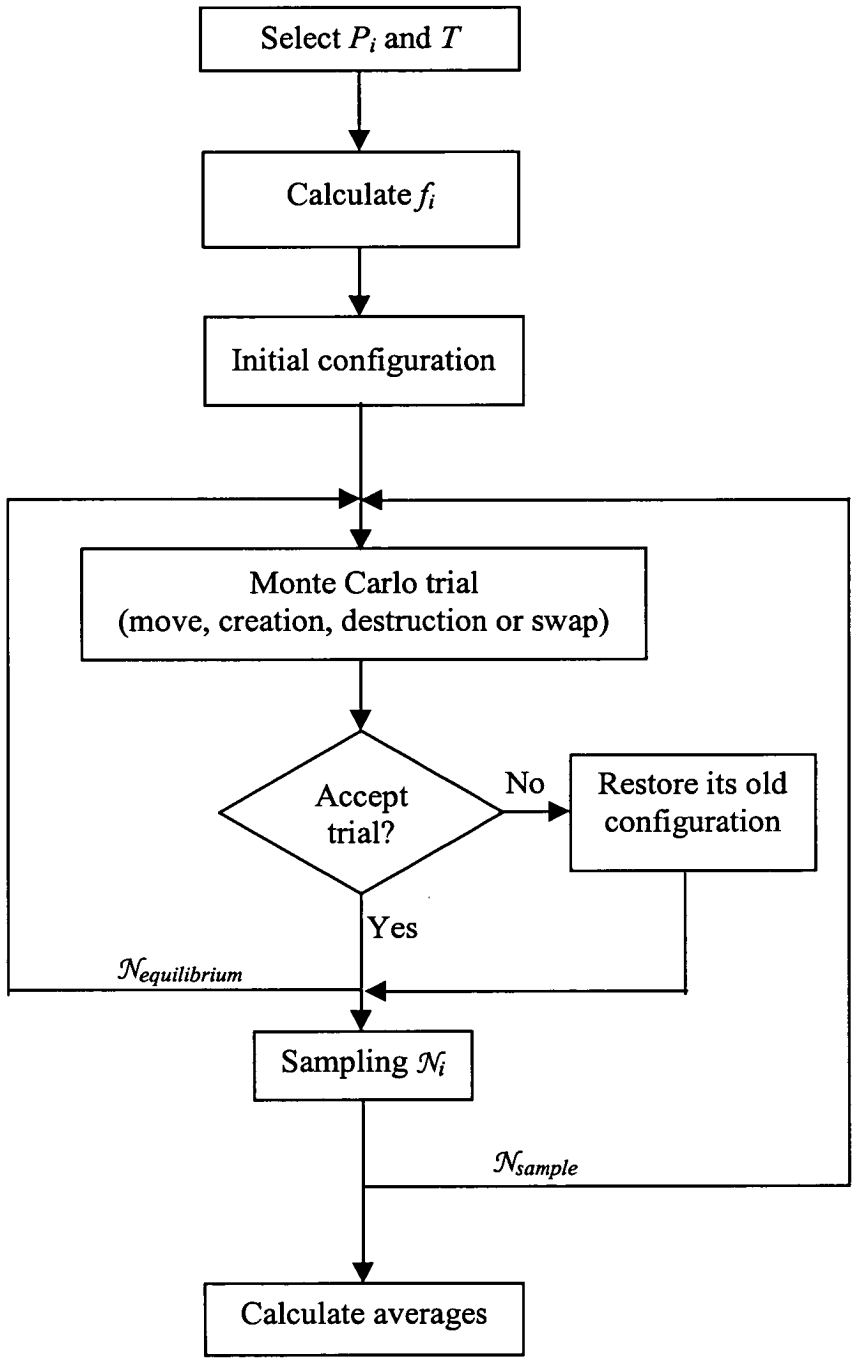

Figure 2.2 - Schematic representation of the GCMC method.

2.2 Molecular Dynamics

While the Monte Carlo method generates configurations from a particular ensemble at random, the molecular dynamics method generates configurations by solving the classical equations of motion for a $\mathcal{N}$-body system interacting through a particular intermolecular potential function, U_i. As devised by Alder & Wainwright (1959), equilibrium Molecular Dynamics (EMD) is typically applied to an isolated system containing a fixed number of molecules $\mathcal{N}$ in a fixed volume V. Because the system is isolated, the total energy E is also constant; here E is the sum of the molecular kinetic and potential energies. Thus, the variables $\mathcal{N}$, V and E determine the thermodynamic state. In MD, molecular positions, $\boldsymbol{r}$, are obtained by solving Newton's classical equation of motion:

$$\mathbf{F}_i = m_i \frac{\partial^2 \mathbf{r}_i}{\partial t^2} \tag{2.14}$$

where m_i is the mass of molecule i and

$$\mathbf{F}_i = -\frac{\partial U_i}{\partial \mathbf{r}_i} \tag{2.15}$$

is the force on that molecule. Under the influence of a continuous potential the motions of all the molecules become coupled together, giving rise to a many body problem that cannot be solved analytically. Thus, a numerical approach, the finite difference method is used to solve the equations of motion. The general idea of the finite difference approach is that time can be broken down into a series of discrete steps of length δt. Given the molecular positions and velocities at a time t we attempt to find these at a later time $t+\delta t$ with a sufficient accuracy. Thus the equations of motion are solved using a finite difference method on a step-by-step basis. Moreover, the integration of Equation 2.14 gives the atomic positions through time and integrating for a long time one gets the individual trajectories from which

the time average can be used to produce macroscopic properties. At equilibrium, this average cannot depend on the initial time or from its initial positions.

2.2.1 Integration of the Equations of Motion

The step-by-step solution of the equations of motion using a finite difference approach is performed by the use of an integration algorithm. One common algorithm is the Verlet (1967) algorithm. This is derived from a Taylor expansion of the positions about time t:

$$\mathbf{r}[t+\delta t]=\mathbf{r}[t]+\mathbf{v}[t]\cdot\delta t+\frac{1}{2}\cdot\mathbf{a}[t]\cdot(\delta t)^2 \tag{2.16}$$

$$\mathbf{r}[t-\delta t]=\mathbf{r}[t]-\mathbf{v}[t]\cdot\delta t+\frac{1}{2}\cdot\mathbf{a}[t]\cdot(\delta t)^2 \tag{2.17}$$

where a is the acceleration of the molecule and it is obtained from the relation between force and the mass of a molecule, m:

$$\mathbf{F}=m\,\mathbf{a}[t] \tag{2.18}$$

Summing Equation 2.16 and 2.17 gives

$$\mathbf{r}[t+\delta t]=2\mathbf{r}[t]-\mathbf{r}[t-\delta t]+\mathbf{a}[t]\cdot(\delta t)^2 \tag{2.19}$$

As can be seen, the Verlet algorithm is time reversible because swapping the positions at $t+\delta t$ with the positions at $t-\delta t$, in Equation 2.19, an equivalent equation is obtained. For this reason the Verlet algorithm gives good conservation of the total energy (Allen & Tildesley, 1989; Haile, 1992). The velocities are not needed to compute the trajectories, but they are useful for estimating the kinetic energy (and hence the total energy). They can be calculated from the formula:

$$v[t] = \frac{\mathbf{r}[t+\delta t] - \mathbf{r}[t-\delta t]}{2\,\delta t} \tag{2.20}$$

The Verlet algorithm is simple and compact to code and the time reversal symmetry leads to good energy conservation. However, the velocities are not well handled (see *e.g.*, Allen & Tildesley, 1989) because the addition of two numbers of different magnitudes (in Equation 2.20) can introduce numerical inaccuracies. An alternative formulation of the Verlet algorithm is the "velocity Verlet" scheme of Swope *et al.*, (1982). This algorithm has the advantage of not only storing positions, velocities, and accelerations at the same time but also minimising the numerical round-off error (Allen & Tildesley, 1989). The velocity Verlet algorithm takes the form:

$$\mathbf{r}[t+\delta t] = \mathbf{r}[t] + \mathbf{v}[t]\cdot\delta t + \frac{1}{2}\cdot\mathbf{a}[t]\cdot(\delta t)^2 \tag{2.21}$$

$$\mathbf{v}[t+\delta t] = \mathbf{v}[t] + \frac{(\mathbf{a}[t] + \mathbf{a}[t+\delta t])}{2}\cdot\delta t \tag{2.22}$$

This algorithm is implemented in two stages. First, the positions are calculated using Equation 2.21. The mid-step velocities are then calculated from the acceleration at time t by

$$\mathbf{v}\left[t+\frac{1}{2}\delta t\right] = \mathbf{v}[t] + \frac{1}{2}\mathbf{a}[t]\cdot\delta t \tag{2.23}$$

The acceleration at time $t+\delta t$ are then calculated and the velocity move is completed

$$\mathbf{v}[t+\delta t] = \mathbf{v}\left[t+\frac{1}{2}\delta t\right] + \frac{1}{2}\mathbf{a}[t+\delta t]\cdot\delta t \tag{2.24}$$

Adding Equation 2.23 and 2.24 one restores Equation 2.22. Thus, in this algorithm one must evaluate the new velocities only after one has evaluated the new positions and the new forces $\boldsymbol{F}$.

2.2.2 Molecular Dynamics at Constant Temperature

In the last section, we described the MD implementation at constant energy (NVE-MD), which cannot provide us with many useful properties, because NVE simulation results (only if properly equilibrated) can be compared with suitable experimental observations. The simplest way to maintain the temperature constant is to periodically rescale the velocity to give the desired temperature. However, we can alternatively impose a temperature on a system by bringing it into thermal contact with an external large heat bath at constant temperature. There are common two methods that describe the interaction between the simulated system and the external bath at constant temperature (Frenkel & Smit, 1996):

i) In the Andersen (1980) thermostat, the interaction with the heat bath is represented by stochastic impulsive forces that act occasionally on randomly selected molecules. These stochastic collisions can be thought of as Monte Carlo moves that transport the system from one constant energy step to another.

ii) In the Nosé-Hoover (1984a, b) thermostat, the thermal equilibrium with the surroundings is achieved by the use of an extended Lagrangian that in addition to the normal terms includes artificial coordinates and velocities.

More recently, MacElroy & Boyle (1999) have introduced the thermal diffuse scattering algorithm to perform MD at constant temperature (NVT-MD). In the thermal diffuse scattering algorithm, when a thermal collision occurs between one fluid molecule and a solid atom (from the surface wall) a change of the momentum and kinetic energy of the fluid molecule occurs. The collision occurs at the potential minimum and the molecules are reflected according to the cosine law of diffuse scattering with a Maxwellian distribution of molecular speeds. Thermal collisions are determined *a posteriori* in our simulations. When they occur, the molecule trajectory is retraced to determine the point of collision and new velocities are assigned according to the thermal diffuse scattering algorithm.

2.2.3 Simulation of Equilibrium Diffusion

Equilibrium self-diffusion, $\mathcal{D}_i$, is defined as diffusion of species in the absence of concentration (or pressure) gradients. Equilibrium diffusion can be related to the mean square displacement (MSD) of each species by Einstein's relation (see *e.g.*, Frenkel & Smit, 1996):

$$\mathcal{D}_i = \frac{1}{2d} \frac{\partial \left\langle \left(\mathbf{r}_i[t] - \mathbf{r}_i[0] \right)^2 \right\rangle}{\partial t} \tag{2.25}$$

where $\left\langle \left(\mathbf{r}[t] - \mathbf{r}[0] \right)^2 \right\rangle$ is the MSD and d is the dimensionality of the system (in a bulk phase d=3, in a slit-like pore d=2 and in a cylindrical pore d=1). Figure 2.3 shows that one can get the equilibrium diffusion coefficient from the slope of the MSD versus time.

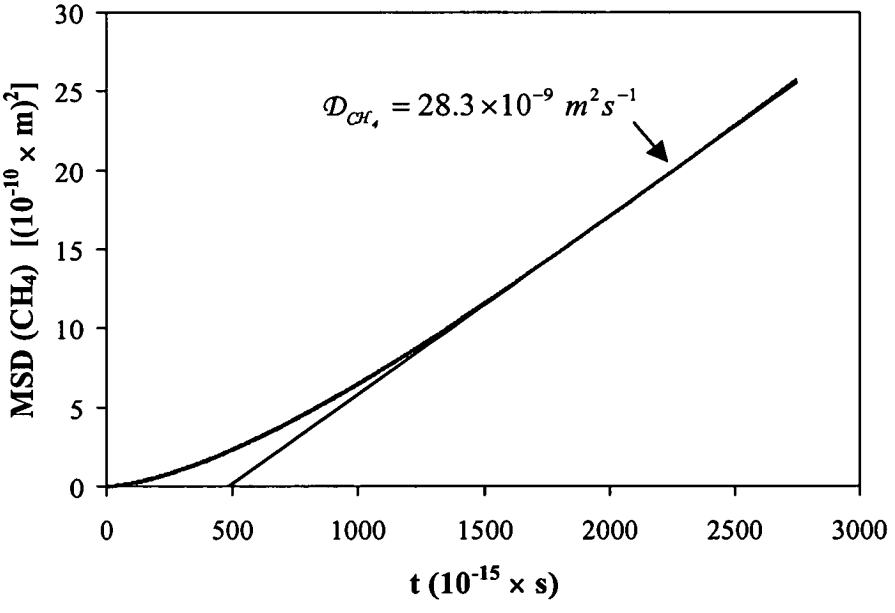

Figure 2.3 – Plot of methane MSD as function of time. (Temperature is 300 K, pressure is 3.65 bar, pore size is 20 Å)

The MSD is calculated from the EMD simulations by following the molecular trajectories:

$$\left\langle (\mathbf{r}[t]-\mathbf{r}[0])^2 \right\rangle = \frac{1}{\mathcal{N}} \sum_{j=1}^{\mathcal{N}} (\mathbf{r}_j[t]-\mathbf{r}_j[t=0])^2 \tag{2.26}$$

In each simulation, data are collected over 500,000 MD steps ($\mathcal{N}_{sample}$). Before starting sampling, the first 50,000 - 500,000 steps ($\mathcal{N}_{equilibrium}$) are discarded to allow the system to reach equilibrium. Figure 2.4 is a schematic representation of the MD method.

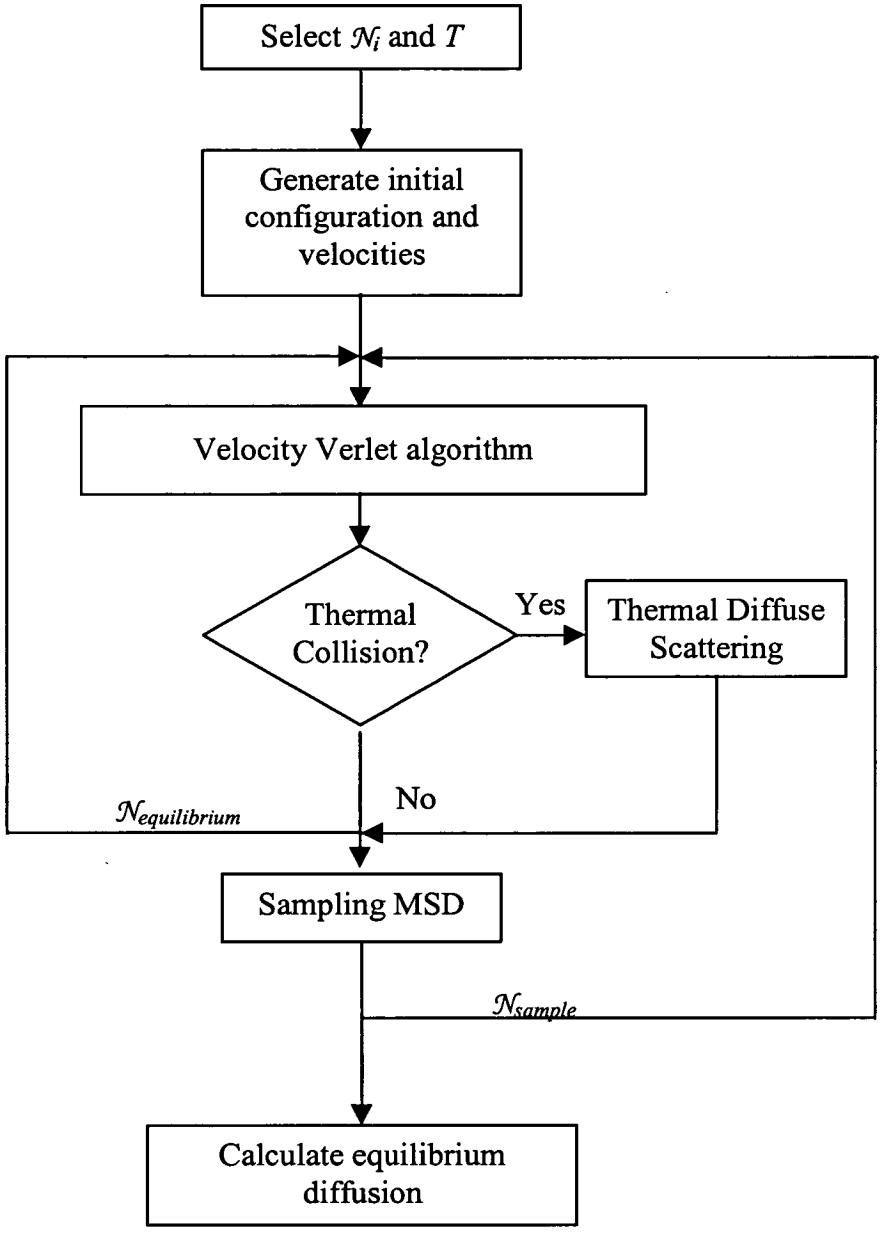

Figure 2.4 - Schematic representation of the EMD method.

2.3 Non-Equilibrium Molecular Dynamics

Transport properties are calculated using a non-equilibrium molecular dynamics technique: the Dual Control Volume Grand Canonical Molecular Dynamics (DCV-GCMD) method of Heffelfinger & van Swol (1994) and MacElroy (1994). In the DCV-GCMD method the GCMC and EMD simulations methods (described in the previous sections) are combined. DCV-GCMD allows transport properties to be studied in the presence of pressure and concentration gradients (as in an industrial process). In these simulations, two control volumes, at constant chemical potential, are placed at each side of the transport region. The chemical potential, in each control volume, is kept constant by cyclically performing a number of GCMC insertions and deletions. The weakness of the GCMC method is that it does not give us a time scale (this restricts GCMC to equilibrium adsorption) because the positions are generated stochastically - the new positions depend only on the previous positions. A rigorous molecular movement is only achieved by using MD steps because the molecular positions are obtained by solving Newton's equations of motion and, hence, the new positions are connected in time. DCV-GCMD simulations mimic the real experiment because by choosing two different pressures, or concentrations, one can define the driving force across the simulation pore. According to Heffelfinger & van Swol (1994) and MacElroy (1994), DCV-GCMD is uniquely suitable for the direct evaluation of transport diffusion.

The simulation starts by running a sequence of GCMC steps either only in those GCMC control volumes or in the entire simulation box to assign an initial position to each molecule. Then, the initial velocity is sampled according to the Maxwell-Boltzmann distribution of velocities. After this initialisation, a cycle of MD steps follows, in which molecules are free to move. A simple visual illustration of the implementation of the DCV-GCMD method is shown in Figure 2.5. Each cycle represents one sequence of GCMC and MD steps. During the GCMC part of each cycle, random insertion, deletions and identity swaps (if desired) are attempted in both GCMC control volumes, using the usual acceptance criteria, to establish

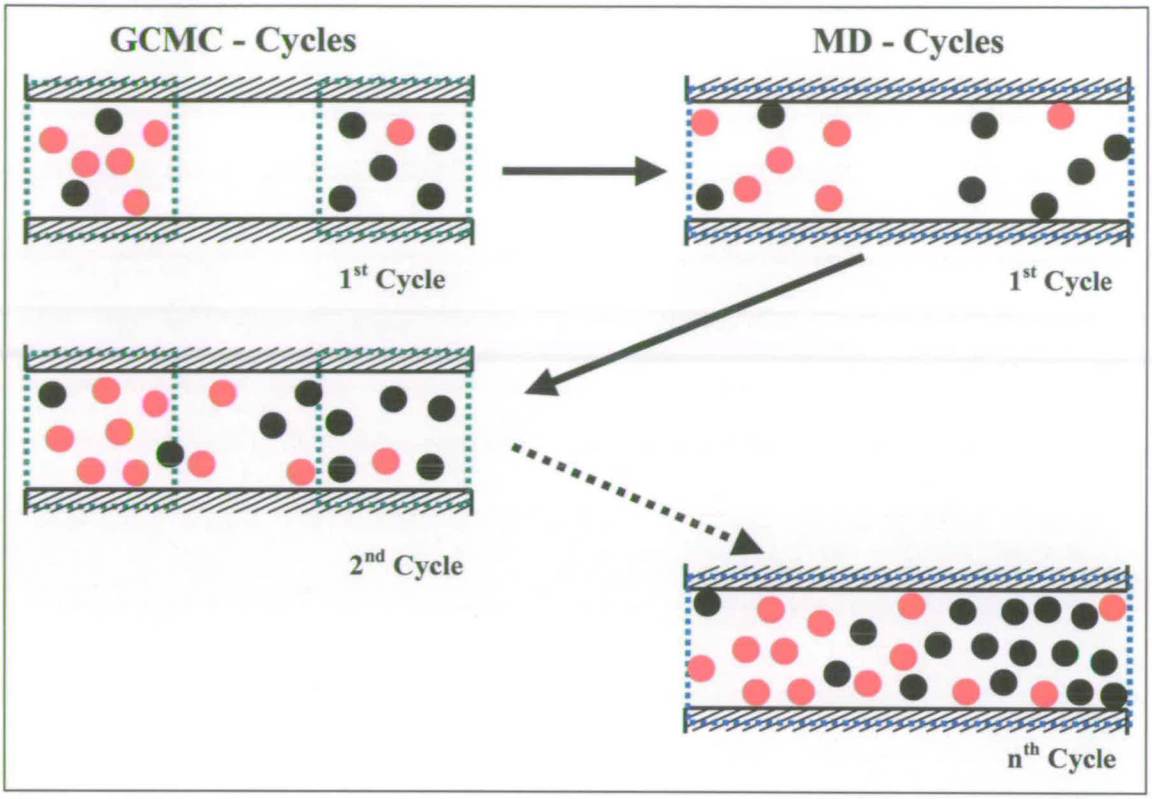

Figure 2.5 – GCMD algorithm schematic representation. Green dashed squares delimit GCMC control volumes and blue dashed rectangle delimits MD control volume. Red and black circles represent two arbitrary species of different chemical potential.

equilibrium between these two control volumes and their correspondent surrounding bulk gas (or pore intersection). Removed molecules are simply erased from the simulation while created molecules are assigned with velocities selected from the Maxwell-Boltzmann velocity distribution at the given temperature. After a GCMC cycle, the motion of the molecules in the transport region is simulated using the MD method, in which the molecular positions are obtained by solving Newton's classical equations of motion by solving the finite-difference velocity Verlet scheme (Swope *et al.*, 1982). The time step used in all our GCMD simulations is about 1.5 fs. Each simulation begins with a series of "equilibration steps" during which the steady-state concentration profile between the two GCMC control volumes is established. As for the NVT-MD, the temperature is kept constant using the thermal diffuse scattering algorithm of MacElroy & Boyle (1999). In our simulations, it was found that a cycle

of 100 GCMC trials (creations and destructions) alternated with a cycle of 5 MD steps gives best control over the chemical potential gradient (as we will see in Section 2.5).

In the original implementation of the DCV-GCMD method, only a single transport region is used. But, we have followed Furukawa, Shigeta & Nitta (1996) and used two transport regions, which we found to give better control of the chemical potential in the reservoirs and is according to our simulations up to 20 % faster for a given accuracy because we are calculating transport properties in two independent transport regions using only one high-pressure control volume. In our DCV-GCMD simulations, the simulation box consists of two control volumes, in which the chemical potentials of the species are specified, and two transport regions, in which diffusion takes place, linking the reservoirs (see Figure 2.6).

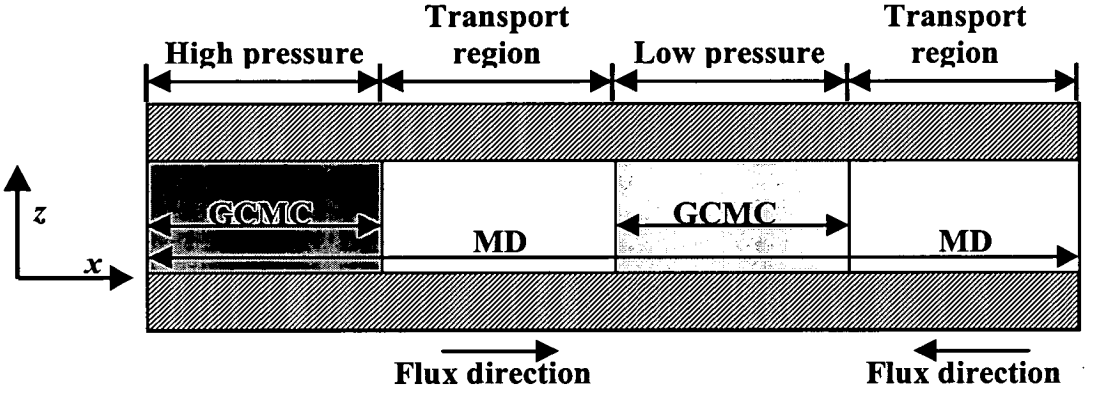

Figure 2.6 – A schematic representation of our DCV-GCMD simulation box. The GCMC control volumes are represented in grey and the transport regions in white. The flux direction is from the control volume at high pressure to the one at low pressure.

According to MacElroy & Boyle (1999), pore entrance effects may contribute significantly to the mass transfer resistance. In this work, the GCMC control volumes are placed at each end of the pore avoiding the entrance and the exit effects. We expect that pore entrance effects are only significant in pores of width comparable to the molecular diameter.

Periodic boundary conditions (see *e.g.*, Allen & Tildesley, 1989) are imposed in the x and y directions (as we will see in Section 2.4.3). This is an advantage to the original DCV-GCMD method, where only a single transport region is used, without the periodic boundary condition in the x-direction. The pore walls confine the adsorbed molecules in the z direction.

2.3.1 Simulation of Transport Diffusion

The first step in the DCV-GCMD is to define the simulation parameters and the models (for the pore and for the adsorptive molecules). Then the initial position and velocities of each molecule are assigned. Until a steady-state chemical potential gradient between both sides of the membrane is established the simulation data are discarded. In our simulations, this takes about 500,000 GCMD steps ($\mathcal{N}_{steady\text{-}state}$). Subsequently, the collection of simulation data begins.

Figure 2.7 shows a schematic representation of the DCV-GCMD algorithm used in our simulations. During each simulation both compositions and fluxes are calculated over not less than 3,000,000 MD steps (*i.e.* N_{sample} = 20 blocks of 30,000 DCV-GCMD of 5 MD steps each). For each component i we calculated its flux N_i by measuring the net number of particles crossing halfway along each transport region:

$$N_i = \frac{n_i^{L2R} - n_i^{R2L}}{\Delta t \, A_{yz}} \tag{2.27}$$

Where n_i^{L2R} and n_i^{R2L} are the number of i molecules moving from left to right and vice versa, A_{yz} is the cross section area and Δt is the sample time. The final estimate of the flux is the average of the flux in both transport regions.

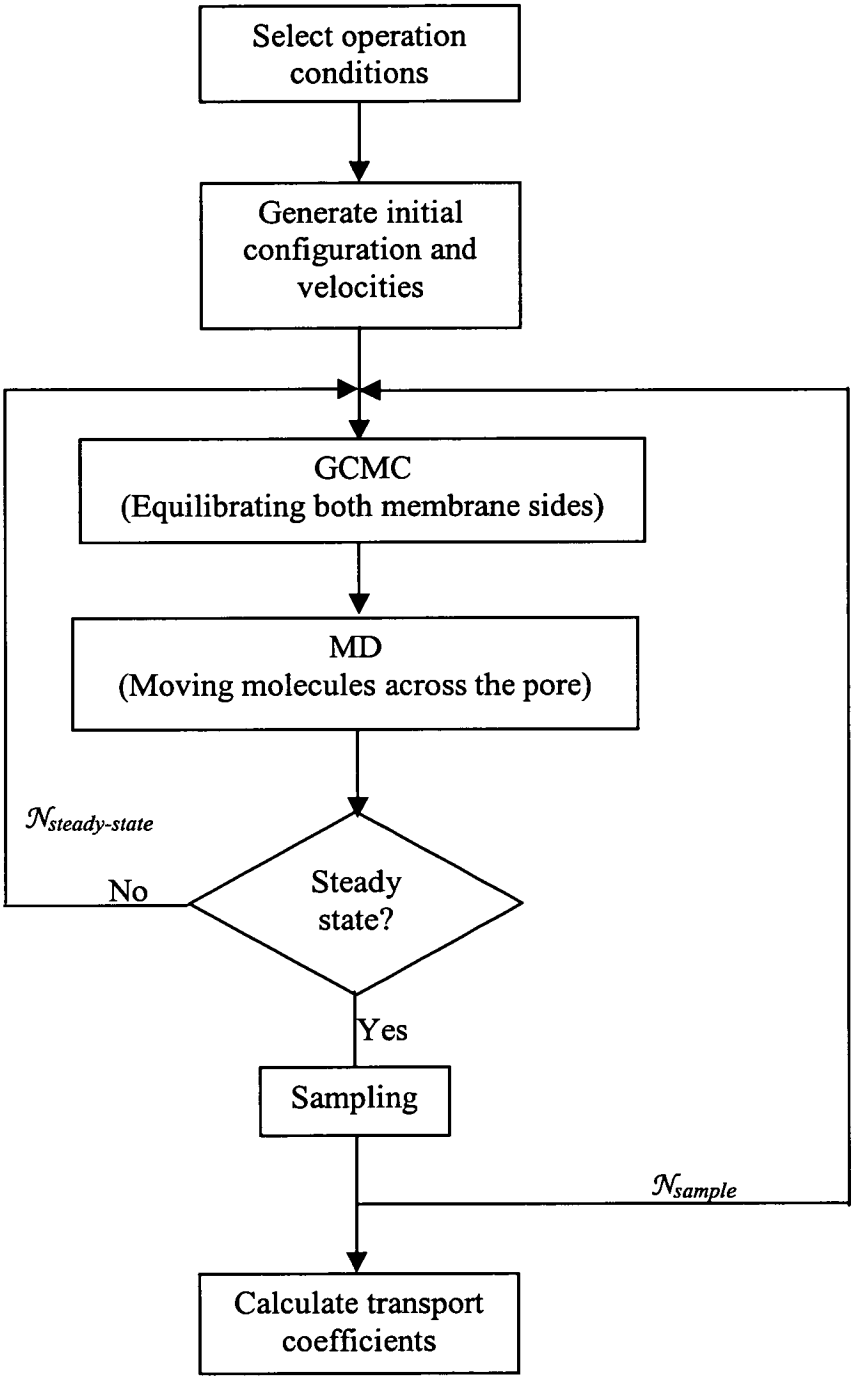

Figure 2.7 – DCV-GCMD algorithm schematic representation.

2.4 Molecular and Pore Model

2.4.1 Intermolecular Potentials

In this work, the solid phase consists of carbon atoms, and the adsorbed phase consists of hydrogen and methane molecules. These adsorptive species are both represented by single Lennard-Jones sites. The Lennard-Jones potential function is:

$$\varphi_{ij} = 4\varepsilon_{ij}\left[\left(\frac{\sigma_{ij}}{r_{ij}}\right)^{12} - \left(\frac{\sigma_{ij}}{r_{ij}}\right)^{6}\right] \tag{2.28}$$

where φ is the intermolecular energy, r_{ij} is the scalar distance between the two particles, σ and ε are the molecular size and energy parameters respectively, values of which are given in Table 2.1. The hydrogen-methane parameters are calculated using the Lorentz-Berthelot combination rules (see, *e.g.*, Allen & Tildesley, 1989). In the simulations, the potential is truncated at 19.7 Å (*i.e.* approximately half of the simulation box) to prevent discontinuities on the intermolecular force calculations.

Table 2.1 – Lennard Jones interaction parameters.

	σ (Å)	ε /K_b (K)
Carbon [1]	3.40	28.0
Methane [2]	3.817	148.3
Hydrogen [2]	2.928	37.0

[1] Steele (1974)

[2] Hirschfelder, Curtiss & Bird (1954)

This potential model is a good approximation for the almost spherical methane molecule. Methane consists of a tetrahedral carbon atom surrounded by hydrogen atoms. Since this structure is symmetric it is reasonable to model methane using a spherical geometry. On the other hand, hydrogen molecules consist in two atoms of

hydrogen on a single axis of symmetry. Thus, representing a molecule by a single sphere it is, in principle, less satisfactory for hydrogen. In this work, three simple hydrogen potential models were tested:

1) One Lennard-Jones sphere as for methane. The potential between hydrogen molecules is represented by Equation 2.28.

2) Two Lennard-Jones spheres separated by a rigid inter-atomic bond of length d=0.74 Å, $\sigma_{H\text{-}H}$=2.59Å and ε/K_b=12.5 K (*e.g.* Cracknell, 2001). The pairwise potential between to diatomic molecules is calculated as the summation of the four site-site Lennard-Jones contribution (see Figure 2.8):

$$\varphi_{ij} = 4\sum_{k=1}^{2}\sum_{l=1}^{2}\varepsilon_{ij}\left[\left(\frac{\sigma_{ij}}{r_{ij}^{kl}}\right)^{12} - \left(\frac{\sigma_{ij}}{r_{ij}^{kl}}\right)^{6}\right] \tag{2.29}$$

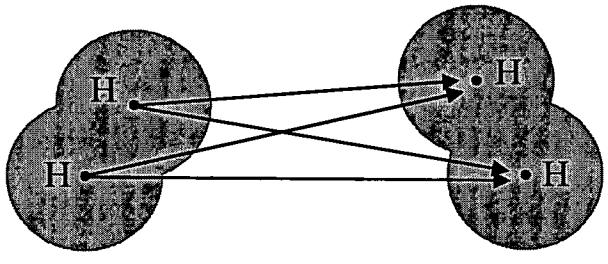

Figure 2.8 – Potential model illustration showing the four site-site contributions to the total potential between two hydrogen molecules.

3) One Lennard-Jones sphere ($\sigma_{H\text{-}H}$=2.958Å, ε/K_b=36.7 K) located at the centre of mass of the molecule and a quadrupolar interaction (Darkrim & Levesque, 1998). The hydrogen quadrupole is described by three charges: two charges q (q=0.615 10^{-26} esu) located on the protons, distant from 0.741 Å, and one charge of -2q located at the centre of mass (see Figure 2.9).

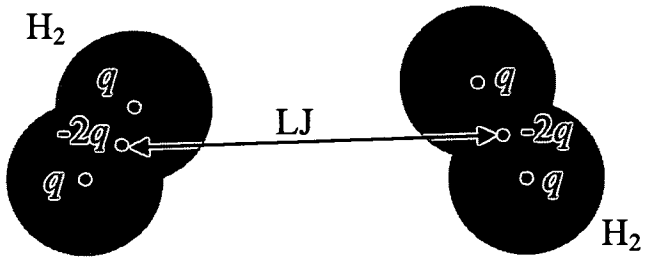

Figure 2.9 – Potential model illustration showing the quadrupole contribution to the total potential between two hydrogen molecules. Lennard-Jones interaction is only between the centre of mass of the molecules.

The total potential between two molecules is given by the summation of the Lennard-Jones interaction and the quadrupole-quadrupole interactions:

$$\varphi_{ij} = 4\varepsilon_{ij}\left[\left(\frac{\sigma_{ij}}{r_{ij}}\right)^{12} - \left(\frac{\sigma_{ij}}{r_{ij}}\right)^{6}\right] + \frac{1}{4\pi\varepsilon_0}\sum_{k=1}^{3}\sum_{l=1}^{3}\frac{q_i^k\, q_j^l}{r_{ij}^{kl}} \qquad (2.30)$$

where q_i^k and q_j^l are charges (subscripts i and j refer to molecules while superscripts k and l refer to charges) and r_{ij}^{kl} is the separation distance between the two charges. ε_0=8.8542×10^{-12} C^2 N^{-1} m^{-2} is the permittivity of free space. The use of Equation 2.30 raises the problem of handling long-range forces. Lennard-Jones potentials can be truncated within few molecular diameters of distance without losing precision. To evaluate the importance of the long range quadrupole-quadrupole interactions a simulation box of about 1000 Å was used (*i.e.*, about 25 times larger than the normal simulated box size used in this thesis). To efficiently calculate the long-range interaction one should use the Ewald sum (see, *e.g.*, Allen & Tildesley, 1989).

Figure 2.10 shows the difference in density between the three potential models studied. The two-centre model for hydrogen was found to produce only a small difference in the equilibrium adsorption results compared with the single-centre model. In addition, quadrupole-quadrupole interactions between the hydrogen

molecules were also found to contribute only a few percent to the total adsorption. These conclusions are supported by other studies (Cracknell, 2001; Darkrim & Levesque, 1998). Thus, in this work we represent hydrogen molecules by a single Lennard-Jones sphere. Although significant deviation in the adsorbed density was not observed for the three methods considered, the molecular shape effect on diffusion might be significant at high pressures (see Figure 2.10). However, as we will show later, significant hydrogen fluxes arise only when there is a low-density region near the centre of the pore, where the diatomic nature of the hydrogen molecule would be expected to have a very small effect.

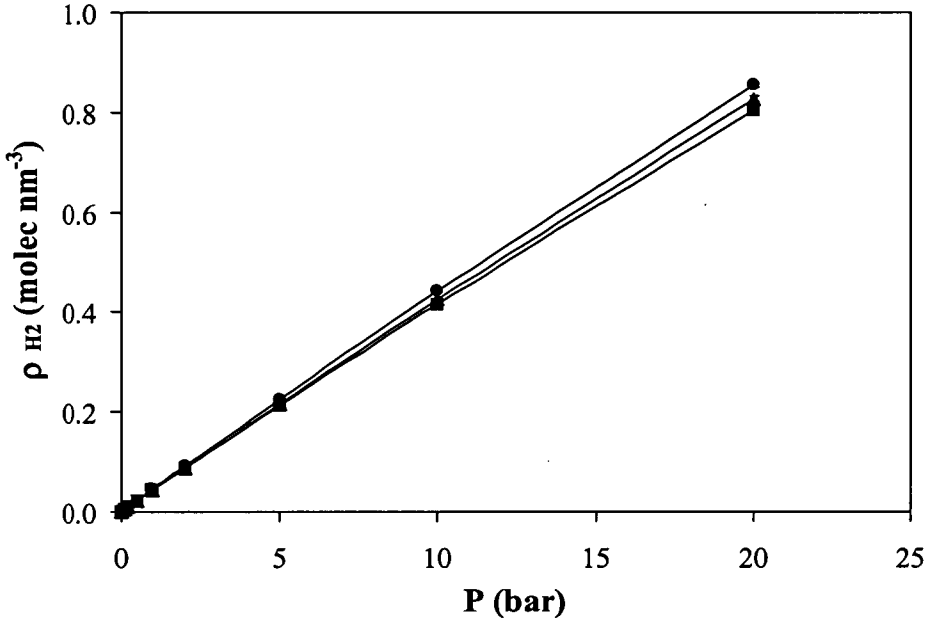

Figure 2.10 - Comparison between hydrogen isotherms, at 300 K and pore size of 10 Å, using different molecular potential models: one Lennard-Jones site (circles), two Lennard-Jones sites (triangles) and one Lennard-Jones site located at the centre of the molecules plus a quadrupolar interaction (squares).

2.4.2 Pore Model

The pore is represented by a slit, bounded by blocks of graphite and is composed of Lennard-Jones carbon atoms. Despite its simple geometry, this pore model has been used successfully to characterise carbon adsorbents and to predict adsorption in these materials (see, *e.g.*, Davies & Seaton, 1999). Furthermore, measurements of the heat of adsorption of various gases seem to agree with a slit-shaped rather than cylindrical pore model (Rao, 1991).

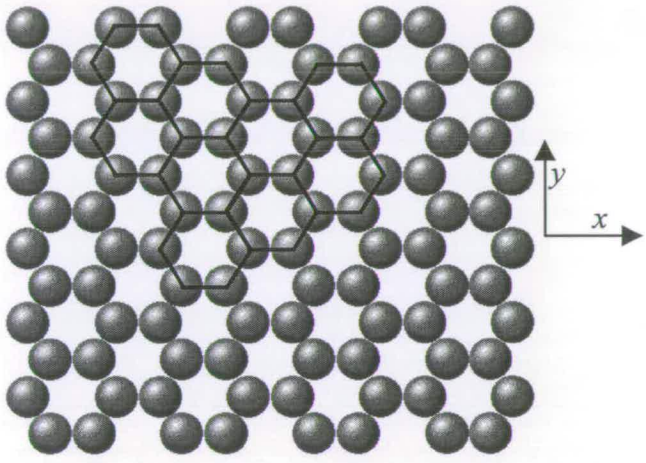

Figure 2.11 – Detail of the pore surface showing the graphitic surface structure (lines show the hexagonal structure). Carbon atoms are reduced in size to make structure clear.

The interaction between a fluid molecule and the carbon is calculated as follows: the surface layer is atomic with the carbon atoms held fixed in space in a graphite-like structure (see Figure 2.11) and the 12-6 Lennard-Jones potential function is used; subsequent layers are considered to be smooth and their interaction is represented by Steele's 10-4-3 potential (Steele, 1974):

$$\varphi_{sf}(z) = 2\pi\rho_s\varepsilon_{sf}\sigma_{sf}^2\Delta\left[\frac{2}{5}\left(\frac{\sigma_{sf}}{z}\right)^{10} - \left(\frac{\sigma_{sf}}{z}\right)^{4} - \frac{\sigma_{sf}^4}{3\Delta\left(0.61\Delta + z\right)^3}\right] \qquad (2.31)$$

Here, Δ is the distance between the two graphite layers (Δ=3.35 Å), ρ_s is the carbon number density in the graphite (ρ_s = 0.114 Å^{-3}) and z is the perpendicular distance between the fluid particle and the first smooth layer. σ_{sf} and ε_{sf} are the solid-fluid Lennard-Jones parameters calculated using the Lorentz-Berthelot combination rules.

The connection between the two GCMC reservoirs in the DCV-GCMD simulation cell and experimental systems may be made in two ways: the reservoirs represent either the bulk gas on each side of the membrane or, more realistically, the fluids present at two neighbouring pore intersections. With the latter interpretation, the individual pore is taken as representative of all the pores in the membrane, assuming them to be identical. The pore width studied varies between 5 Å and 20 Å. The size of the simulation box is approximately 160 Å by 40 Å, rounded to the closest integer number of surface graphite rings (*i.e.* 38 × 16 graphite rings orientated in the x direction).

2.4.3 Periodic Boundaries Conditions and Minimum Image Convention

A common characteristic of molecular simulations is the use of periodic boundary conditions. The molecules are contained within a basic simulation box. When a molecule leaves one side of the simulation box, its image enters from the opposite side as shown in Figure 2.12 (*e.g.* Allen & Tildesley, 1989).

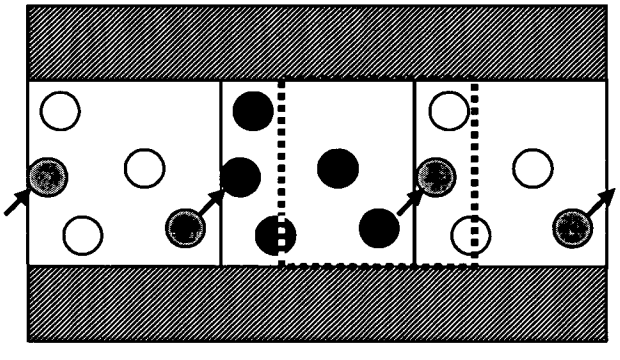

Figure 2.12 - Periodic boundary conditions in a cross section of our pore (in a two dimensional illustration). The dashed square represents the minimum image convention relatively to the moving molecule.

In the minimum image convention, each molecule sees one image of every other molecule in the system (which is repeated infinitely via the periodic boundary method). The potential and force are calculated with the closest molecule or image, as illustrated in Figure 2.12 by a dashed square. When periodic boundary conditions are being used the cutoff should not be more than half the length of the cell to avoid counting the same molecule twice.

2.5 Program Code Validation

In Figure 2.13 we compare the pure-component bulk density obtained by our GCMC program and using the Peng-Robinson equation of state (via Equation 2.12) with the experimental densities reported by Lide & Kehiaian (1994). There, we can see an excellent agreement between our GCMC simulated densities and the experimental densities. The maximum deviation between the experimental densities and the simulated densities calculated is smaller than about 0.5 %.

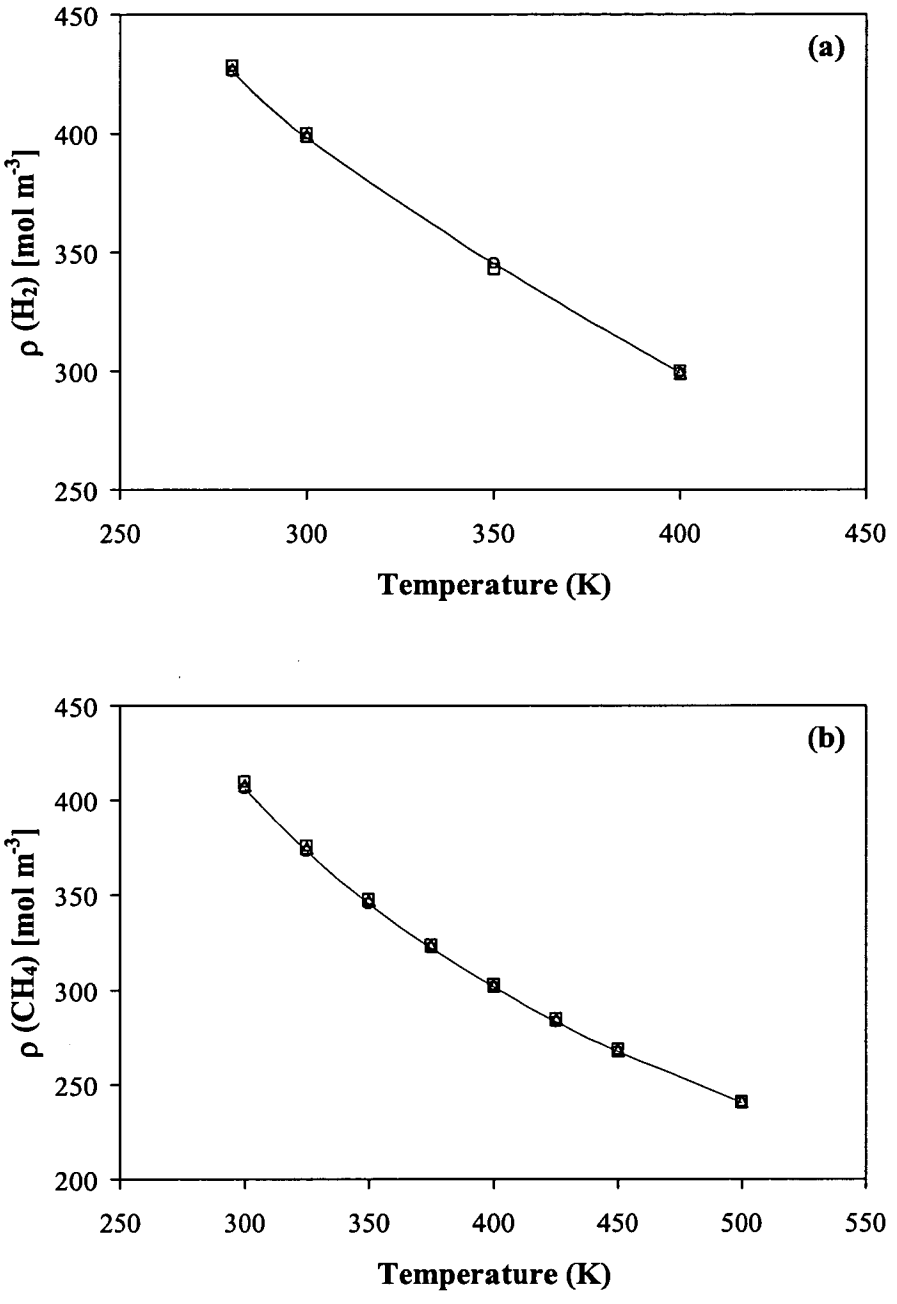

Figure 2.13 – Comparison of pure bulk densities at 300 K for (a) hydrogen and (b) methane. Experimental densities (triangles), Peng-Robinson equation of state (squares) and GCMC simulations (circles). The bulk pressure is 10 bar and simulation box is a cube of 100 Å of width.

In Figure 2.14 we compare a pure-methane adsorption isotherm at 296 K, obtained by our program, with the results obtained by Nicholson & Cracknell (1996) and Davis (1999) in a 9.53 Å pore. The adsorption shown is expressed in number of molecules absorbed per cubic nanometre of pore volume. An excellent agreement can be seen between the results obtained by our GCMC program and the results reported by those authors. Our adsorption results of a 80 % hydrogen / 20 % mixture methane at 300 K are compared in Figure 2.15 with the results of Davis (1999) for a slit size of 10 Å. Again, our results are in good agreement with other authors results. Although this agreement does not prove that the GCMC program is 100 % error free it is very strong evidence to support the correctness of the program.

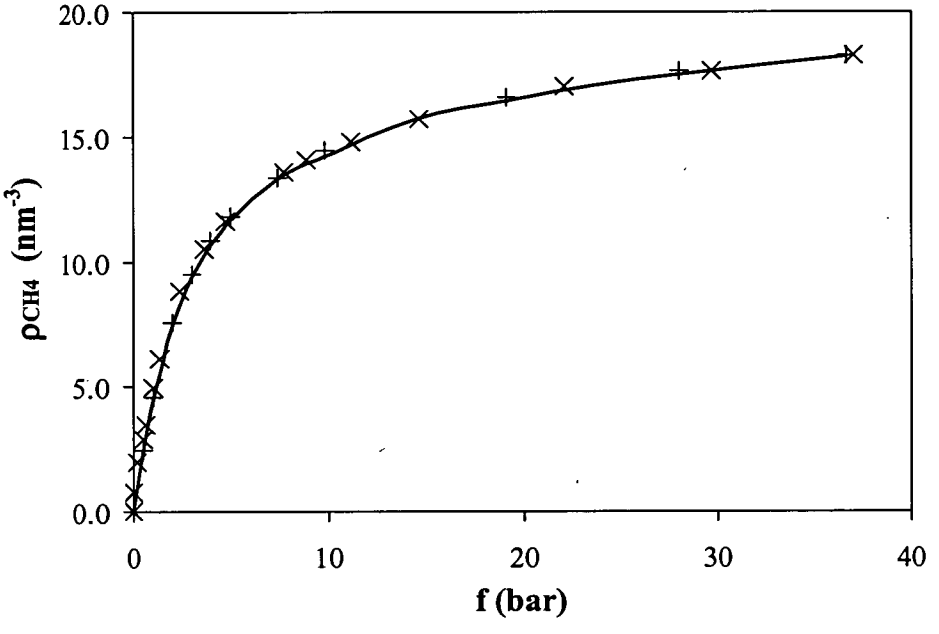

Figure 2.14 – Comparison of pure methane isotherm at 296 K (pore size is 9.53 Å): Nicholson & Cracknell (×), Davis (+) and this work (–).

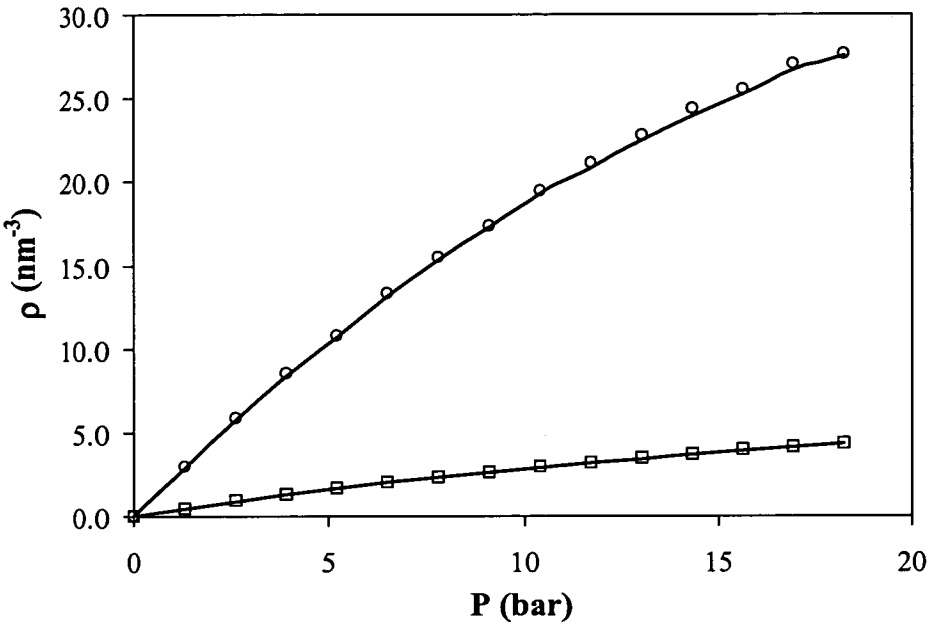

Figure 2.15 – Comparison of binary hydrogen (80 %) - methane (20 %) isotherm at 300 K (pore size is 10 Å): Davis (1999) (symbols) and this work (lines). Circles represent methane and squares represent hydrogen.

Due to the absence of published diffusion coefficients using the thermal diffuse scattering of MacElroy & Boyle (1999) in slit-like pores, we cannot test directly our EMD and NEMD results. However, simple tests were performed to ensure that there is not any error. The first check is verifying if the MD program, running at constant energy (NVE-MD), is conserving the total energy. Figure 2.16 shows the variation of energies (total, kinetic and total) along the course of a short run. The total energy oscillation is about 16 ppb (16 parts in 10^6). According to Allen & Tildesley (1989), energy fluctuations of order 100 ppb are generally acceptable for Lennard-Jones systems.

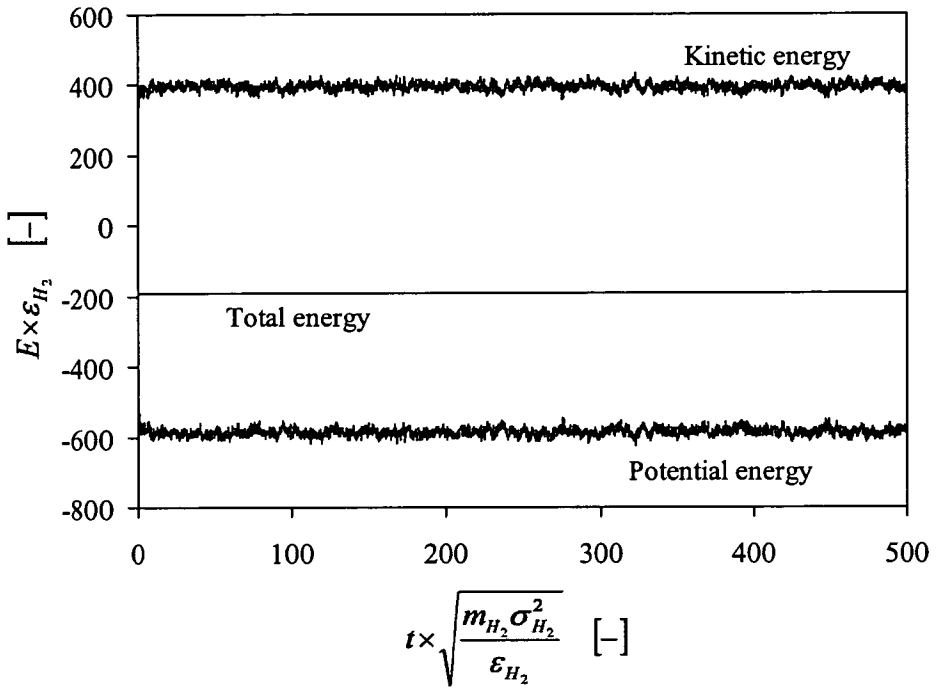

Figure 2.16 – Total, potential and kinetic energy as function of the simulation time in a NVE-MD simulation. (T=300 K, w=11.43 Å, $\mathcal{N}_{H2}$=50, $\mathcal{N}_{CH4}$=50 and δt=1.5 fs.)

The second test is to determine if the thermal diffuse scattering of MacElroy & Boyle (1999) is working properly (*i.e.* if the algorithm is keeping the temperature constant through out the simulation). Figure 2.17 shows the NVE-MD and NVT-MD programs temperature response to an initial temperature of 300 K (starting from the same configuration). Conditions used are that total number of molecules is 100 ($\mathcal{N}_{H2}$=50, $\mathcal{N}_{CH4}$=50) and the pore size of 11.43 Å. It can be seen from Figure 2.17 that the thermal diffuse scattering provides a good control of the temperature: the final average of temperature is 300.4 ± 0.9 K.

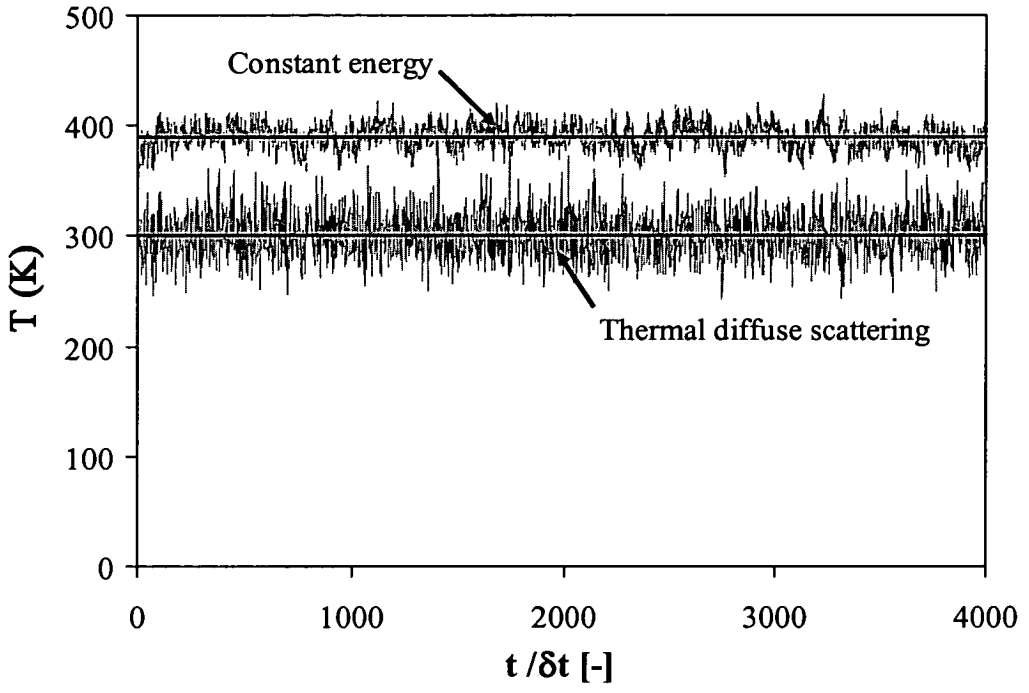

Figure 2.17 – Temperature comparison between the NVE-MD and NVT-MD algorithms for an initial temperature of 300 K at each time step. Horizontal lines represent the average temperature. (w=11.43 Å, $\mathcal{N}_{H2}$=50, $\mathcal{N}_{CH4}$=50 and δt=1.5 fs.)

Figure 2.18 shows the pure-methane density profiles across a slit pore 20 Å in width, obtained by GCMC, NVE-MD and NVT-MD at 538.7 K and 17.59 bar. There, it is shown that the density profiles are in excellent agreement which demonstrates the ability of the thermal diffuse scattering algorithm to reproduce the isothermal density profile. It is worth emphasising that these density profiles are obtained by independent simulation techniques and are a strong evidence of the correctness of the programs. In addition, Figure 2.18 shows the existence of adsorbed methane layers near the walls (shaded areas). The average thickness of each layer is about 3 Å. The middle-pore density remains roughly constant across the pore because the molecules in this region are far from the influence of the surface potential.

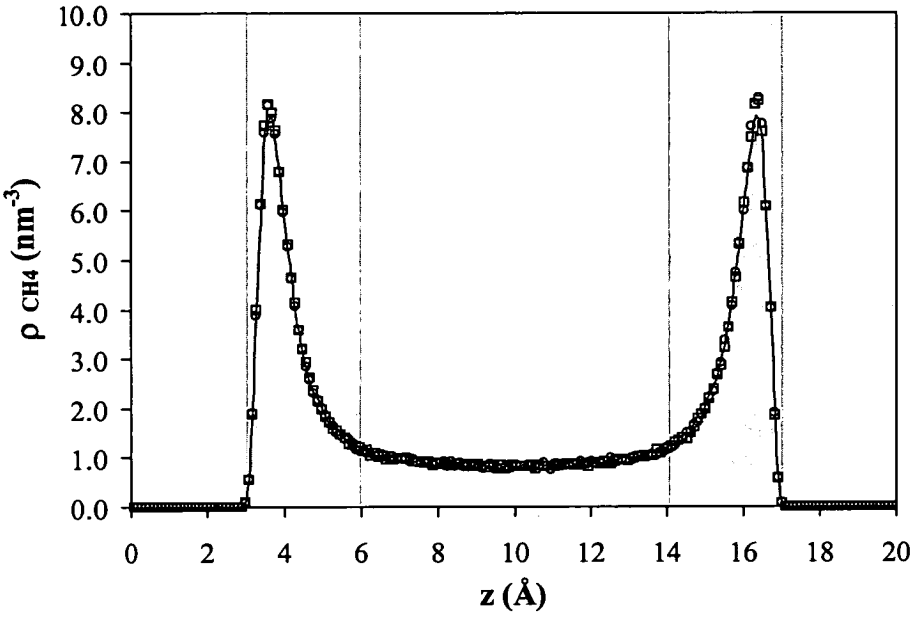

Figure 2.18 – Pure-methane density profile across a slit pore 20 Å at 538.7 K obtained by different simulation methods: GCMC (line), NVE-MD (circles) and NVT-MD (squares). Shaded areas represent adsorbed layers on the surface.

From Figure 2.19 it can be seen the pure-methane density calculated in the high pressure reservoir of the GCMD conforms with the density calculated from the GCMC program. In addition, the GCMC density profile is perfectly horizontal denoting a good chemical potential control. It is important to have a rigorous control on the chemical potential in each GCMC region to have the correct driving force (*i.e.* gradient of density along the pore). It was found that a ratio of 100 GCMC trials for each 5 MD steps gives the best control of the chemical potential in our system. In Section 2.3 we have explained that the GCMD simulation alternates a cycle of GCMC trials (creations and destructions) with a cycle of MD steps. Figure 2.19 and Figure 2.20 show the importance of using a correct ratio between the cycle of GCMC trials and the cycle of MD steps. If we use a large number of MD steps, the molecules will move out the GCMC region creating a density depression (shaded area in left hand side of Figure 2.20) giving the wrong density profile in the transport region (although the average density is in conformity with the GCMC results).

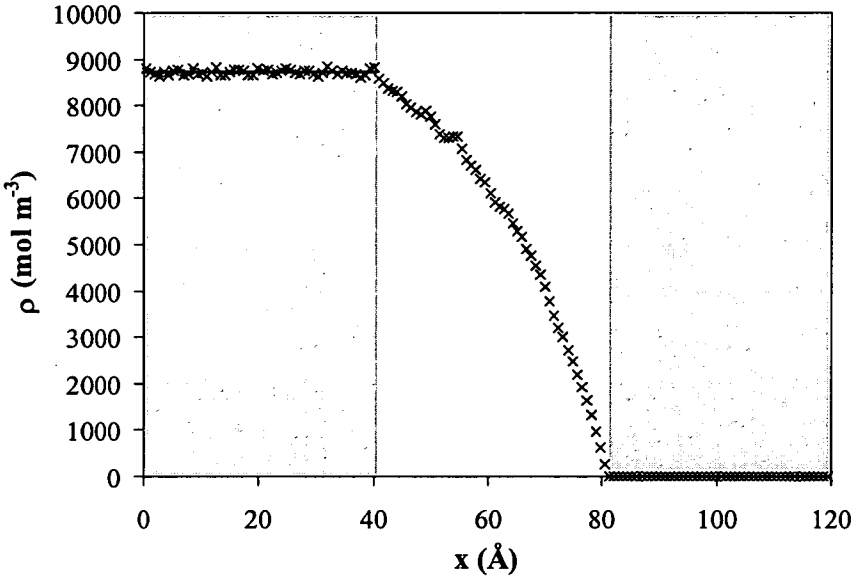

Figure 2.19 – Methane density profile along the pore length at 300 K in a pore of 8 Å. Shaded areas represent GCMC regions; each region is about 40 Å. Horizontal line represents density obtained from the GCMC simulations. The ratio between GCMC and MD steps in each GCMD cycle is 100 to 5.

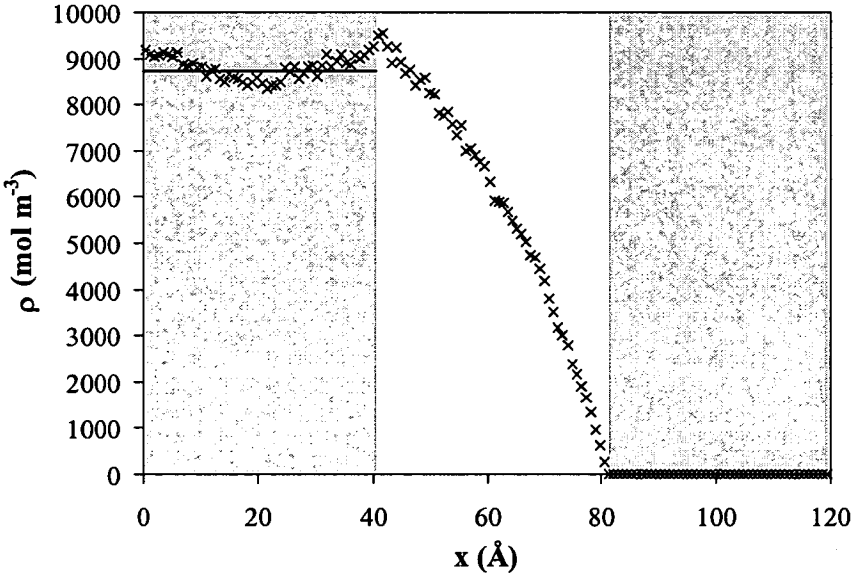

Figure 2.20 – Methane density profile along the pore length at 300 K in a pore of 8 Å. Shaded areas represent GCMC regions; each region is about 40 Å. Horizontal line represents density obtained from the GCMC simulations. The ratio between GCMC and MD steps in each GCMD cycle is 100 to 20.

Arya, Chang & Maginn (2001) recently demonstrated the importance of adding a streaming velocity, calculated from the averaged previous flux, to the newly created molecules. They showed that simulations in which a streaming velocity (i.e. a bias to the velocity in the direction of flow) is not added are less efficient and, in some circumstances, liable to bias, giving a discontinuity in the longitudinal density profile at the ends of the transport region. In our simulations, the thermal scattering algorithm cancels the streaming velocity effect in pores smaller than about 8 Å. [When a thermal collision occurs between a fluid molecule and a carbon atom on the surface the new molecular velocity is sampled from the Maxwell-Boltzmann distribution (MacElroy & Boyle, 1999), and the "streaming velocity information" is lost.] However, as the pore gets wider than about 10 Å there is a small discontinuity giving errors of a few percent in the flux.

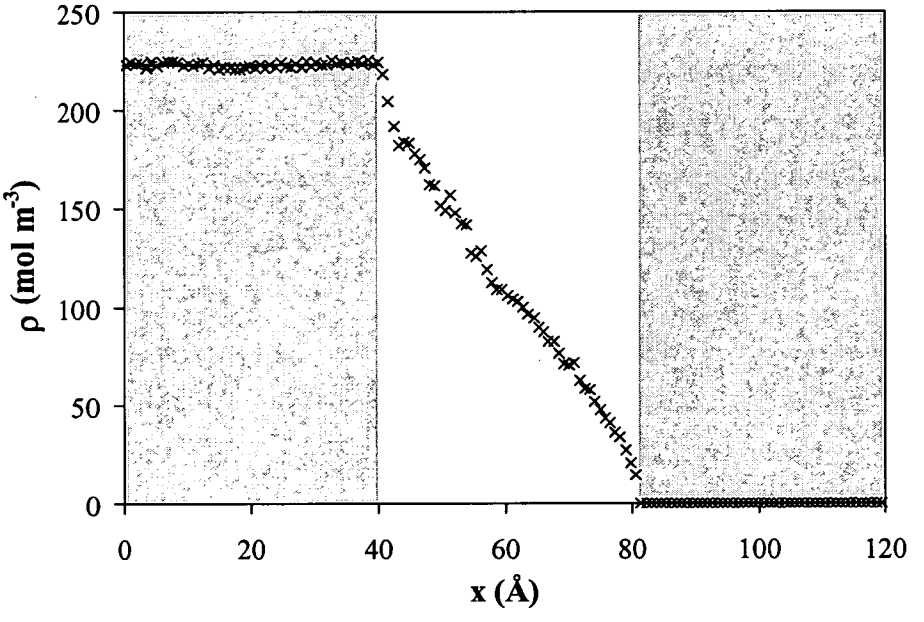

Figure 2.21 – Methane density profile along the pore length at 500 K in a pore of 20 Å. Shaded areas represent GCMC regions; each region is about 40 Å. Horizontal line represents density obtained from the GCMC simulations. Ratio number between GCMC and MD steps in each GCMD cycle is 100 to 5.

Figure 2.21 shows an example of discontinuity (at 40 Å and at 81 Å) obtained in our simulations at 500 K in a pore of 20 Å. These density discontinuities are mainly observed at high temperature and for large pores. We do not expect that our transport results are affected by these discontinuities because we use only the density profile in the transport region to calculate the transport properties. Nevertheless, an attempt to add a streaming velocity to the newly created molecules was made. But, the addition of the proper streaming velocity is nontrivial, since the streaming velocity is the purpose of the simulation and so is not known *a priori* as described by Arya, Chang & Maginn (2001). If the streaming velocity added is large we introduce a bias in the overall velocity and therefore on the density profile. On the other hand, if the streaming velocity is too small it does not produce any effect on the density profile.

2.6 Summary

In this chapter, simulation methods to calculate equilibrium adsorption, equilibrium diffusion and transport diffusion were presented. Equilibrium adsorption is calculated using the Grand Canonical Monte Carlo (GCMC) method. Equilibrium diffusion (*i.e.* diffusion in absence of gradients of chemical potential) is calculated using the Equilibrium Molecular Dynamics (EMD) method. However, the Grand Canonical Molecular Dynamics (GCMD) method is uniquely suited for systems with gradients of chemical potential as it can describe transport properties (flow and diffusion).

In our system, the solid phase consists of carbon atoms, and the adsorbed phase consists of hydrogen and methane molecules. These adsorptive species are both represented by single Lennard-Jones sites. This model is a good approximation for the almost spherical methane molecule. However, representing hydrogen by a single sphere it is, in principle, less satisfactory for hydrogen. But, we have shown that representing hydrogen by a two-centre model produces only a small difference in the

equilibrium adsorption results. In addition, quadrupole-quadrupole interactions between the hydrogen molecules were also found to contribute only a few percent to the total adsorption. The interaction between a fluid molecule and the carbon is calculated as follows: the surface layer is atomic with the carbon atoms held fixed in space in a graphite-like structure and the 12-6 Lennard-Jones potential function is used; subsequent layers are considered to be smooth and their interaction is represented by Steele's 10-4-3 potential.

Some density profile discontinuities are observed in our simulations mainly at high temperature and for large pores. However, we do not expect that our transport results are affected by these discontinuities because we use only the density profile in the transport region to calculate the transport properties.

3. Simulation of Adsorption and Diffusion in Microporous Carbons

In this chapter, competitive adsorption and diffusion in microporous carbons are investigated. Equilibrium adsorption is studied using Grand Canonical Monte Carlo while transport diffusivities are studied using Grand Canonical Molecular Dynamics. Simulated equilibrium adsorption and transport diffusion results for different pore sizes and temperatures are presented. In this work, the relationship between the amount adsorbed and the pressure at constant temperature is expressed by the Langmuir isotherm. To calculate the diffusion coefficients we use the Generalised Maxwell-Stefan diffusion coefficients developed by Wesselingh & Krishna (1992). We found that the contribution of viscous flow and cross-diffusion coefficients makes an insignificant contribution to the total flux. In addition, Maxwell-Stefan diffusion coefficients are found to be composition independent as suggested by Wesselingh & Krishna (1992). To investigate the contribution of different diffusion mechanisms to the total diffusion the pore was divided into two regions according to their local densities: the wall region; and the middle pore region. The total diffusion coefficient was found to depend on the number fraction of molecules in each transport region. The simulated operating conditions in this chapter (*i.e.* temperature, pressure and composition) chosen are typical off-gas stream conditions in refineries.

3.1 Equilibrium Adsorption

3.1.1 Simulated Equilibrium Isotherms

Adsorption is the process by which liquid or gaseous molecules are concentrated on a solid surface, which in our case is a carbon. When a gas comes into contact with a solid surface, molecules of the gas will adsorb to the surface in quantities that are a function of their partial pressure in the bulk phase. The relationship between the

amount adsorbed and the pressure, or concentration, at constant temperature is known as the adsorption isotherm. In equilibrium adsorption the rate of adsorption of molecules onto the surface is exactly counterbalanced by the rate of desorption of adsorbed molecules back into the gas phase.

The effect of the pore size on pure-component isotherms for hydrogen and methane is shown in Figure 3.1. It can be seen in Figure 3.1a that the adsorption of hydrogen shows a linear dependence on pressure for all pore sizes studied (*i.e.* hydrogen is in the Henry's law region). In the Henry law region the adsorbed density, ρ_1, is linearly dependent of the bulk phase partial pressure, P_i:

$$\rho_i = H_i P_i \tag{3.1}$$

where H_i is the Henry's constant. On the other hand, methane (Figure 3.1b) shows evidence of some pore saturation especially in pores smaller than about 9 Å because the isotherm starts to bend. [The pore saturation corresponds to complete occupancy of the pore volume by the adsorbing molecules. Once the pore saturation has been reached, the adsorbed density does not change with the increase of pressure (*i.e.* the isotherm becomes more horizontal).] Methane isotherms are fitted to the Langmuir isotherm. Langmuir isotherm is given by (see *e.g.*, Rouquerol, Rouquerol & Sing, 1999):

$$\rho_{CH_4} = \frac{m_{CH_4} b_{CH_4} P_{CH_4}}{1 + b_{CH_4} P_{CH_4}} \tag{3.2}$$

where b_{CH_4} is the adsorption constant, P_{CH_4} is the methane partial pressure and m_{CH_4} is the adsorbed density for which the surface is completely covered. For pores wider than 11 Å, the methane isotherms become linear (for the pressure range studied).

The differences between the behaviour of hydrogen and methane (shown in Figure 3.1) can be explained based on the difference strengths of adsorption. As will be discussed later in this section, methane molecules adsorb onto carbon more strongly

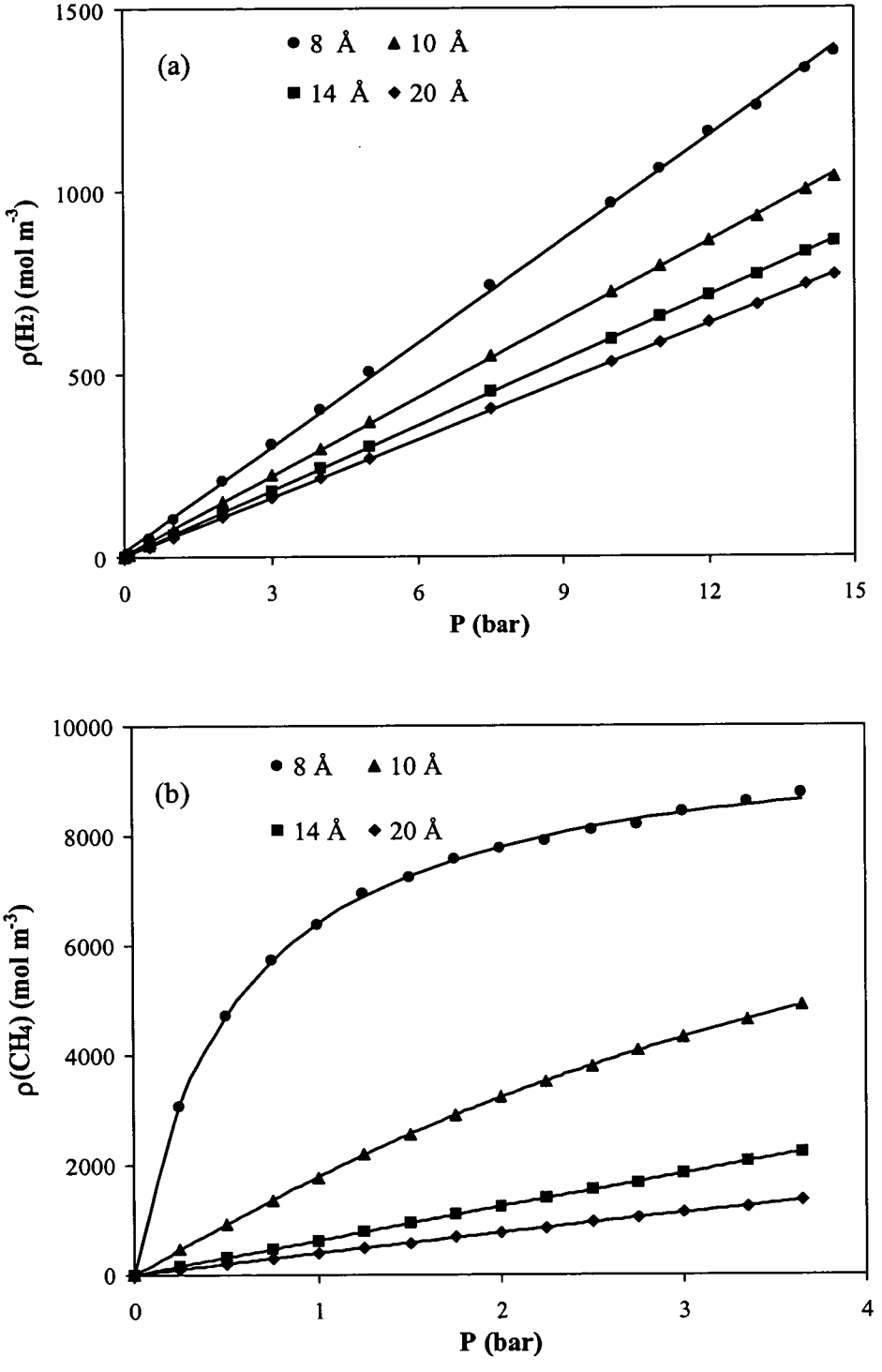

Figure 3.1 – Pure-component isotherms for different pore sizes at 300 K: a) hydrogen and b) methane.

than hydrogen because of their higher molecular weight. Thus, methane densities are always higher that the hydrogen densities.

Isotherms for a mixture of methane and hydrogen at 300 K at different pore sizes in shown in Figure 3.2. For a binary mixture, the adsorbed density of species *i* is fitted to the extended Langmuir isotherm equation by (see *e.g.*, Rouquerol, Rouquerol & Sing, 1999):

$$\rho_i = \frac{m_0 \, b_i \, P_i}{1 + b_{H_2} \, P_{H_2} + b_{CH_4} \, P_{CH_4}} \tag{3.3}$$

To have thermodynamic consistency (*i.e.* the sum of all surfaces coverage and fraction of vacant sites must be equal to unity) the monolayer capacity, m_0, of both species must be the same (Sircar, 1991). According to Kapteijn, Moulijn, & Krishna (2000), this is particularly important for diffusion, as we will discuss in Section 3.2.

Figure 3.2a shows that hydrogen isotherms are particularly affected by the presence of methane (the most strongly adsorbing species). The pure-component hydrogen isotherm which is linear at 8 Å becomes more curved and the maximum hydrogen capacity decreases (because hydrogen adsorption is restricted to the void space between methane molecules). A better perception of the competitive adsorption effect of methane over hydrogen can be seen by the following simulation snapshots (shown in Figure 3.3). As can be observed, the smaller pore is filled exclusively with methane molecules – the hydrogen molecules are excluded from the pore. However, as the pore size gets wider (*e.g.*, 20 Å), the hydrogen occupies mainly the mid-pore channel while methane molecules are preferentially located on the pore surface. On the other hand, the methane isotherms are not affected by the presence of hydrogen in the mixture (see Figure 3.2b). This behaviour denotes that methane adsorbs more strongly than hydrogen.

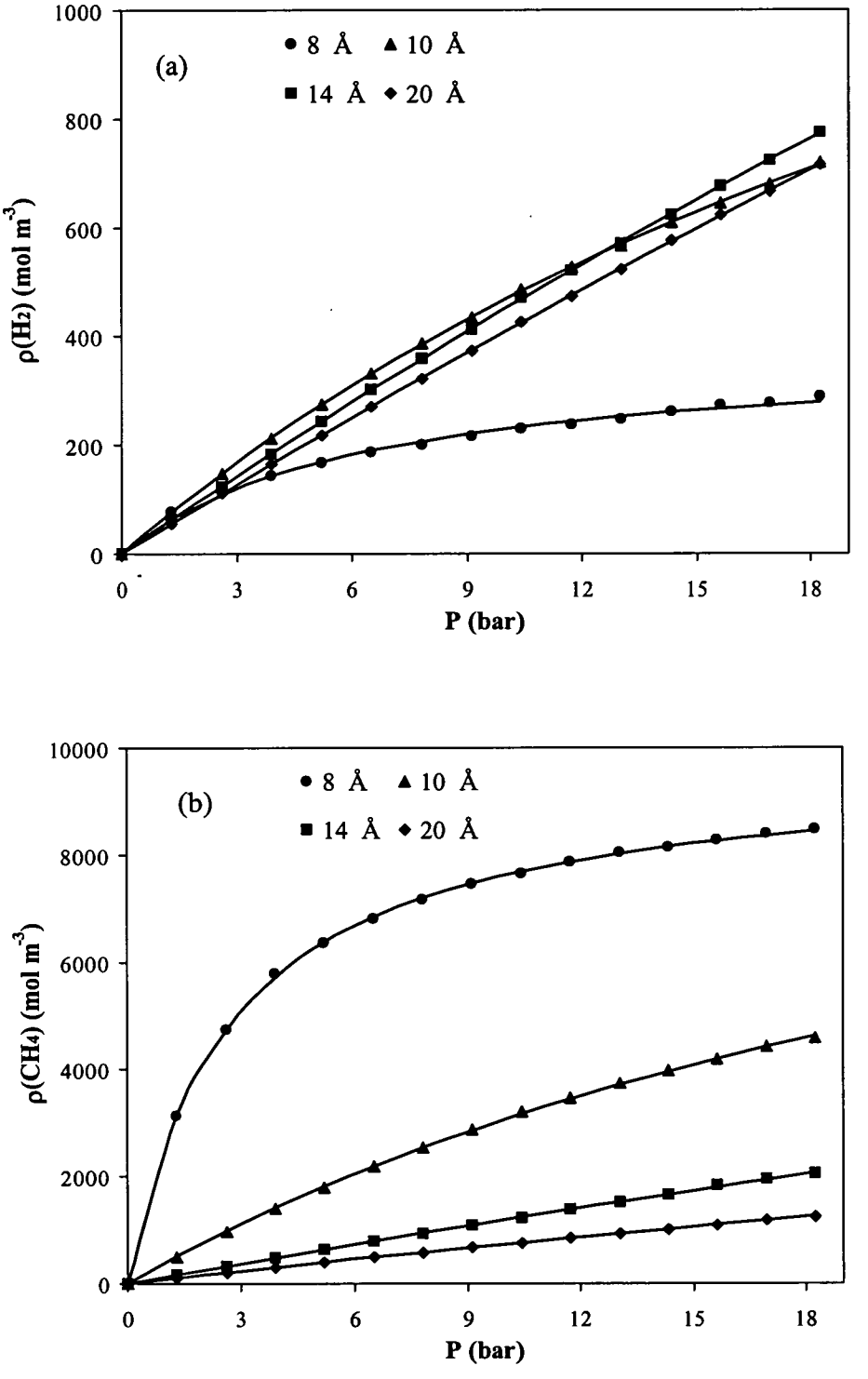

Figure 3.2 – Binary isotherms at different pore sizes at 300 K: a) hydrogen and b) methane. Adsorbed densities are fitted to the Langmuir Isotherm (Equation 3.3).

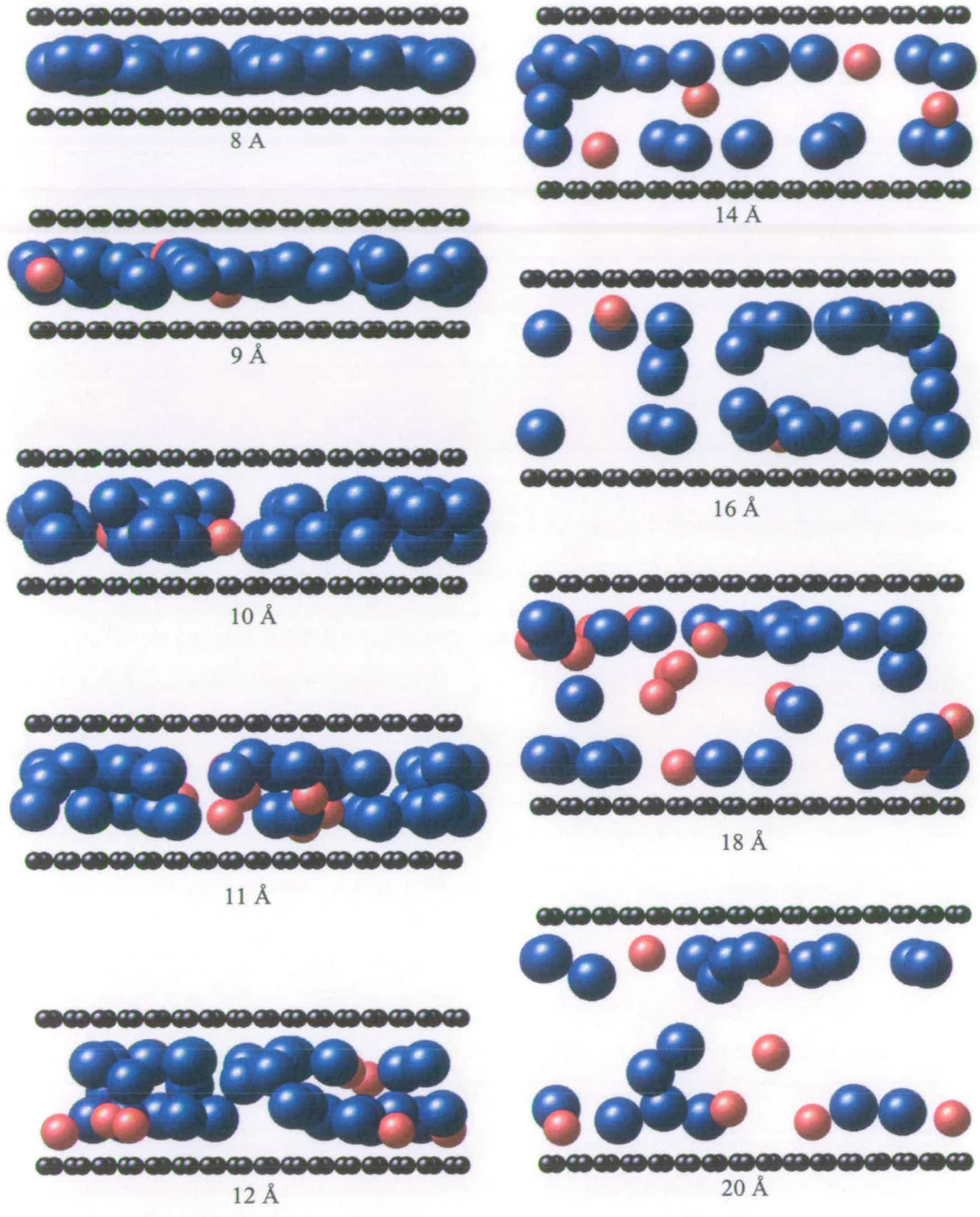

Figure 3.3 – Adsorption simulation snapshot (mixture conditions at 300 K, total pressure 18.25 bar, hydrogen mole fraction of 0.8). Hydrogen is represented in red, methane in blue and carbon atoms from the graphic surface in black. (Note that carbon atoms are not to scale for better visualisation of adsorbed molecules).

3.1.2 Effect of Pore Width on Adsorption Pore Loading

The variation of equilibrium hydrogen density with the pore size at different temperatures (keeping the total pressure and bulk composition constant) is shown in Figure 3.4a. The hydrogen density is significantly influenced by the presence of methane. By comparing the adsorption of the pure-component with the amount adsorbed from the mixture (at the same operating conditions) it is possible to see that hydrogen is almost excluded for pores smaller than 10 – 11 Å (Figure 3.4b). At 500 K, there is not any significant deviation in the adsorbed density from the pure-hydrogen case.

Figure 3.5a shows the variation of equilibrium methane density with the pore size at different temperatures for a mixture of hydrogen/methane. The pure-component density profile is essentially identical to the density profile of the mixture as can be observed from Figure 3.5b. This feature is due to the strong adsorption of methane into the pore. However, methane density drops almost one order of magnitude at 300 K with the increase of the pore size because as space between the walls increases the methane adsorption potential decreases allowing hydrogen molecules to enter more easily into the pore. Similar behaviour is observed when increasing the temperature denoting that methane has a higher heat of adsorption.

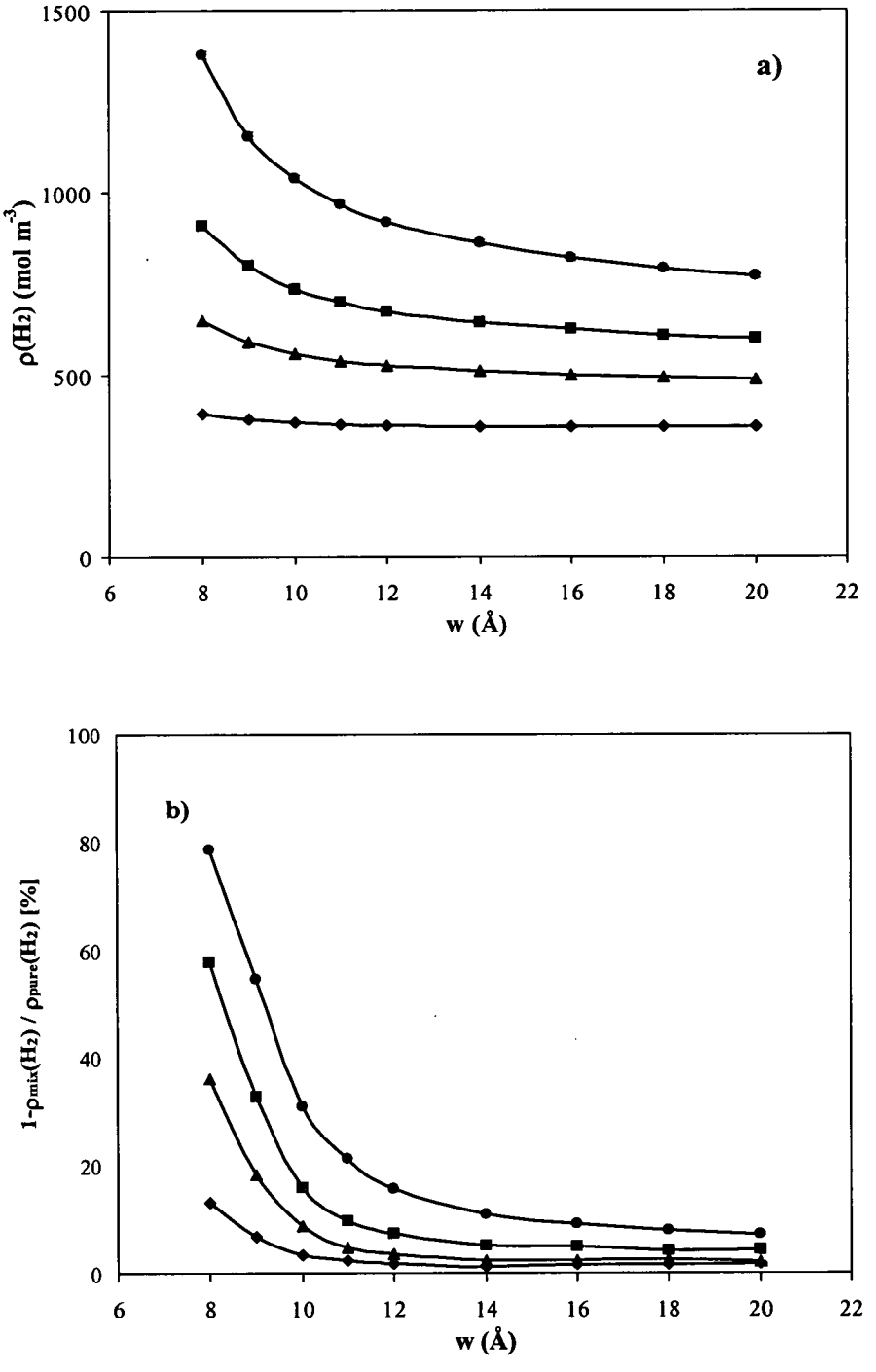

Figure 3.4 – Variation of the adsorbed density with pore width: a) pure hydrogen density and b) density difference between hydrogen in presence of methane and pure hydrogen. Hydrogen partial pressure of 14.60 bar, methane partial pressure of 3.65 bar and temperature of 300 K (circles), 350 K (squares), 400 K (triangles) and 500 K (diamonds). Lines are guide to the eye.

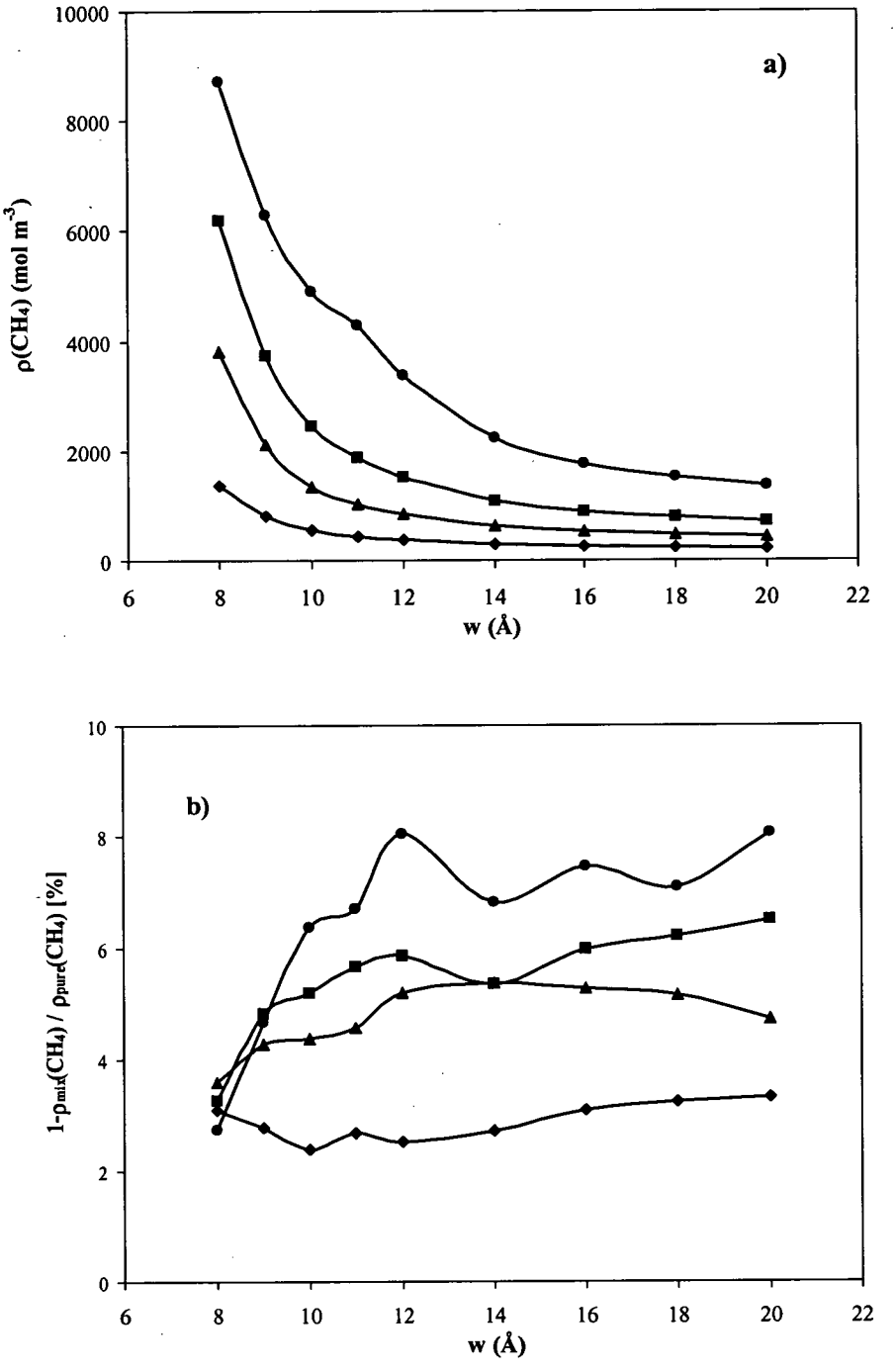

Figure 3.5 – Variation of the adsorbed density with pore width: a) pure methane density and b) density difference between methane in presence of hydrogen and pure methane. Hydrogen partial pressure of 14.60 bar, methane partial pressure of 3.65 bar and temperature of 300 K (circles), 350 K (squares), 400 K (triangles) and 500 K (diamonds). Lines are guide to the eye.

3.1.3 Equilibrium Selectivity

For a binary mixture, the equilibrium selectivity, S^{eq}, is defined by:

$$S^{eq}(CH_4/H_2) = \frac{x_{CH_4} / y_{CH_4}}{x_{H_2} / y_{H_2}} \tag{3.4}$$

were, $x_{CH_4} = \frac{\rho_{CH_4}}{\rho_{H_2} + \rho_{CH_4}}$ is the methane adsorbed mole fraction and $y_{CH_4} = \frac{P_{CH_4}}{P_{H_2} + P_{CH_4}}$ is the methane bulk mole fraction. x_{H_2} and y_{H_2} are the hydrogen adsorbed mole fraction and bulk mole fraction respectively. Values greater than unity imply that methane is more strongly adsorbed than hydrogen. Figure 3.6 shows the equilibrium selectivity of methane over hydrogen for several pore sizes. A decrease of selectivity is observed with increasing pore size and with increasing temperature. For small pores, one observes strong methane adsorption and a maximum of selectivity is observed at about 8 Å, which corresponds to the pore size where the methane molecules are most effectively packed (see simulation snapshots in Figure 3.3). However, as the pore size increases, the void space between the walls increases allowing hydrogen molecules to enter the pore more easily. In addition, as the pore size increases, the isotherms become linear and only selectivity depends only on the ratio of the Henry's constants. In the Henry's law region the adsorbed density is linearly dependent of the bulk phase partial pressure (see Equation 3.1):

$$S^{eq}(CH_4/H_2) = \frac{H_{CH_4}\left(P^0 y_{CH_4}\right)}{y_{CH_4}} \frac{y_{H_2}}{H_{H_2}\left(P^0 y_{H_2}\right)} \tag{3.5}$$

Thus, the selectivity in the Henry's law region does not depend on the composition:

$$S^{eq}(CH_4/H_2) = \frac{H_{CH_4}}{H_{H_2}} \tag{3.6}$$

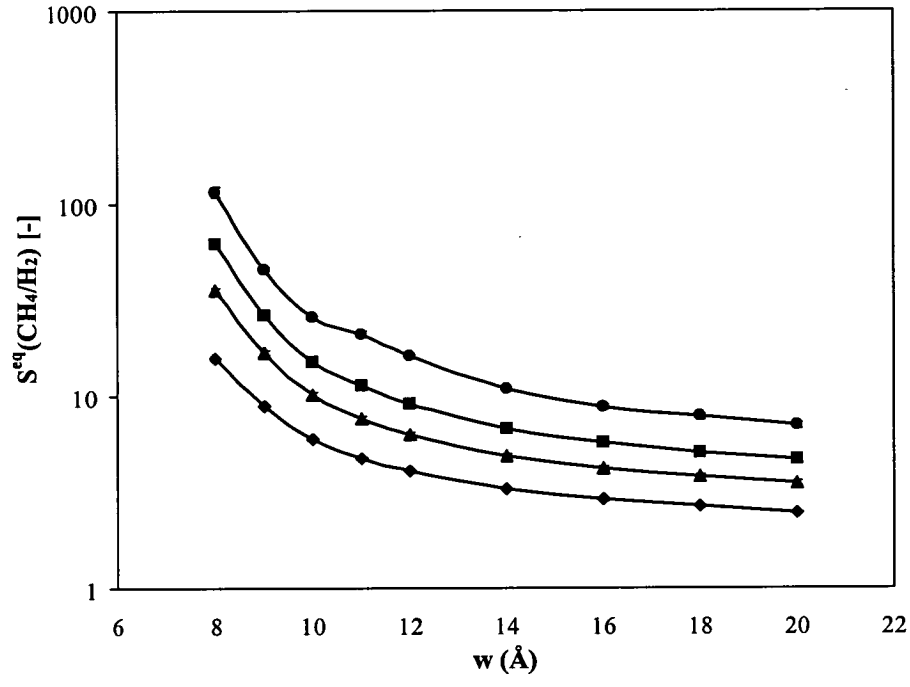

Figure 3.6 – Variation of the equilibrium selectivity with pore width. Total pressure 18.25 bar, hydrogen bulk mole fraction 0.8, methane bulk mole fraction 0.2 and temperature of 300 K (circles), 350 K (squares), 400 K (triangles) and 500 K (diamonds).

3.2 Transport Diffusion in Micropores

There are three well-known macroscopic theories for describing the mass transport behaviour of multicomponent mixtures (Taylor & Krishna, 1993); these include Fick's law, the Onsager theory of irreversible thermodynamics and the Maxwell-Stefan theory. If the diffusion coefficient is independent of concentration then the transport can simply be described using Fick's law (Krishna, 1992). In the Maxwell-Stefan theory microscopic information is included, since mechanical interactions (friction) between the different species are considered explicitly. Although the Onsager theory (Onsager, 1931a; 1931b) of irreversible thermodynamics takes in account the effect of non-idealities, the Onsager diffusion coefficients are normally strong functions of composition (Kärger & Ruthven, 1992). On the other hand, Maxwell-Stefan diffusion coefficients are composition independent (Wesselingh & Krishna, 2000).

3.2.1 Flux in Micropores

Hydrogen net flux as a function of pore size is shown in Figure 3.7. It can be seen in Figure 3.7a that the pure hydrogen flow shows a linear dependence on pore size (as we will see in Section 3.3, this linear dependence is characteristic of Knudsen diffusion). In addition, the pure-hydrogen flux is found to be inversely proportional to the temperature. On the other hand, the hydrogen flux in the binary mixture is significantly reduced by the presence of methane. From Figure 3.7b, it can be seen that the hydrogen flux starts roughly at zero denoting a significant pore blockage by the adsorbed molecules of methane - the more strongly adsorbed species (see Figure 3.3). This blockage effect is more considerable at low temperatures where methane adsorbs strongly as previously described in Section 3.1. Thus, the hydrogen flux increases with temperature in pores smaller than about 10 to 12 Å because as the temperature increases the methane density decreases giving more space for hydrogen molecules to flow.

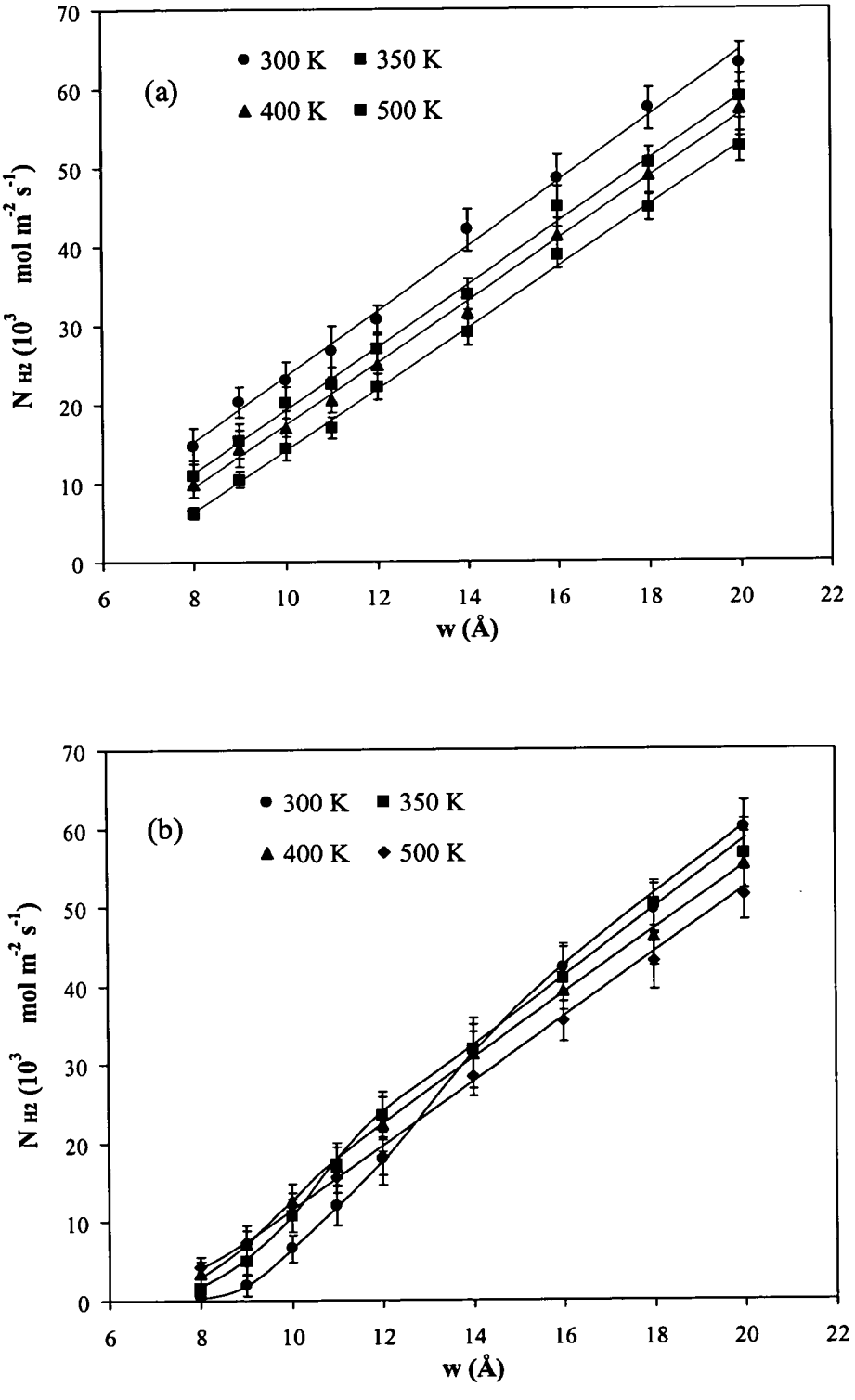

Figure 3.7 - Variation of hydrogen net flux with pore size for a) pure hydrogen and b) hydrogen in the presence of methane. Partial pressure of hydrogen is 14.6 bar, partial pressure of methane is 3.65 bar.

Figure 3.8 shows the variation of the pure-methane flux with the pore size. It can be seen that the methane flux has a maximum at about 9 Å, corresponding to the pore size where methane molecules are more easily transported. The flux seems to be almost independent of pore size in pores bigger than 14 Å. The methane flux in the presence of hydrogen is not shown because it is not significantly influenced by the presence of hydrogen. [In small pore, the hydrogen molecules are excluded from entering in the pores because methane adsorbs more strongly than hydrogen. On the other hand, as will be shown in Section 3.3 the hydrogen molecules and the methane molecules flow in different regions in larger pores.]

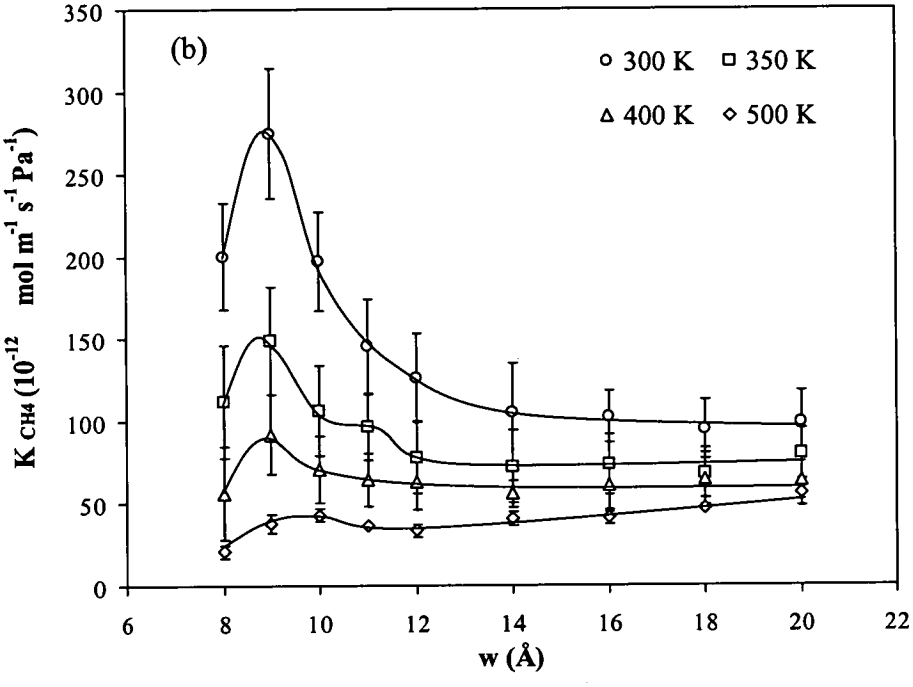

Figure 3.8 - Variation of pure-methane permeability in presence of hydrogen. Partial pressure of hydrogen is 14.6 bar, partial pressure of methane is 3.65 bar.

3.2.2 Generalised Maxwell-Stefan Theory

In this thesis, the Generalised Maxwell-Stefan (GMS) approach is used to calculate diffusion coefficients because the Maxwell-Stefan diffusion coefficients are composition independent (Wesselingh & Krishna, 2000; Kärger & Ruthven, 1992).

The GMS theory uses microscopic information about intermolecular friction between different species. Krishna (1990) looked into the application of the GMS theory for transport in microporous materials (see Figure 3.9). In his work, vacancies (*i.e.* vacant surface sites) are regarded as pseudo-species. The vacancy species flux, N_v, must balance the fluxes of the others diffusing species, N_i. Thus, the summation of all fluxes must cancel (*i.e.* $\sum_{i=1}^{n}(N_i)+N_v=0$).

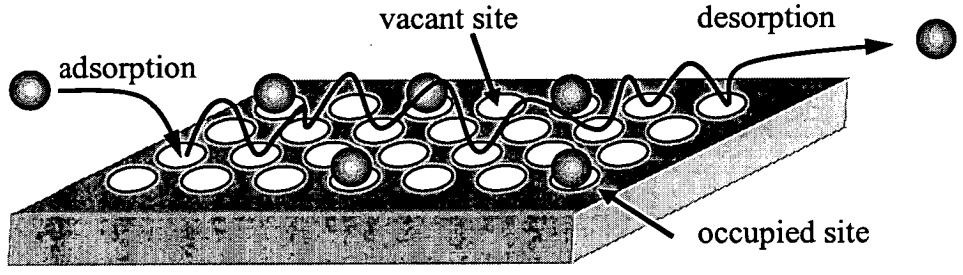

Figure 3.9 – Schematic representation showing the surface adsorption/diffusion sites (represented by white circles). Line represents the adsorbed molecules jumps between sites.

Considering vacancies as pseudo-species can create some controversy since they cannot be regarded as real particles to which mass and chemical potential can be assigned. Nevertheless, the GMS formulation has been applied successfully to describe transient uptake in zeolites, carbon molecular sieves and zeolitic membrane permeation (Kapteijn, Moulijn & Krishna, 2000; Krishna. & van den Broeke, 1995). If a pressure gradient is present, viscous transport occurs through the pore. Thus, the viscous flux contribution simply adds to the diffusional flux (Kärger & Ruthvem, 1992). The GMS diffusion equation is given by (Krishna, 1990; 1993):

$$-\frac{\theta_i}{RT}\nabla\mu_i-\theta_i\frac{B_0}{\eta Đ_i}\nabla P=\sum_{\substack{j=1\\ i\neq j}}^{n}\frac{\theta_j N_i-\theta_i N_j}{m_0 Đ_{ij}}+\frac{N_i}{m_0 Đ_i} \tag{3.7}$$

The left-hand side of the equations reflects the driving force, expressed in terms of a chemical potential gradient ($\nabla\mu_i$) and a gradient of total pressure (∇P), acting on

species i. η is the viscosity of the mixture, P is the total pressure and B_o is a parameter characteristic of the membrane. In a slit pore $B_0 = \frac{w^2}{12}$. The first term of the right-hand side reflects the friction between different adsorbate species i and j ($Đ_{ij}$). The second term reflects friction between species i and the surface ($Đ_i$). According to Krishna (1992; 1993) $Đ_i$ is independent of surface coverage. The fractional occupancies (surface coverage), θ_i, are defined as

$$\theta_i = \frac{\rho_i}{m_0} \tag{3.8}$$

To have thermodynamic consistency, the saturation loading (m_0) for all the species must be equal (Kapteijn, Moulijn & Krishna, 2000). Thus,

$$\sum_{i=1}^{n+1} \theta_i = 1 \tag{3.9}$$

where, $n+1$ term corresponds to the occupancy of the vacancies.

3.2.3 Importance of Viscous Flow and Cross Diffusion Coefficients

Before simplifying Equation 3.7 we need to determine the relative importance of each term (*i.e.* viscous flow and cross-diffusion) on the total flow. We followed an GMS alternative treatment developed by Mason & Viehland (1978). For binary diffusion in porous membranes, the treatment of Mason and co-workers leads to the following expression:

$$J_i = -L_{ii} \nabla \mu_i - L_{ij} \nabla \mu_j - \frac{B_o \rho_i}{\eta} \nabla P \tag{3.10}$$

L_{ij} are the phenomenological coefficients of Onsager (1931a; 1931b), which are postulated by microscopic reversibility to obey the reciprocity relations $L_{ij} = L_{ji}\big|_{i\neq j}$ (Cussler 1997). This method is an alternative to the GMS equations of diffusion and it has the advantage of been easier to put into practice. However, the disadvantage of using Equation 3.10 is that the phenomenological coefficients are strong functions of concentration:

$$L_{ij} = D_{ij}\frac{\rho_i}{RT} \tag{3.11}$$

For isothermal mass transport in a simple binary mixture the non-equilibrium thermodynamic treatment leads to three independent diffusion coefficients (D_{11}, D_{22} and D_{12}):

$$\begin{cases} N_1 = -D_{11}\dfrac{d\rho_1}{dx} - D_{12}\dfrac{d\rho_2}{dx} - \dfrac{B_o\,\rho_1}{\eta}\nabla P \\ N_2 = -D_{22}\dfrac{d\rho_2}{dx} - D_{21}\dfrac{d\rho_1}{dx} - \dfrac{B_o\,\rho_2}{\eta}\nabla P \end{cases} \tag{3.12}$$

In Equation 3.12, $D_{21} = \dfrac{x_2}{x_1}D_{12}$ because $L_{ij} = L_{ji}\big|_{i\neq j}$ (Cussler 1997). In addition, Mason & Malinauskas (1983) showed that the phenomenological diffusion coefficients, in a binary mixture, are related to the three Maxwell-Stefan pair diffusivities by:

$$D_{11} = \frac{\dfrac{x_1}{Đ_{12}} + \dfrac{1}{Đ_2}}{\left(\dfrac{x_1}{Đ_1} + \dfrac{x_2}{Đ_2}\right)\dfrac{1}{Đ_{12}} + \dfrac{1}{Đ_1 Đ_2}}, \tag{3.13}$$

$$D_{22} = \frac{\dfrac{x_2}{Đ_{12}} + \dfrac{1}{Đ_1}}{\left(\dfrac{x_1}{Đ_1} + \dfrac{x_2}{Đ_2}\right)\dfrac{1}{Đ_{12}} + \dfrac{1}{Đ_1 Đ_2}}, \tag{3.14}$$

$$D_{12} = \frac{\frac{x_1}{Đ_{12}}}{\left(\frac{x_1}{Đ_1} + \frac{x_2}{Đ_2}\right)\frac{1}{Đ_{12}} + \frac{1}{Đ_1 Đ_2}} \tag{3.15}$$

where $Đ_{11}$ and $Đ_{22}$ are the GMS main diffusion coefficients and $Đ_{12}$ is the cross diffusion term (*i.e.* reflects the friction between different adsorbate species *i* and *j*). However, if the cross diffusion coefficients are negligible relative to the main diffusion coefficients Equations 3.13 – 3.15 reduce to: $Đ_{11} = D_{11}$ and $Đ_{22} = D_{22}$.

Using local equilibrium adsorption isotherms one can relate the adsorbed densities (in Equation 3.12) to the pressure. The phenomenological diffusion coefficients shown in Figure 3.10 were obtained by simultaneously solving numerically Equation 3.12 and optimising the variables of interest (D_{11}, D_{12}, D_{22} and η). The diffusion coefficients shown represent the best fit of the simulated density profile (a example of which is shown in Figure 3.12). The cross-coefficient terms (D_{12} and D_{21}) are found to be about four to six orders of magnitude smaller than main-coefficients. In addition, the main diffusion terms are almost independent of viscosity, which suggests that viscosity is unimportant in our pore width range. [If the viscosity is smaller than about 10^{-4} - 10^{-3} kg m^{-1} s^{-1} there is not any diffusion coefficient that gives, for example, the density profile shown later in figure 3.12. The order of magnitude of viscosity (Atkins, 1994; Reid, Prausnitz & Toling, 1987) typically varies between 10^{-5} kg m^{-1} s^{-1} (for gases) and 10^{-3} kg m^{-1} s^{-1} (for liquids).] To verify if the viscous flow is indeed negligible, equilibrium self-diffusion coefficients at constant pressure (*i.e.* in the absence of viscous flow) were calculated via EMD (see Section 2.2.3) using the feed-side conditions. Equilibrium self-diffusion coefficients are also shown in Figure 3.10. It can be seen from Figure 3.10 that there is no evident of viscous flow because the transport diffusion coefficients are in conformity with the self-diffusion coefficients. Since we did not find any evidence that either the viscous flow or the cross-diffusion coefficients contribute significantly to the total flux, we conclude that the GMS equations (described by Equation 3.7) can be simplified further.

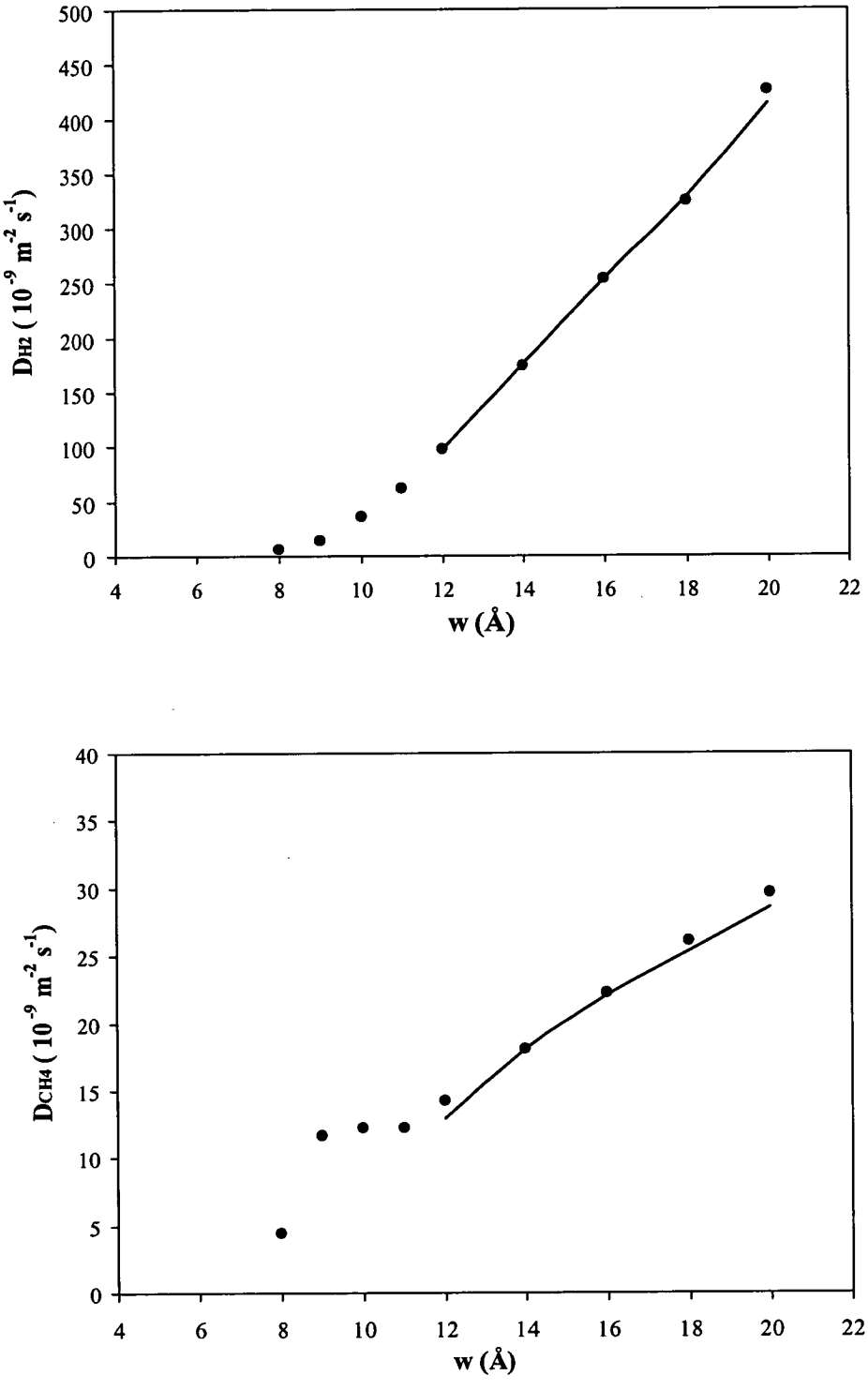

Figure 3.10 – Comparison between transport diffusion (symbols) and self-diffusion coefficients (solid line). Temperature is 300 K, hydrogen partial pressure is 14.6 bar, methane partial pressure is 3.65 bar.

3.2.4 Calculation of Diffusion Coefficients

After we have verified that the contribution of viscous flow and cross diffusion coefficients to the total flux is not important in our pore size range, Equation 3.7 can be simplified to:

$$-\frac{\theta_i}{RT}\nabla\mu_i = \frac{N_i}{m_0 \mathcal{D}_i} \tag{3.16}$$

The chemical potential is related to the fugacity of the adsorbing fluid, f_i, by:

$$\mu_i = \mu_i^0 + R\,T\ln\left(\frac{f_i}{f_i^0}\right) \tag{3.17}$$

where the superscript, *0*, denotes the reference state. Assuming equilibrium between the pore surface and the bulk gas phase, the chemical potential gradient of Equation 3.16 can be expressed in terms of gradients of the surface occupancies:

$$\frac{\theta_i}{RT}\nabla\mu_i = \sum_{j=1}^{n}\Gamma_{ij}\nabla\theta_i \tag{3.18}$$

where n is the number of species and Γ_{ij} is the Darken thermodynamic factor:

$$\Gamma_{ij} \equiv \theta_i \frac{\partial \ln(f_i)}{\partial \theta_j} \tag{3.19}$$

However, one needs to keep the fugacity of species j constant to simplify the Darken thermodynamic factor (because Γ_{ij} is a function of the composition of both species). By keeping the fugacity of species j constant one gets that $\Gamma_{jj} = 0$. Thus, Equation 3.18 (that is the left-hand side of the Equation 3.16) can be further simplified to:

$$\frac{\theta_i}{RT}\nabla\mu_i = \Gamma_{ii}\nabla\theta_i \tag{3.20}$$

Finally one gets that the flux of species *i* is given by:

$$N_i = -m_0\,\Gamma_i\,Đ_i\,\nabla\theta_i \tag{3.21}$$

For pure-hydrogen, where the isotherms are linear (Figure 3.1a), the Darken thermodynamic factor ($\Gamma_{H_2} = 1$) becomes unity and Equation 3.21 reduces to the Fickian form:

$$N_i = -Đ_i\nabla\rho_i \tag{3.22}$$

where $\rho_i = m_0 \times \theta_i$. On the other hand, the Darken thermodynamic factor for methane is a function of composition. For the Langmuir isotherm (see Equation 3.3) one obtains that: $\Gamma_{CH_4} = \dfrac{1}{1-\theta_{CH_4}}$ via Equation 3.19.

Figure 3.11 shows variation of the pure-methane Darken thermodynamic factor with the pore size. The Darken factor is close to unity, for all temperatures, in pores wider that about 12 Å. If the Darken factor does not depend significantly on the local composition (in pores wider than 12 Å) a linear density profile along the pore is obtained (like the profile shown in Figure 3.12b). Otherwise, the profiles are influenced by the local composition (see Figure 3.12a). [In Figure 3.12, the simulated pure-methane composition profiles along the pore length (expressed in terms of surface coverage) are shown.]

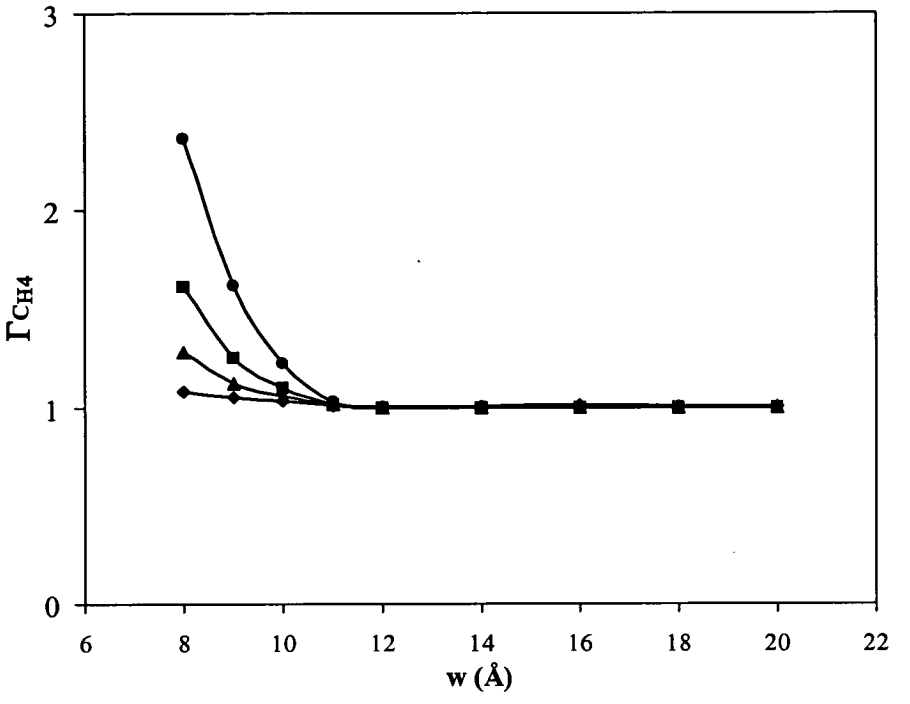

Figure 3.11 – Variation of pure-methane Darken thermodynamic factor with the pore size at 300 K (circles), 350 K (squares), 400 K (triangles) and 500 K (diamonds). Methane pressure is 3.65 bar. Solid line is a guide to the eye.

From our GCMC simulations, we obtain information about local equilibrium composition (equilibrium isotherms). In our non-equilibrium GCMD simulations, we keep the chemical potential of one of the species constant while analysing the other species. The GCMD method provides fluxes and density profiles. The Euler method (see *e.g.*, Press *et al.*, 1986) is used to solve numerically Equation 3.21. Thus, diffusion coefficients are calculated by simultaneously solving and fitting Equation 3.21 to our simulation results. All optimisations are made using the Microsoft Excel Solver. The optimisation variables are the main-diffusion coefficients. A comparison between the composition profile (expressed in terms of surface coverage) obtained from our GCMD simulations and the composition profile obtained from Equation 3.21 is shown in Figure 3.12. It can be seen than there is a good agreement between our simulation results and GMS equations.

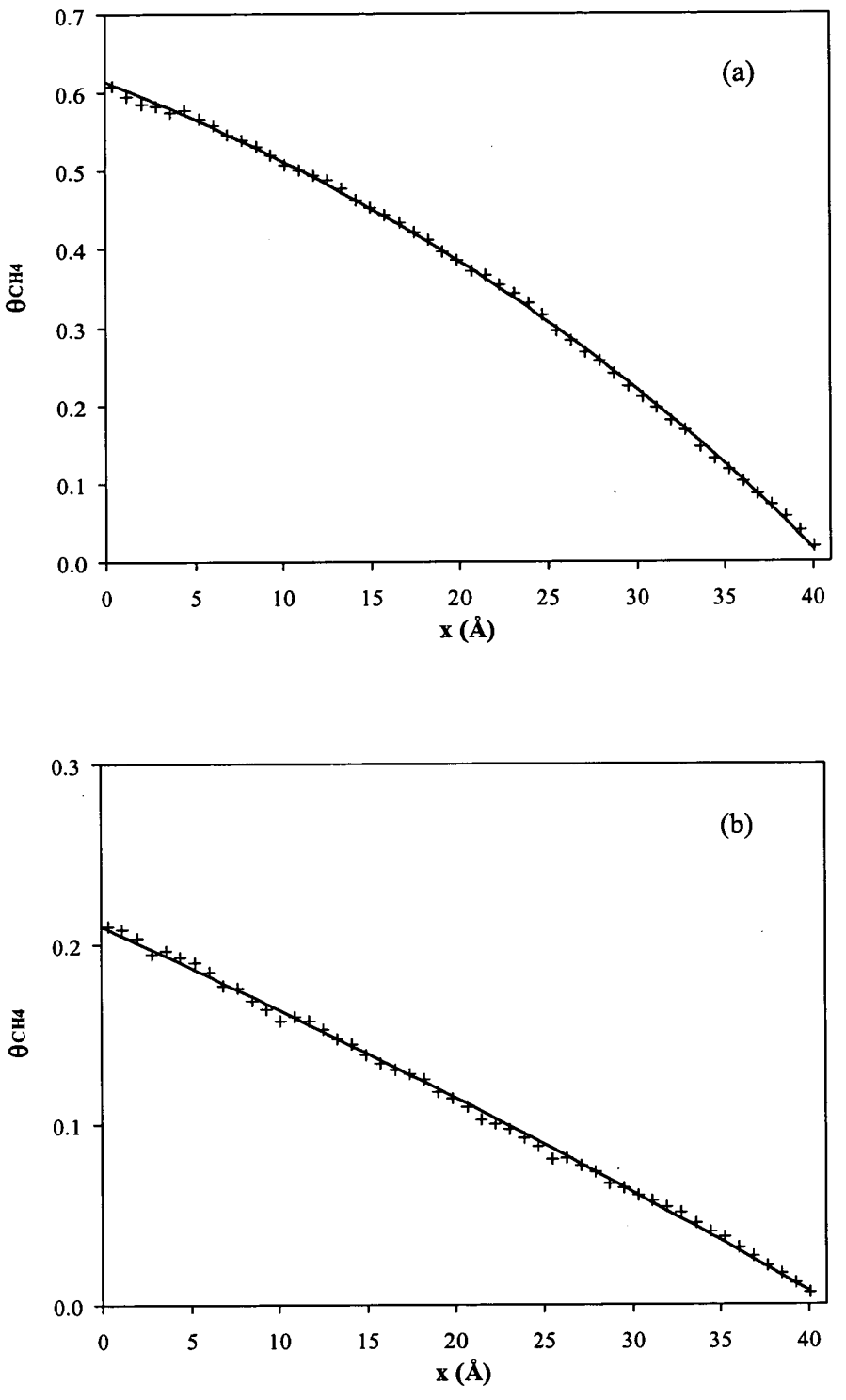

Figure 3.12 – Pure-methane coverage profile along the pore length for a pore size of a) 9 Å and b) 14 Å. Symbols represent coverage from simulation and solid line represents fit to GMS Equation 3.21. Temperature is 300 K, and pressure is 3.65 bar.

3.2.5 Variation of Diffusion with Composition

To investigate the influence of loading on the methane diffusivity, we calculated Maxwell-Stefan diffusion coefficients at different pure-methane loadings. Different loadings are achieved by adjusting the feed-side pressure. Figure 3.13 shows that diffusivities calculated by the GMS equations are essentially composition independent as suggested by Krishna (1992). This provides evidence to support the applicability of GMS equations (via Equation 3.21) to describe mass transport in our micropore range. The pore width analysed is 9 Å, which corresponds to the maximum of methane flux (see Figure 3.8).

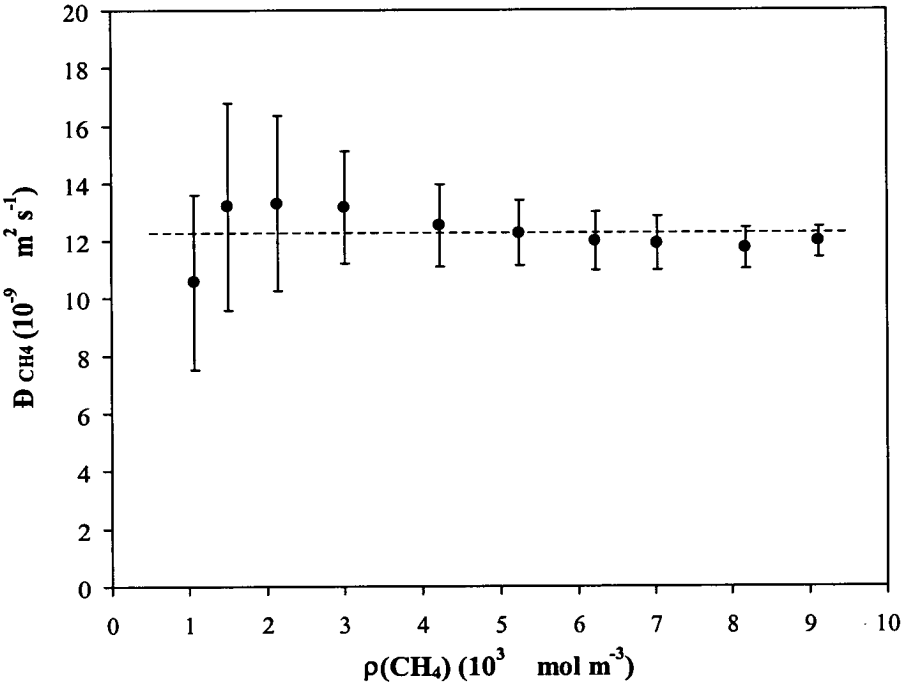

Figure 3.13 - Variation of the methane diffusion coefficient with methane loading. Horizontal dashed line corresponds to the average diffusion coefficient. Temperature 300 K and pore width 9 Å.

3.2.6 Variation of Diffusion with Pore Size and Temperature

Figure 3.14 shows the variation of the hydrogen diffusion coefficient as function of pore size (when the chemical potential of methane is kept constant). In pores wider than 12 Å, the variation of the diffusion coefficient with the pore width is linear and is also proportional to the temperature. As we will see in Section 3.3, this linear dependence is characteristic of Knudsen diffusion. A diminution of the hydrogen diffusion coefficient in the presence of methane is observed in particular for small pores because of the pore blockage effect of methane over hydrogen. However, as the pore size increases the diffusion coefficients show the same behaviour as for the pure-component.

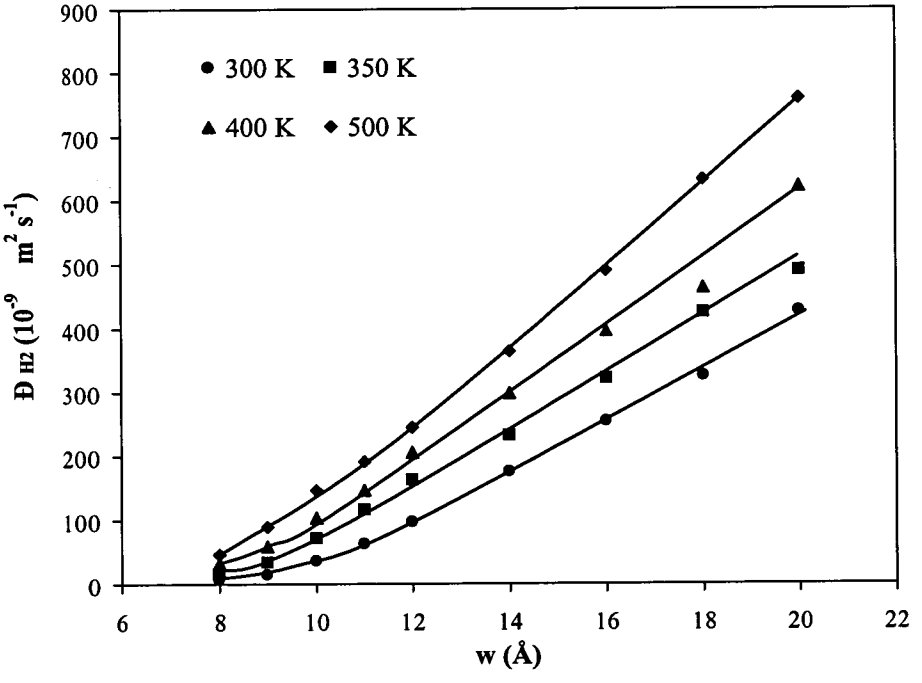

Figure 3.14 – Variation of hydrogen diffusion coefficients, in presence of methane (pressure of methane is 3.65 bar), with the pore size.

Figure 3.15 shows the ratio between the hydrogen diffusion coefficient (in the presence of methane) and the pure-hydrogen diffusion coefficient at 300 K. The effect of pore blockage by methane molecules is evident in pores smaller than 14 Å,

where the hydrogen diffusion (in the presence of methane) is about 10 % of pure-hydrogen diffusion at 8 Å. However, this value increases to about 90 % at 20 Å because the hydrogen molecules are mainly in the mid pore channel while the methane molecules are essentially located on the pore surface.

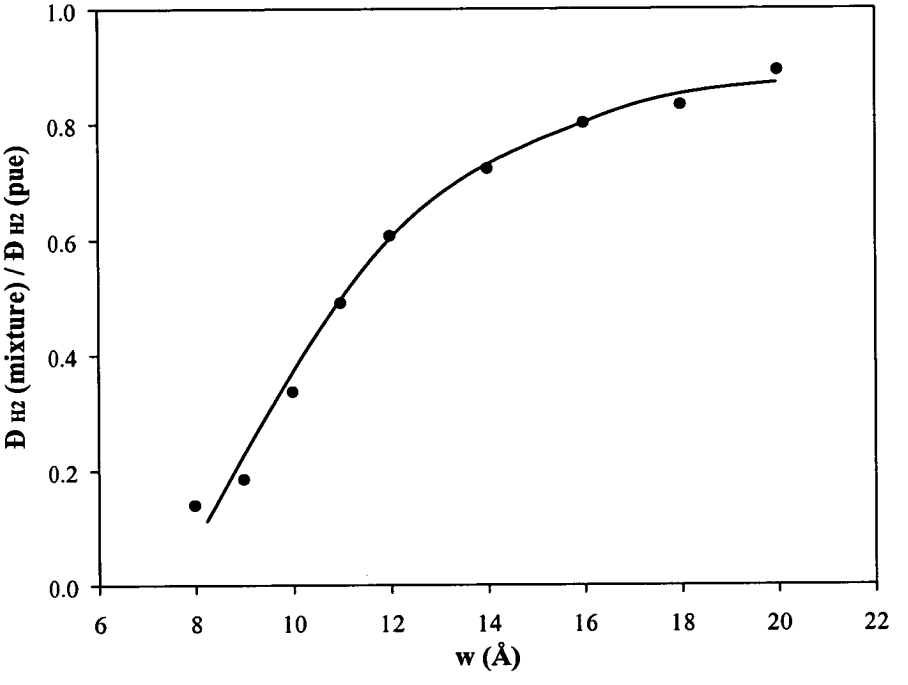

Figure 3.15 – Ratio between hydrogen diffusion (in presence of a methane) and pure hydrogen diffusion at 300 K (hydrogen partial pressure is 14.6 bar).

Figure 3.16 shows the variation of the methane diffusion coefficient with the pore width when the chemical potential of hydrogen (corresponding to a hydrogen partial pressure of 14.6 bar) is kept constant. The presence of hydrogen in the mixture does not change significantly the methane diffusion coefficient relative to the pure methane diffusion. In pores smaller than about 10 - 12 Å, the hydrogen molecules are excluded from the pore. Methane molecules form a tight mobile phase in which steric restrictions may prevent molecules from passing one another (Kärger & Ruthven, 1992). This particular motion of diffusing molecules along a one-dimensional channel is designated by single-file diffusion. However, in our simulations molecules diffuse in a slit-like pore (*i.e.* along two-dimensions). Thus,

we expect single-file diffusion effects not to be significant in our system because diffusive molecules can pass one another more easily. In pores larger than about 12 Å, the methane molecules are transported near the wall while the hydrogen molecules flow in the middle pore region (see Figure 3.3). At 300 K, methane diffusion shows a maximum at about 9 – 10 Å. This maximum is only evident at low temperatures (and becomes a point of inflection at 350 K or higher temperatures). This maximum corresponds to a pore size immediately before the formation of two distinct adsorbed layers of methane on the surface (this effect is more clear in the snapshots shown in Figure 3.3). In addition, the diffusion coefficients increase with the temperature for both species and for all the pore sizes.

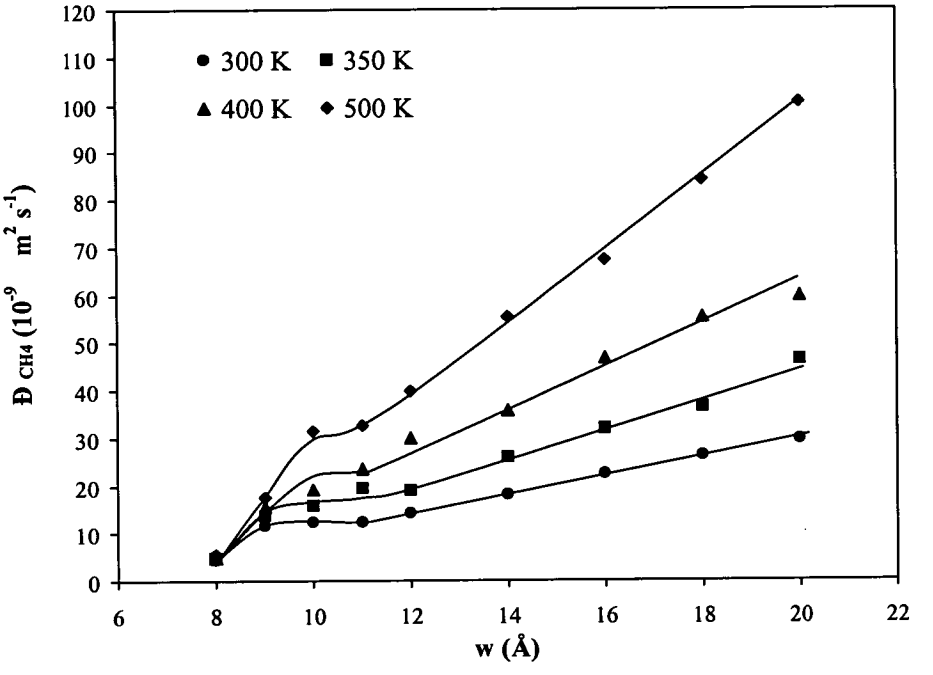

Figure 3.16 – Variation of methane diffusion coefficients, in presence of hydrogen, with the pore size at 300 K (circles), 350 K (squares), 400 K (triangles) and 500 K (diamonds). The hydrogen partial pressure is 14.6 bar.

3.2.7 Permeabilities

The permeability through a porous membrane is analogous to a mass transfer coefficient, *i.e.* the flux per unit of the driving force (*e.g.* concentration, partial pressure). The molar flux, N_i, of species "*i*" across a membrane is (*e.g.* Cussler, 1997):

$$N_i = \left(\frac{K_i}{L_x}\right) \times \Delta P_i \tag{3.23}$$

where K_i is the pore permeability of the membrane to component *i*, ΔP_i is the difference in the partial pressure of component i across the pore and L_x the membrane thickness.

As described previously in Section 2.5, there is a small discontinuity in the longitudinal density profile at the ends of the transport region particularly when the pore gets wider than about 10 Å. Thus, Equation 3.23 cannot be used, directly, to calculate the permeability because the concentration gradient in the transport region is less than the concentration gradient defined between the two GCMC regions. To calculate the permeability one first integrates the flux Equation 3.21 over the membrane thickness:

$$\int_0^{L_x} N_i \, dz = -m_0 \int_{\theta_i^0}^{0} \frac{Đ_i}{1-\theta_i} d\theta_i \tag{3.24}$$

The surface coverage (or adsorbed density) at the exit of the membrane is zero because we use a zero-density sink as the permeate side. Thus, the flow of component *i* across the membrane is given by

$$N_i = -\frac{m_0 \, Đ_i}{L_x} \ln\left(1-\theta_i^0\right) \tag{3.25}$$

The permeability equation is obtained by equating Equation 3.23 and Equation 3.25:

$$K_i = -\frac{Đ_i\, m_0}{\Delta P_i} \ln\left(1-\theta_i^0\right) \tag{3.26}$$

The permeability plots have a similar shape to the corresponding component flux shown in Figure 3.7 and Figure 3.8 because they are both related via Equation 3.23. Thus, similar conclusions are drawn. For pores larger than about 12 – 14 Å, an inverse dependence of the permeabilities on temperature is observed and a linear dependence on pore size is observed for pure-hydrogen (Figure 3.17a). However, the hydrogen permeability is significantly affected by the presence of methane denoting a strong pore blockage by the methane adsorbed molecules causing the hydrogen permeability to fall. Figure 3.17b shows the variation of the methane permeability with pore size. It can be seen that there is a maximum of permeability, at about 9 Å, corresponding to the pore size where methane molecules are easily transported.

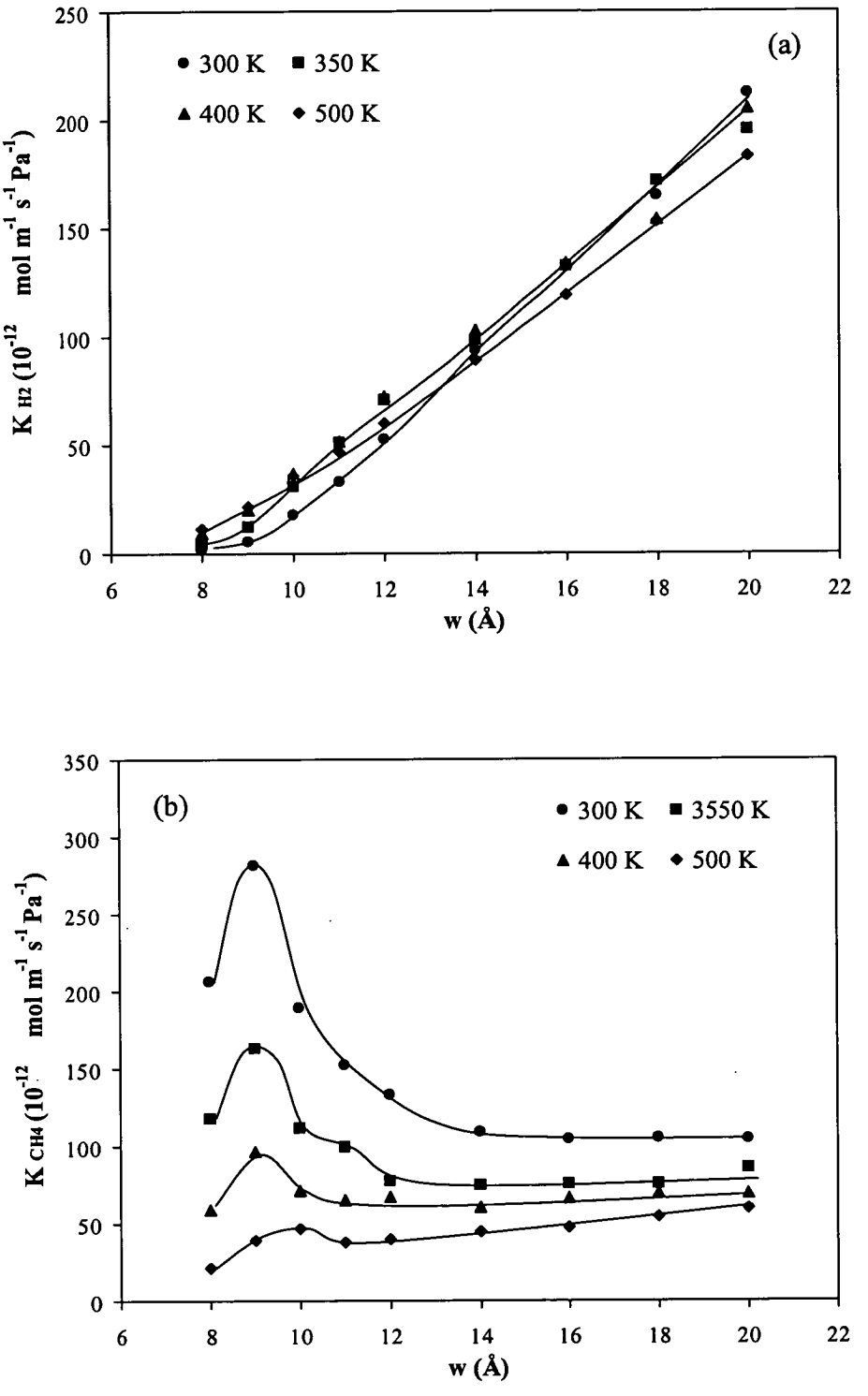

Figure 3.17 - Variation of permeability for a) hydrogen in the presence of methane and b) methane in presence of hydrogen (hydrogen partial pressure is 14.6 bar and methane partial pressure is 3.65 bar).

3.2.8 Kinetic Selectivity

The effectiveness of the separation is quantified by the kinetic selectivity S^k, which is defined as the ratio of the permeabilities of the two components in the mixture:

$$S^K{}_{(CH_4/H_2)} = \frac{K_{CH_4}}{K_{H_2}} \tag{3.27}$$

In Figure 3.18, the kinetic selectivity of methane over hydrogen is plotted as a function of pore size at different temperatures. It can be seen that the separation decreases considerably with increasing pore size - *i.e.* with the increase in the volume available for hydrogen flow. High selectivity arises from the exclusion of hydrogen from the pore by the adsorption of methane (as seen previously in Figure 3.3). The selectivity gets lower than unity (poor separation) in pores wider than 14 Å and 10 Å at 300 K and 500 K because as the pore gets wider the middle-pore free space for hydrogen increases. Hydrogen molecules are smaller and lighter (compared with methane molecules). Thus, hydrogen will diffuse faster than methane leading to a decrease of the selectivity as the pore size increases.

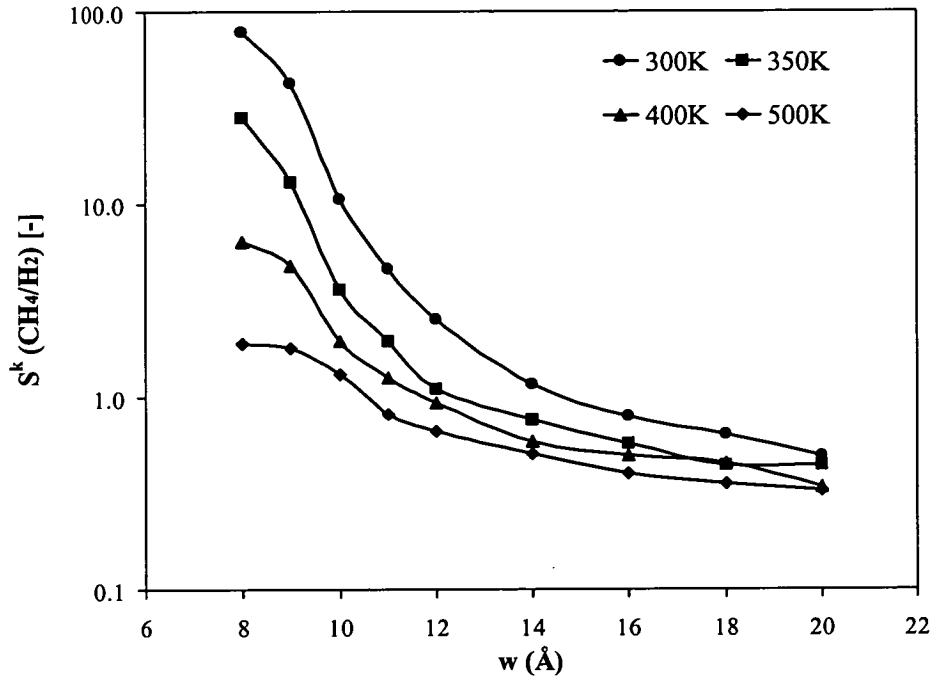

Figure 3.18 - Variation kinetic selectivity with pore size. Pressure of 18.25 bar, hydrogen mole fraction of 0.8 and methane mole fraction of 0.2. Lines are guide to the eye.

Figure 3.19 shows the difference between equilibrium and kinetic selectivities. The equilibrium selectivity (see Figure 3.6) corresponds to the maximum separation that one can obtain in a SSF membrane. The minimum shown in Figure 3.19 at 300 K and at 9 Å correspond to bad simulation statistics. Selective methane adsorption occurs in small pore sizes and the hydrogen molecules are prevented from entering in the pore making difficult to accurately compute the hydrogen density (in some of our simulations we have about 1 hydrogen molecule per 200 methane molecules). Kinetic selectivities are smaller than equilibrium selectivities because the species have different velocities of diffusion. By substituting GMS diffusion equation (Equation 3.21) in the equation of the permeability (Equation 3.27), one gets:

$$S^k{}_{(CH_4/H_2)} = \frac{\Gamma_{CH_4} Đ_{CH_4} \nabla\theta_{CH_4}}{\Delta P_{CH_4}} \frac{\Delta P_{H_2}}{\Gamma_{CH_2} Đ_{H_2} \nabla\theta_{H_2}} \tag{3.28}$$

By approximating the derivatives by finite differences (we use zero-density sink as permeate in our simulations):

$$S^{k}{}_{(CH_4/H_2)} = \frac{P^0_{H_2}}{P^0_{CH_4}} \frac{\theta^0_{CH_4}}{\theta^0_{H_2}} \frac{\Gamma^0_{CH_4}}{\Gamma^0_{H_2}} \frac{Đ_{CH_4}}{Đ_{H_2}} \tag{3.29}$$

Thus,

$$S^{k}{}_{(CH_4/H_2)} = S^{eq}{}_{(CH_4/H_2)} \frac{\Gamma^0_{CH_4}}{\Gamma^0_{H_2}} \frac{Đ_{CH_4}}{Đ_{H_2}} \tag{3.30}$$

This result shows that the kinetic selectivity is proportional to the ratio of Maxwell-Stefan diffusivities and to the ratio of the thermodynamic factors.

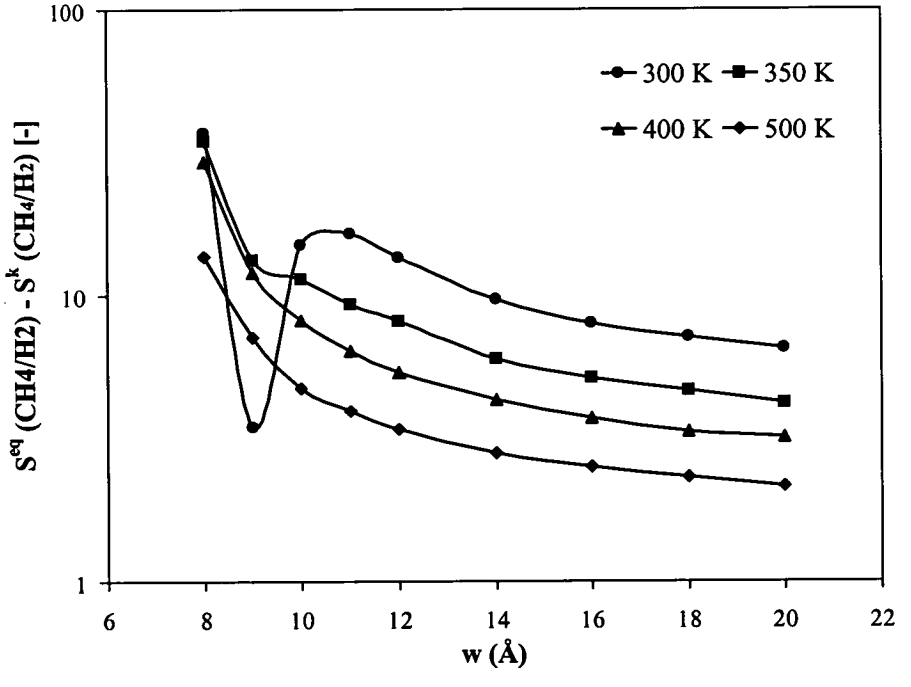

Figure 3.19 – Difference between equilibrium and kinetic selectivities with pore size. Pressure of 18.25 bar, hydrogen mole fraction of 0.8.

3.3 Transport Mechanisms in Micropores

As we have described in Chapter 1, different basic transport mechanisms can occur in a microporous membrane (Seader & Henley, 1998 and Cussler, 1997) according to the nature of the fluid and membrane. The basic transport mechanisms relevant to the microporous carbon membranes are viscous flow, Knudsen diffusion and surface diffusion. Molecular sieving is a particular type of microprous carbon membrane, in which the separation is based in different molecular sizes (see *e.g.*, Koresh & Soffer, 1987). According to Wesselingh & Krishna (1997), viscous and Knudsen diffusion mechanisms occur together and it is prudent to take both mechanisms into account rather than assuming that one mechanism is "controlling". On the other hand, surface diffusion occurs in parallel (by analogy to an electric circuit) to the other two mechanisms and its contribution to the total flux may be quite significant particularly in micropores (Do, 1997; Kärger & Ruthven, 1992; Ruthven, 1984). Surface diffusion coefficients are strong functions of temperature and surface concentration. The surface diffusion coefficient dependence on the temperature is given by (Do, 1997; Glicksman, 2000; Kärger & Ruthven, 1992):

$$D^{s0} = D^{s\infty}\, e^{\frac{E_a}{RT}} \tag{3.31}$$

where D^{s0} is the surface diffusivity at zero-coverage, $D^{s\infty}$ is the surface diffusivity at infinite temperature and E_a is the activation energy for surface diffusion.

The following figure shows the electrical analogue circuit representation of the various contributions to the total flow of the different transport mechanisms inside a membrane pore. We note that Bell & Brown (1974) developed one more complex model derived from momentum balances that take into account interactions between the gas and the mobile adsorbed phases. However, in the current work we followed the simple model described by Wesselingh & Krishna (1997).

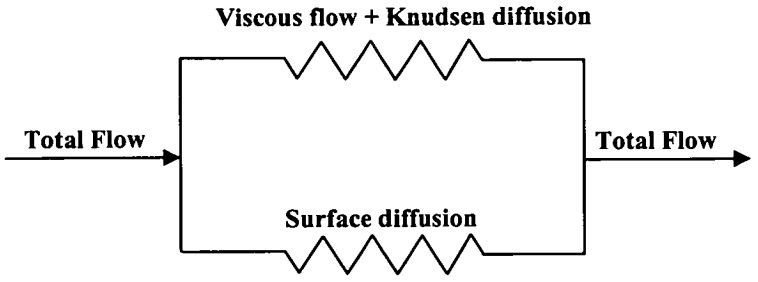

Figure 3.20 – Electric analogue circuit representing the flow of the diffusion species. Adapted from Wesselingh & Krishna (1997).

The relative importance between the viscous flow and the Knudsen diffusion (and therefore the properties of flux in porous media) depends on the ratio between the frequency of molecule-molecule collisions and molecule-wall collisions. The Knudsen number, K_n, is normally used to classify these different diffusion regimes:

$$K_n = \frac{\lambda}{w} \tag{3.32}$$

where w is the pore width and λ is the mean free path (defined as the average distances that a molecules travels between two consecutive collisions). For a pure gas (Hecht 1990),

$$\lambda = \frac{K_b T}{\sqrt{2}\,\pi\sigma^2 P} \tag{3.33}$$

K_b is the Boltzmann constant, T is the temperature, P is the pressure and σ is the molecular diameter. The mean free path of species 1 in a gas mixture is given by (Hecht, 1990):

$$\lambda_1 = \frac{\bar{c}_1}{z_1} \tag{3.34}$$

$\bar{c}_1$ is the average molecular speed of molecule 1 at temperature T, and z_1 is the total number of collisions per second between molecules of species 1 and all other molecules:

$$z_1 = \sum_{j=1}^{n} \rho_j \sigma_{1j}^2 \left(\frac{8 \pi R T}{\mu} \right)^{1/2} \tag{3.35}$$

where ρ_j is the number density of species j, σ_{1j} is the arithmetic average molecular diameter ($\sigma_{1j} = \frac{\sigma_1 + \sigma_j}{2}$) and μ is the reduced mass ($\mu = \frac{M_1 M_j}{M_1 + M_j}$).

Depending on the magnitude of the Knudsen number three main flow regimes can be identified:

1. $K_n \ll 1$ Molecular diffusion and viscous flow (in the presence of a pressure gradient) are the main transport mechanisms. Here molecule-molecule interactions are dominant and the velocity of the molecules near the wall is zero.
2. $K_n \approx 1$ This is the transition region. Slip flow may occur (Levenspiel, 1994) because the velocity of the molecules near the wall is not zero (*i.e.* it is not negligible compared to the overall velocity).
3. $K_n \gg 1$ Knudsen diffusion induced by the collision of molecules on the wall occurs. Here, there are very few collisions between gas molecules. Thus, the concept of viscosity has no meaning and is no longer applicable.

However, this simple picture is likely to breakdown in the presence of an adsorbed phase because the micropore size has the same order of magnitude as the diameter of the adsorbed molecules and molecules never leave the influence of the force field of the pore wall (Karimi & Farooq, 2000). Thus, the molecular trajectories in adsorbed phases (as in a condensed liquid-like phase) are much shorter than predicted by

Equation 3.33 and Equation 3.34 from the kinetic theory (for gas phases). The mean free path in liquid-like phases is only a few Angstroms (Cussler, 1997) and the Knudsen number is always small (see Table 3.1). The mean free path in a liquid phase (shown in Table 3.1) is a rough estimate of the mean free path in the adsorbed phase, assuming that the liquid density is about three orders of magnitude smaller than for gases.

Table 3.1 - Values of the mean free path and Knudsen number calculated from Equations 3.32 –3.35. (Temperature 300 K and for a pore width of 20 Å).

Partial	Hydrogen				Methane			
pressure	pure		mixture		pure		mixture	
(bar)	λ (Å)	K_n	λ (Å)	K_n	λ (Å)	K_n	λ (Å)	K_n
1	2174.5	108.7	1091.0	54.6	1284.3	64.2	483.8	24.2
10	217.5	10.9	109.1	5.5	128.4	6.4	48.4	2.4
Liquids	2.2	1.1	1.1	0.6	1.2	0.6	0.5	2

For the system studied (a mixture of 80% hydrogen / 20% methane at 300 K and 18.25 bar), the mean free path is about 60 Å for hydrogen and 23 Å for methane. The corresponding values of K_n are 2 and 1 for hydrogen and methane respectively on a pore width of 20 Å. Thus, in this work we may find a combination between Knudsen diffusion and slip flow on the surface. To investigate, and quantify, the contribution of different diffusion mechanisms, the pore was divided into two regions according to their local densities:

i) the wall region characterised by transport diffusion in the dense and less mobile adsorbed layers on the surface (*i.e.* diffusion on the surface or liquid-like diffusion);

ii) the middle pore region characterised by molecular and Knudsen diffusion. In this region, the density is smaller relatively to the density near the wall but the molecules are more mobile because they do not have a compact density.

A schematic representation of the simulated pore used in this work is shown in Figure 3.21. The diffusion on the surface occurs in two adsorbed layers of thickness t. In Figure 3.21, w is the simulated pore width (*i.e.* the distance between carbon centres of each wall) and w_0 is the smallest pore in which diffusion takes place. Thus, ½ w_0 represents the minimal distance that a molecule can approach the surface (this value is established by the solid-fluid potential).

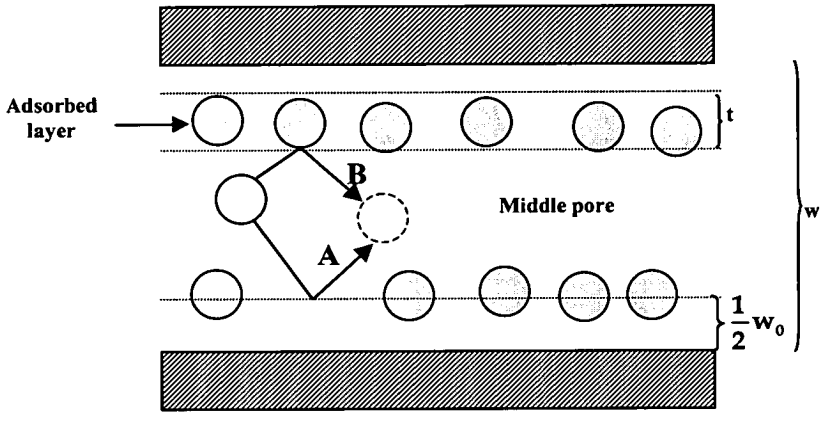

Figure 3.21 – Illustration of the simulated pore of width w, showing two adsorbed layers at surface each having a thickness t and the centre-to-centre minimal distance ($½\, w_0$) between the fluid molecules and the carbon atoms of the surface wall.

To determine the diffusion coefficients in each transport region, we calculate the fluxes and density profiles in each of these regions, and we apply Equation 3.21 independently to each region. The value of t and w_0 were determined *a priori* from the cross-section density profiles shown in Figure 2.18.

3.3.1 Middle Region Diffusion and Wall Region Diffusion

Knudsen transport is due to the collision of gas molecules with the pore wall (*i.e.* collision between gas molecules and the internal surface wall of a pore are more frequent than the collision between gas molecules). The resulting movements of

different molecules are independent of each other (Mason & Malinauskas, 1983). The Knudsen diffusive flux, J_i^K, equation can be written as:

$$J_i^K = \frac{1}{4}\omega\,\bar{c}_i\,\Delta\rho_i \tag{3.36}$$

where $\Delta\rho_i$ is the bulk density difference along the length of the pore, $\bar{c}_i$ is the mean thermal molecular speed and ω is a probability factor that depends on the capillary geometry. Clausing (1931, 1971) looked at the problem of molecular flow through a capillary aperture with rectangular section. An analytical solution can only be found if the length of the capillary aperture is much larger than the capillary width and capillary length. For example for a long straight rectangular capillaries (*i.e.* $L_x \gg w$) we have:

$$\omega = \frac{w}{L_x}\ln\left(\frac{L_x}{w}\right) \tag{3.37}$$

A slit-like pore can be thought of as a very large rectangular capillary aperture (*i.e.* where the contribution of the side walls are insignificant). Figure 3.22 shows the probability factor function for different capillaries geometries (probability are taken from Clausing, 1971). Our pore length (L_x) is about 40.5 Å.

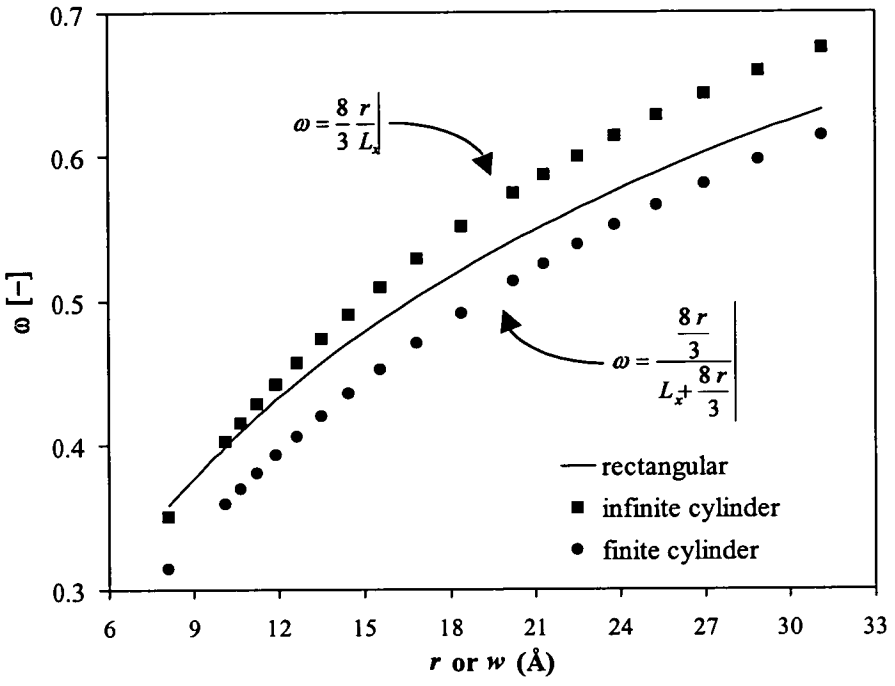

Figure 3.22 – Probability ω as function of slit width (w) or capillary radius (r). Adapted from Clausing (1931, 1971).

From Figure 3.22, we can see that the probability factor for a rectangular capillary lies between the solution for infinite cylindrical capillaries and finite cylindrical capillaries. Since there is not any simple analytical relation to express the probability factor of a rectangular capillary as function of the pore width we approximate ω (without significant lost of precision) to the probability factor for infinite cylindrical capillary:

$$\omega = \frac{8\,w}{3\,L_x} \tag{3.38}$$

By comparing the Knudsen flux equation (see Equation 3.36) with the Knudsen flux expressed in a Fickian form (see Equation 3.22) one gets:

$$J_i^K = \left(\frac{2\,w}{3}\right)\bar{c}_i\,\frac{\Delta\rho_i}{L_x} = -D_i^K\,\frac{d\,\rho_i}{d\,x} \tag{3.39}$$

where $\bar{c} = \sqrt{\frac{8RT}{\pi M_i}}$. Thus, the Knudsen diffusion coefficient in a slit pore can be given by:

$$D_i^K = \frac{2}{3}(w - w_0)\sqrt{\frac{8RT}{\pi M_i}} \tag{3.40}$$

w_0 is the smallest pore in which diffusion takes place. Hence, the term $(w - w_0)$ in Equation 3.40 represents the effective pore width and discounts the distance to the wall, in which molecules cannot get closer (see Figure 3.21). In our simulations, it was found that w_0 is about 4.6 Å for hydrogen and 5.7 Å for methane.

Figure 3.23 shows the diffusion on the surface, middle pore region diffusion and Knudsen diffusion from theory for pure-hydrogen. There is good agreement between middle pore region diffusion and the diffusion calculated from Equation 3.40 at both temperatures analysed (300 K and 500 K). Thus, we conclude that Knudsen diffusion is the dominant mechanism in the central part of the pore.

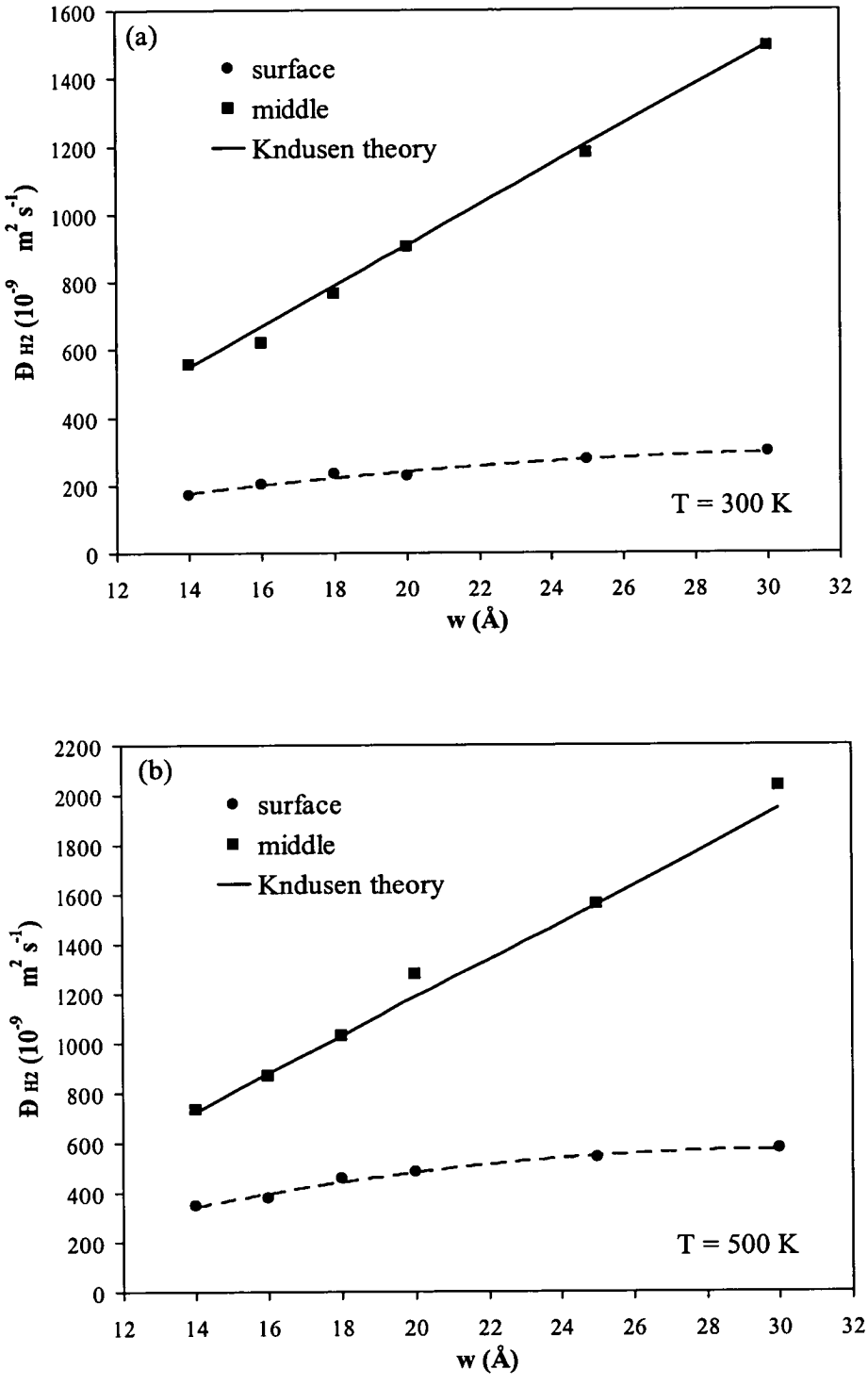

Figure 3.23 – Pure-hydrogen surface (circles), middle pore diffusion (squares) and Knudsen diffusion from theory (lines) at (a) low temperature and (b) high temperature. Dashed line is a guide to the eye.

Figure 3.24 shows the surface diffusion, middle-pore diffusion and Knudsen diffusion from theory for pure-methane. However, only a qualitative agreement can be seen between the middle pore diffusion and the diffusion calculated from Equation 3.40. Diffusion coefficients near the surface wall are about one order of magnitude smaller than the diffusion coefficients in the middle region.

To explain the qualitative agreement, shown in Figure 3.24, between middle pore diffusion and the Knudsen diffusion calculated from Equation 3.40 we need to look back to Figure 3.21. There, we can see that a fluid molecule can collide either with the pore surface (trajectory **A**) or with the molecules that form the adsorbed layer (trajectory **B**). Thus, the probability of a fluid molecule colliding with adsorbed layer is proportional to the surface coverage. The "total" Knudsen diffusion coefficient (D^{Kp}) is:

$$D^{Kp} = (1-\theta)D^{K}\Big|_{A} + (1-\theta)D^{K}\Big|_{B} \tag{3.41}$$

Using the variables defined in Figure 3.21, Knudsen equation 3.41 reduces to:

$$D^{Kp} = \frac{2}{3}(w - w_0 - 2\,t\,\theta)\,\bar{c} \tag{3.42}$$

where θ is the surface coverage and $\bar{c}$ is the mean molecular speed. The methane monolayer thickness (t) can be estimated from Figure 2.18. The relative importance of the adsorbed layer to the Knudsen diffusion, is obtained by comparing Equation 3.40 and Equation 3.42:

$$\frac{D^{Kp}}{D^{K}} = 1 - \frac{2\,t\,\theta}{w - w_0} \tag{3.43}$$

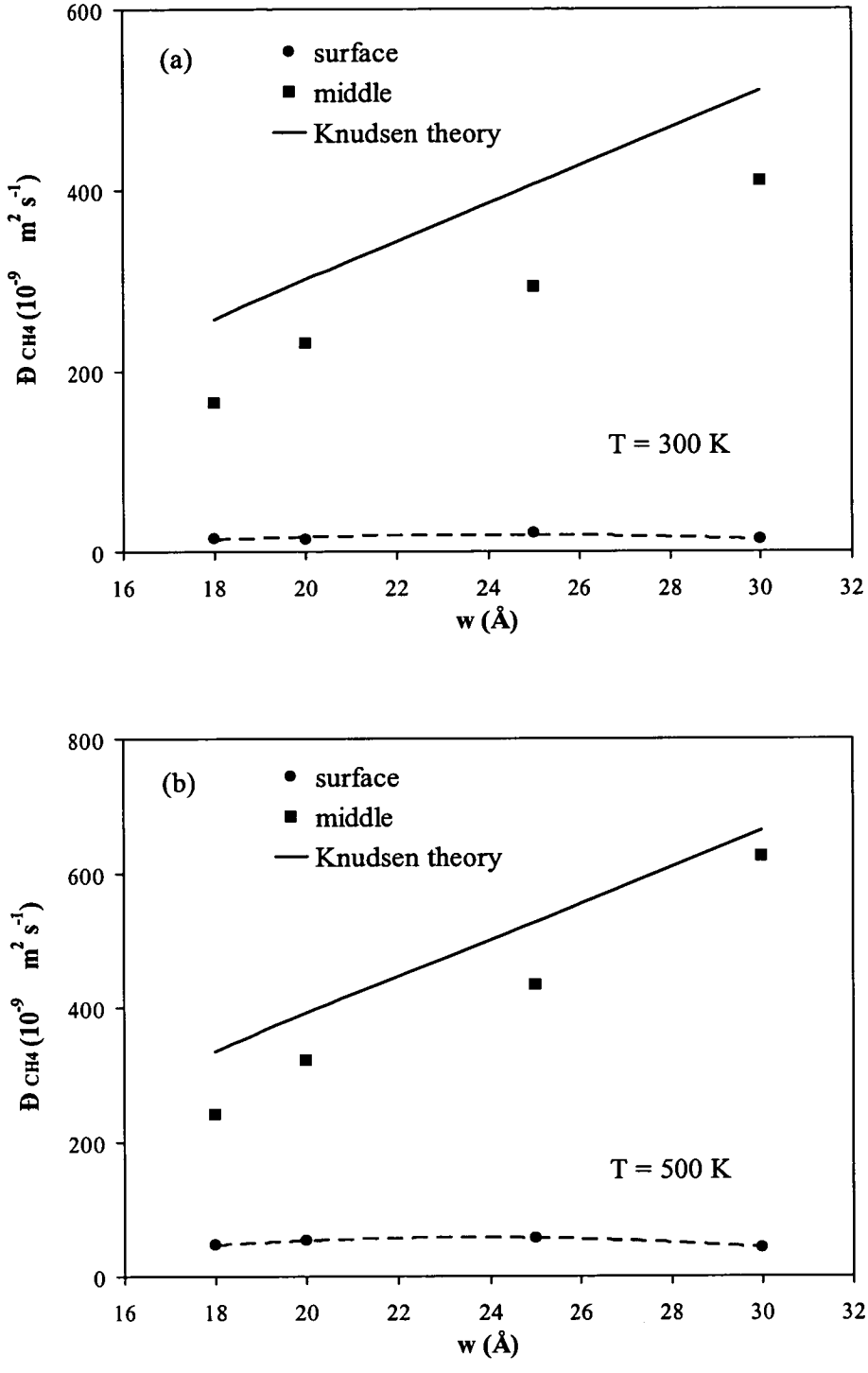

Figure 3.24 – Pure methane surface (circles), middle pore diffusion (squares) and Knudsen diffusion from theory at (a) low temperature and (b) high temperature. Dashed line is a guide to the eye.

Equation 3.43 shows why it is not possible to observe a good agreement between Knudsen diffusivities obtained from the simulations and those from Equation 3.40. It can be seen in Equation 3.43 that when the surface coverage increases, the difference between Knudsen diffusion at zero-coverage and Knudsen diffusion in the presence of adsorption increases. By assuming a constant monolayer of 3 Å and coverage of 50 %, one gets, according to Equation 3.43 a value of $\frac{D^{Kp}}{D^{K}}$ between 0.6 and 0.8 (we note that this range is in conformity with the deviation observed in Figure 3.24).

Figure 3.25 shows that the logarithm of diffusivities in the wall region is proportional to inverse of absolute temperature as for activated diffusion (see Equation 3.31):

$$\ln\left(D^{S_0}\right) = \ln\left(D^{S_\infty}\right) - \frac{E_a}{R\,T} \tag{3.44}$$

Thus, the temperature dependence of the diffusivities in the wall region suggests that transport in this region occurs by diffusion on the surface. The methane activation energy is about double the hydrogen activation energy ($E_a(H_2)$ = 4.1 kJ mol^{-1} and $E_a(CH_4)$ = 8.5 kJ mol^{-1}). Therefore, methane surface diffusivities vary more with temperature than hydrogen surface diffusivities (the activation energy is calculated from the slope of the Equation 3.44).

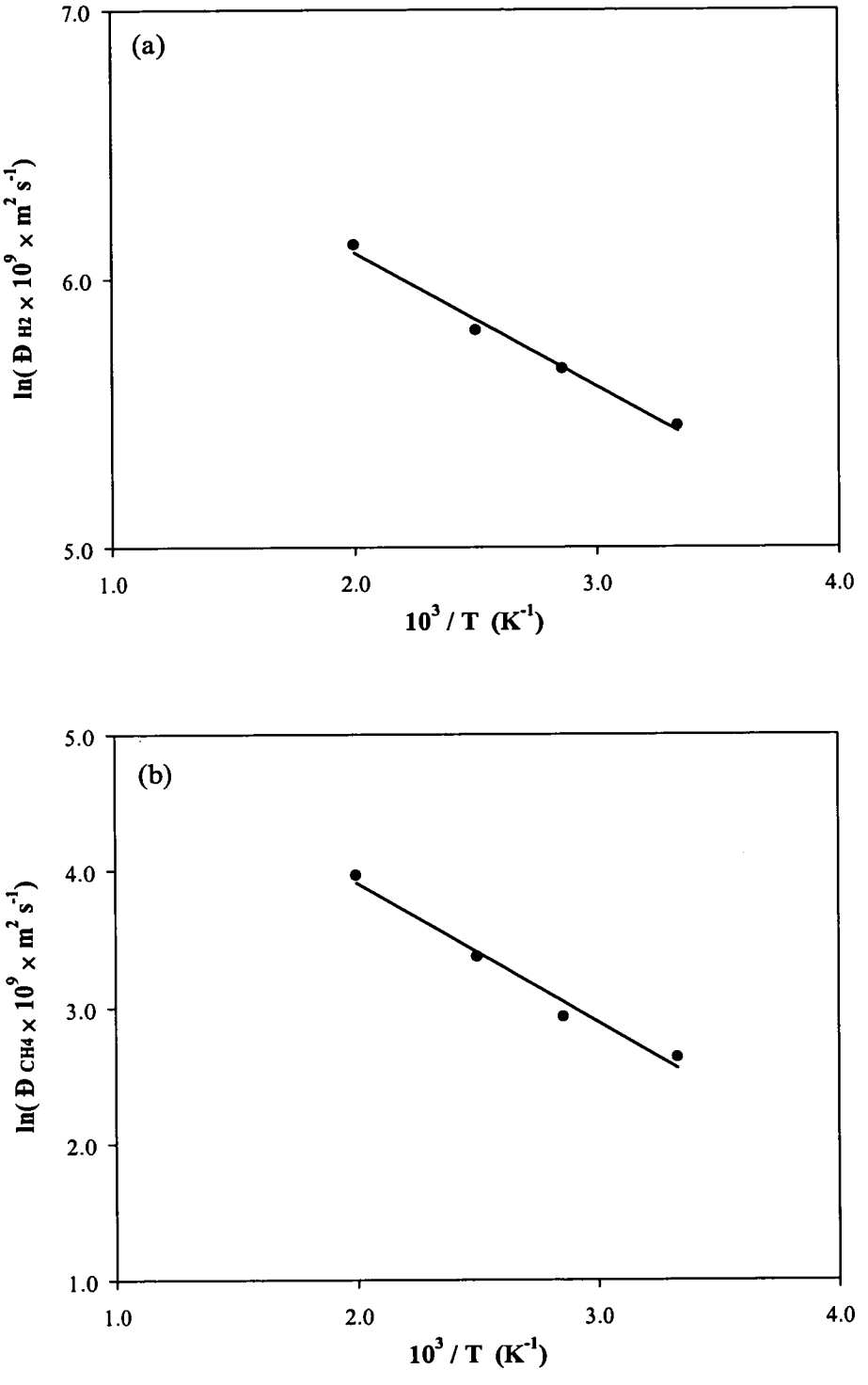

Figure 3.25 –Temperature dependence of the diffusion coefficients in the wall region for: a) pure hydrogen (14.6 bar) and b) pure methane (3.65 bar). The pore width is 20 Å.

3.3.2 Total Diffusivities

The middle-pore flow and adsorbed phase flow on the wall occur in parallel (by analogy to an electrical circuit) and are to a first approximation independent (Do, 1998; Kärger & Ruthven, 1992; Wesselingh & Krishna, 2000) and are consequently additive. The contribution of the adsorbed phase flow on the wall to the total flow may be quite significant particularly in micropores. The relative importance of diffusion on the surface relatively to other diffusion mechanisms is proportional to the adsorbate density (Kärger & Ruthven, 1992):

$$D = D^p + \mathcal{K}\, D^s \tag{3.45}$$

where $\mathcal{K}$ is the dimensionless adsorption equilibrium constant (*i.e.* the adsorbed density divided by the bulk phase density), D^s is the surface diffusion, D^p denotes the contributions from Knudsen and molecular diffusion and D is the total diffusion coefficient.

Recently, Wesselingh & Krishna (2000) expressed the microporous total diffusivity in terms of both the fraction of molecules adsorbed and on the magnitude of the surface (D^S) and Knudsen diffusivities (D^K):

$$D = \frac{\rho^S}{\rho^S + \rho^K} D^S + \frac{\rho^K}{\rho^S + \rho^K} D^K \tag{3.46}$$

where ρ^S is the adsorbed density on the first adsorbed layer and ρ^K is the density in the middle of the pore.

If we assume that the two mechanisms (Knudsen and diffusion on the surface) occur independently (as shown schematically in Figure 3.20 and Figure 3.21) then the flows (F) in each region are additive (by analogy with a system of two resistances in parallel in an electrical circuit):

$$A D_i \frac{d\rho_i}{dx} = A_s D_i^s \frac{d\rho_i^s}{dx} + A_K D_i^K \frac{d\rho_i^K}{dx} \tag{3.47}$$

By approximating the derivatives by finite differences and knowing that the product side density is zero one gets:

$$D_i \frac{\Delta(A\,\rho_i)}{L_x} = D_i^s \frac{\Delta(A_s\,\rho_i^s)}{L_x} + D_i^K \frac{\Delta(A_K\,\rho_i^K)}{L_x} \tag{3.48}$$

Thus, we obtain the following total diffusivity equation:

$$D_i = \frac{n_i^s}{n_i} D_i^s + \frac{n_i^k}{n_i} D_i^K \tag{3.49}$$

Thus, the total diffusion depends not only on the diffusion coefficients (D_i^s and D_i^K) but also on the fraction of molecules in the wall region and in the fraction of molecules at the middle of the pore.

Figure 3.26 shows the variation of the number fraction of molecules in the region near the wall and in the middle of the pore in a simulation run at 300 K. There we can see that the methane molecules are mainly located on the surface (only about 10 % of the methane molecules are located in the central region of the pore). Thus, the methane flow is mainly on the surface of the pore. On the other hand, the hydrogen molecules are also mainly located near the wall (because the volume defined near the wall is larger than the volume in the middle of the pore) but the fraction of hydrogen molecules located on the surface decreases as the middle pore volume increases. A similar conclusion was drawn from the equilibrium snapshots shown in Figure 3.3.

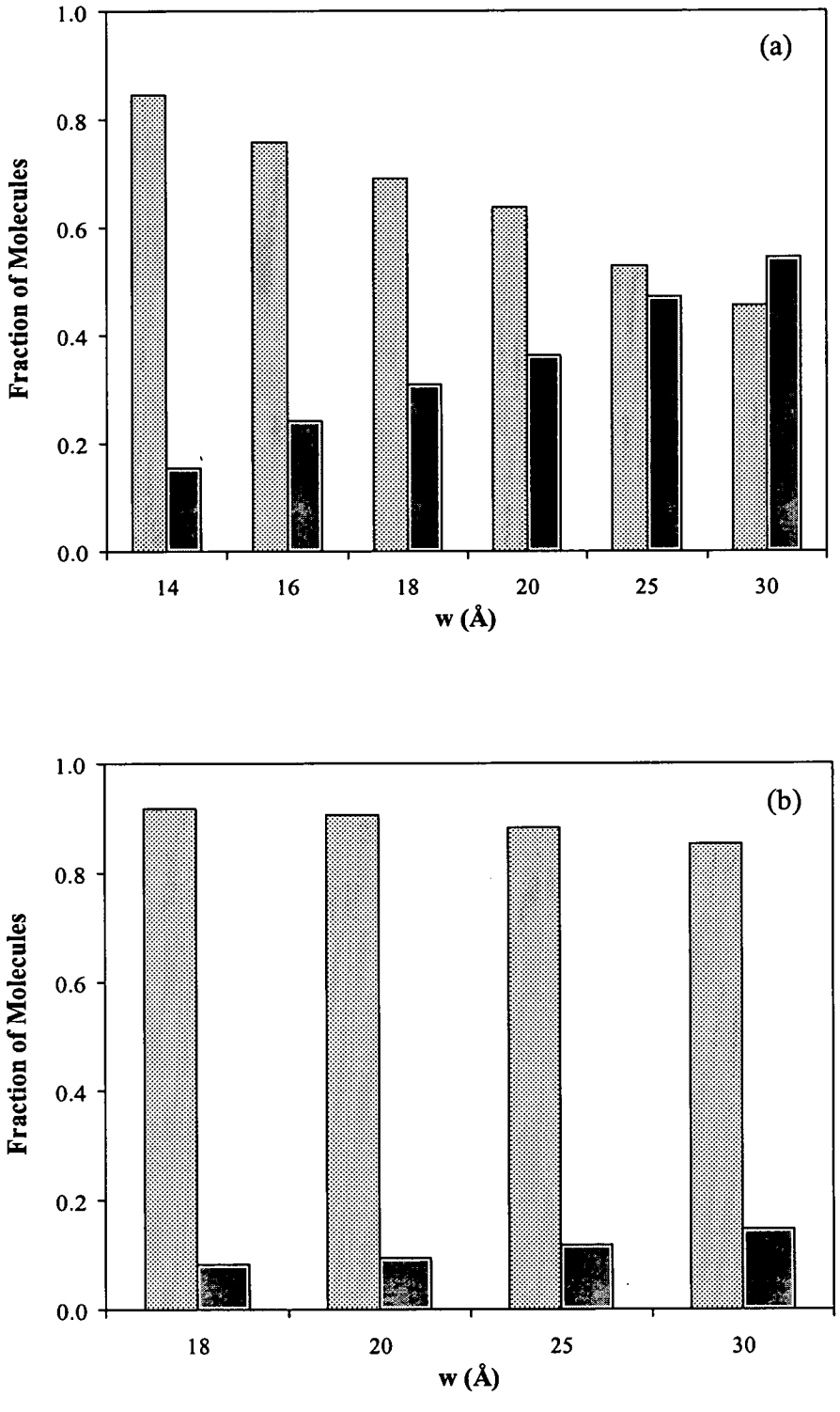

Figure 3.26 - Fraction of number of molecules in wall region (dashed light grey) and mid pore region (dark grey) for a) pure hydrogen and b) pure methane at 300 K. Hydrogen pressure is 11.6 bar and methane pressure is 3.65 bar.

In Figure 3.27, we compare the total pore diffusivities obtained from the surface diffusivities and Knudsen diffusivities (Equation 3.49) with the diffusivities measured directly from our simulations (simulated diffusivities are on the x-axis while estimated diffusivities are on the y-axis). The method proposed by Kärger & Ruthven (1992), described by Equation 3.45, underestimates the total diffusivities. On the other hand, Wesselingh & Krishna (2000), described by Equation 3.46, overestimates the total diffusivities because they have assumed that the surface and Knudsen flow area are the same. The total diffusivity that is proposed in this work (Equation 3.49) gives an excellent agreement with the total diffusivity calculated directly from our simulations. This emphasises the realism and the physical basis of Equation 3.49.

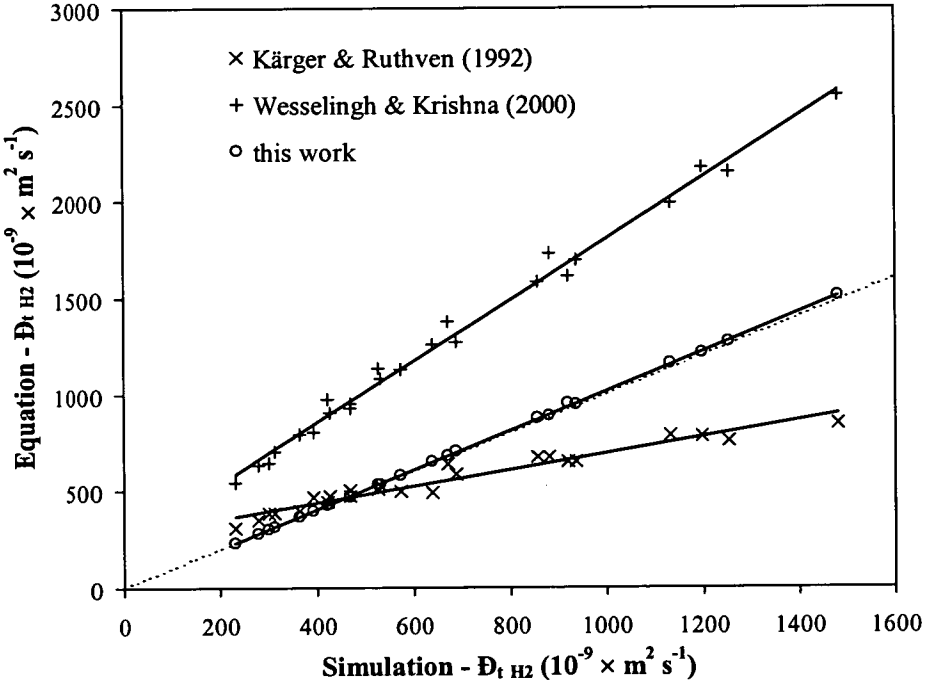

Figure 3.27 – Comparison of different total diffusivity methods for pure hydrogen in pores between 14 and 30 Å and temperatures between 300 K and 500 K. Dashed line represents a slope of unity.

3.4 Summary

The Generalised Maxwell-Stefan (GMS) diffusion equations of Krishna (1990) are used to calculate diffusion coefficients. GMS uses microscopic information about intermolecular friction between different species. To obtain the diffusion coefficients we fit our simulation results to the GMS equations. Cross-diffusion coefficients and viscous flow are found to be negligible. Maxwell-Stefan diffusion coefficients are also found to be composition independent providing evidence that supports the applicability of GMS equations to describe mass transport in our micropore range.

Our simulation results have identified two pore size ranges in which different transport mechanisms are dominant:

i) In pores smaller than about 10 - 12 Å, strong methane adsorption occurs in the pores, blocking hydrogen molecules from adsorbing and diffusion into the pore. High selectivities are observed. Both hydrogen fluxes and permeabilities are strongly affected by the presence of methane (because methane adsorbed more strongly in the pore, thereby excluding the hydrogen molecules). However, the methane properties (adsorbed densities and diffusivities) are not affected significantly by the presence of hydrogen in the mixture.

ii) In pores bigger than about 14 Å, the void space between walls increases allowing hydrogen molecules to enter more easily. This results in a decrease in selectivities. In this region, both fluxes and hydrogen permeabilities are proportional to the pore size denoting Knudsen-like diffusion. However, methane fluxes appear to be independent of pore size.

We also observe that the equilibrium selectivities are smaller than the kinetic selectivities because the species have different mean velocities. An inverse temperature dependence is observed on the fluxes and permeabilities for both

species. In pores bigger than about 14 Å, the diffusion coefficients increase with temperature and pore size denoting Knudsen behaviour.

To investigate, and quantify, the contribution of different diffusion mechanisms, the pore was divided into two regions:

i) the wall region characterised by transport diffusion in the dense and less mobile adsorbed layers on the surface;

ii) the middle pore region characterised by molecular and Knudsen diffusion. In this region, the density is smaller relatively to the density near the wall but the molecules are consequently more mobile.

This enabled us to determine that flow in the middle region of the pore follows the Knudsen theory (via Equation 3.40) while the flow in the wall region is on the surface (see Equation 3.31). Good agreement was found between the hydrogen middle pore diffusion and the diffusion coefficient obtained from the Knudsen theory (Clausing, 1931; 1971). Not such good agreement was observed with methane because middle pore methane molecules are colliding more frequently with the methane adsorbed layer than with surface of the pore. Thus, the observed methane Knudsen diffusion coefficient is less than the one predicted from the Knudsen theory. Methane molecules are mainly located at the pore surface while hydrogen molecules are more equally distributed in the pore. The total diffusion coefficient was found to depend on the number fraction of molecules in each transport region.

4. Non-Equilibrium Molecular Dynamics Simulation of Gas Separation in a Microporous Carbon Membrane

In the previous chapter, simulation of adsorption and diffusion in micropores in general was addressed. Molecular simulations of gas separation of the SSF membrane described in Chapter 1 are reported in this chapter. Here, we compare Air Products experimental results with our simulation results in order to estimate the pore size that best describes the experimental results for a mixture of 50 % hydrogen/ 50 % methane. A new set of DCV-GCMD simulations were conducted and are reported in this Chapter. The experimental Air Products membrane set-up is described in Appendix I. The studied operating conditions are 295.1 K of temperature and three different pressures (11.3 bar, 32.0 bar and 55.6 bar).

4.1 SSF Adsorption Simulation Results

The variation of the equilibrium density as a function of pore width, *w*, obtained by GCMC simulation, is shown in Figure 4.1. [*w* is defined as the distance between the centres of the carbon atoms on opposing pore walls.] Here, it can be seen that hydrogen can enter into pores as small as 4.9 Å while methane is restricted to pores larger than 5.9 Å. The adsorption of methane and hydrogen oscillates as a function of pore size, in pores between 5.9 Å and about 12 Å, reflecting the packing of the methane molecules and the corresponding variation in the space available to hydrogen; adsorption of methane is favoured when one or two distinct layers of methane molecules fit into the pore - at about 7 and 12 Å respectively, with more space available for hydrogen between these peaks. [This feature is, in effect, an artefact of the regular pore model used, and would not be observed in a real membrane with a more heterogeneous pore structure.] At still larger pore sizes, the

methane adsorption is weaker allowing a gradual increase in the amount of hydrogen adsorbed. The effect of pressure is to increase adsorption of both species, especially at larger pore sizes where the pore is not already close to saturation.

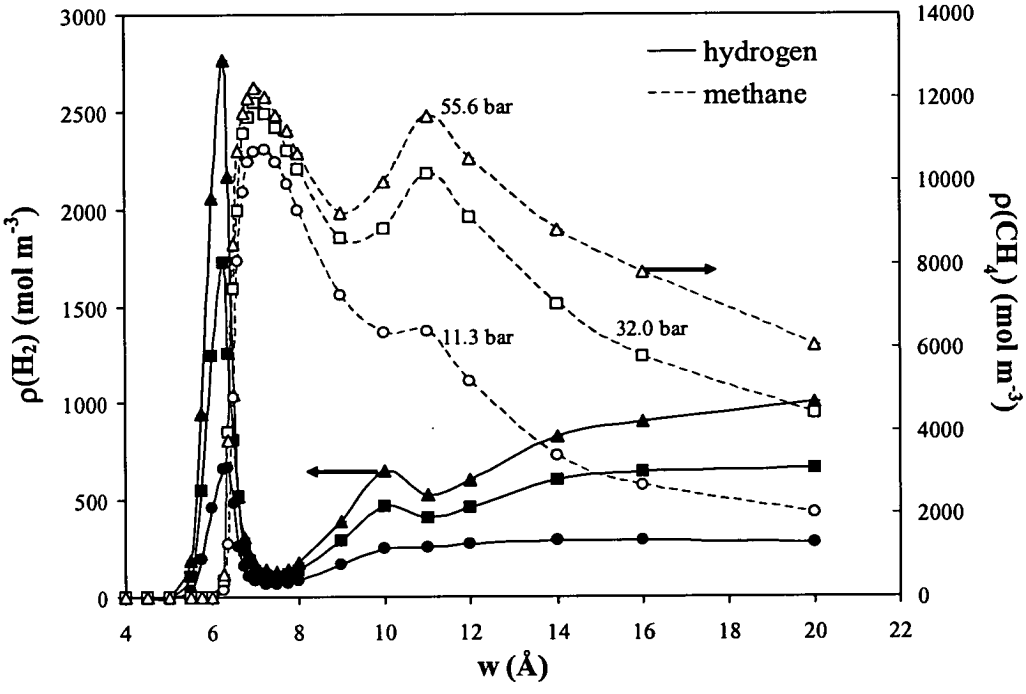

Figure 4.1 - Variation of absolute density with pore with at 295.1 K for a mixture of 50 % hydrogen/ 50 % methane, with feed pressure as a parameter. Solid lines and filled symbols represent hydrogen and dashed lines and open symbols represent methane.

Figure 4.2 shows the variation of the equilibrium selectivity of methane over hydrogen as function of pore width. A maximum of selectivity at about 7 Å is observed. However, an increase in pressure causes a drastic selectivity reduction in pores smaller than 10 - 12 Å. In those small pores, increasing the pressure can squeeze hydrogen more easily into vacancies between the methane molecules. In large pores the equilibrium selectivity is, over this pressure range, independent of pressure because the adsorption isotherms become linear in pores bigger than 12 Å and the selectivity depends only of the ratio of the Henry's constants (see Equation 3.6).

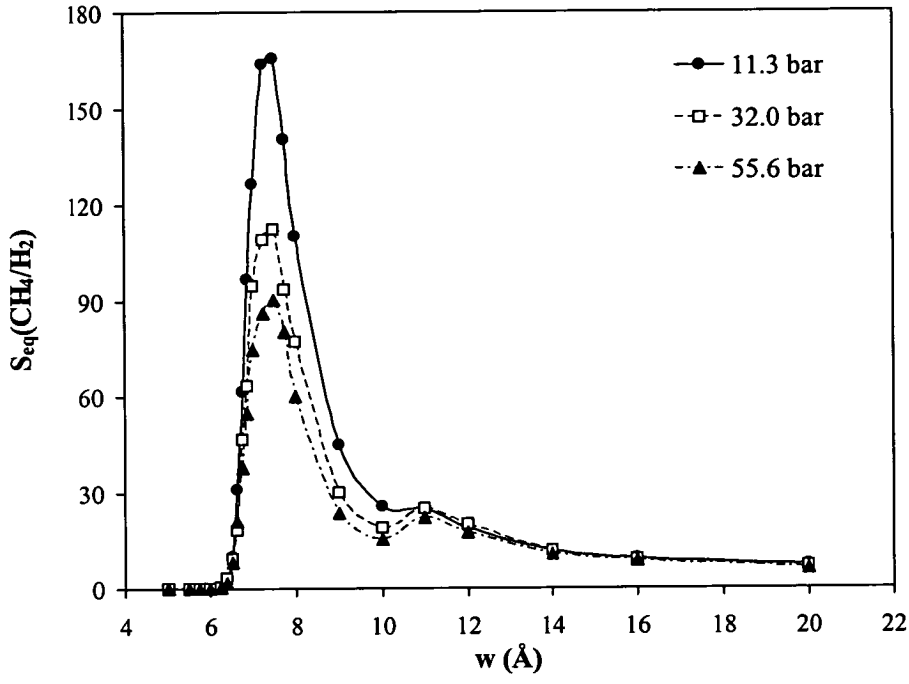

Figure 4.2 - Variation of equilibrium selectivity with pore width at 295.1 K for a mixture of 50 % hydrogen/ 50 % methane, with feed pressure as a parameter.

Equilibrium separation can be more easily understood by referring to snapshots of molecular configurations (Figure 4.3), where the effect of pore size on adsorption is better visualised. Methane molecules are too big to enter in the pore of 6.0 Å. Thus, separation is based on molecular size as in a molecular sieve for small pore sizes (*i.e.* the small hydrogen molecules enter preferentially). The maximum selectivity is observed at 7.0 Å (see Figure 4.2), which is the pore width where the methane molecules are most effectively packed in a single layer, with the efficient packing leaving little space for hydrogen molecules. As the pore size increases, the void space between the walls increases allowing the hydrogen molecules to enter the pore more freely. This effect starts to become more pronounced at around 9.0 Å, where the pore is not quite large enough to accommodate two methane layers; this corresponds to the minimum methane density. At 20.0 Å, the methane is mainly located on the surface while hydrogen is restricted to the low-density section in the centre of the pore.

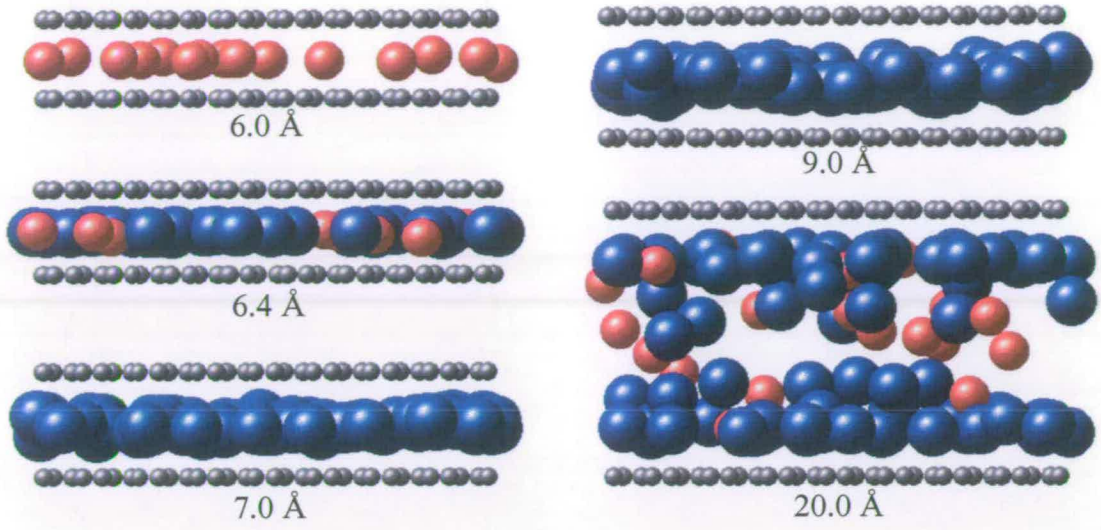

Figure 4.3 - Equilibrium simulation snapshots at 55.6 bar and 295 K (50 % hydrogen / 50 % methane mixture). Methane is represented by blue spheres and hydrogen by red spheres. (Note that the black carbon atoms are reduced in size to make picture clearer.)

4.2 SSF Transport Simulation Results

Transport permeabilities for the hydrogen/methane mixture as a function of pore width are shown in Figure 4.4. Pores smaller that about 6 Å behave like molecular sieves (*i.e.* hydrogen molecules can pass through the pores while methane cannot enter). The hydrogen permeability increases with increasing pore size and with decreasing feed pressure. This reflects the higher methane loading at high pressure (shown in Figure 4.3) which hinders the diffusion of hydrogen. In addition, the hydrogen permeabilities depend linearly on the pore size, in pores larger than 11 Å - 12 Å. As we have seen in Section 3.3, hydrogen diffusion has a Knudsen-like behaviour (but with collisions with the adsorbed films of mostly methane, rather than the pore walls) and both the hydrogen flux and the permeability (via Equation 3.23) show a corresponding linear dependence on the pore size. On the other hand, methane shows a rapid and significant increase of the permeability in small pores. In this pore size range, the methane density is high (7 - 8 Å corresponds to the

maximum equilibrium selectivity as shown in Figure 4.2) but the molecules are tightly packed and therefore less mobile. A maximum in the methane permeability is observed at about 9 Å because the adsorbed layer is dense and also relatively mobile. In pores slightly larger than 9 Å, the molecules pack less effectively (as shown in Figure 4.3), so the adsorbate density is lower, leading to a lower permeability. Increasing pressure causes a general increase in the permeability of both components (though to an extent that differs between the components and varies with pore size), due to the increase in adsorbate loading with pore size.

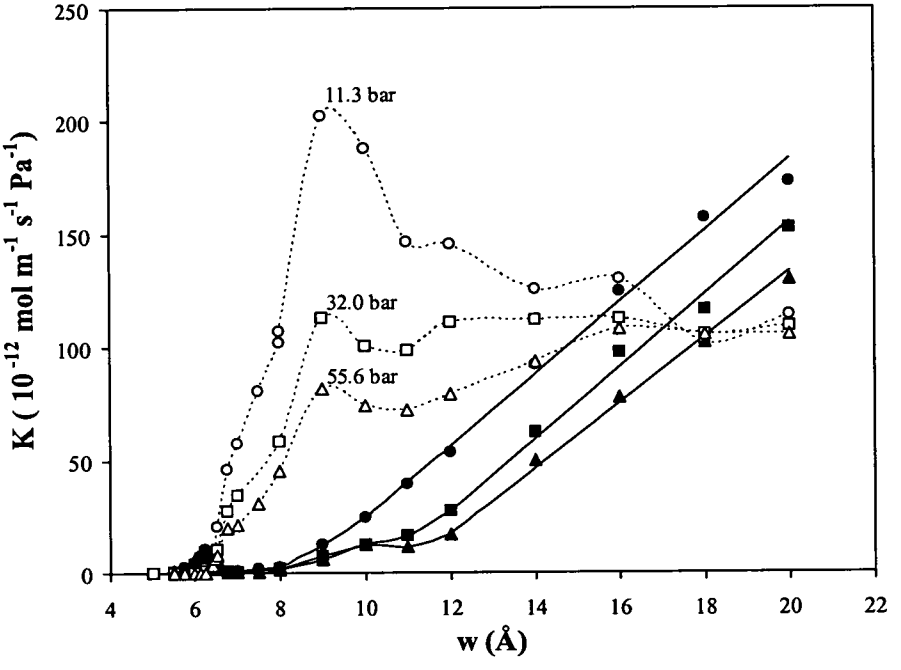

Figure 4.4 – Simulated gas permeabilities for a 50 % hydrogen/ 50 % methane feed mixture as function of pore width at 295 K, with feed pressure as a parameter. Solid lines and filled symbols represent hydrogen and dashed lines and open symbols represent methane.

Figure 4.5 shows the variation of the simulated kinetic selectivity with pore width. There is a maximum in the kinetic selectivity as a function of the pore size (between 6.5 and 7.5 Å) because the pores are already substantially full of methane. The separation selectivity decreases considerably with the increase in the volume available for hydrogen diffusion (*i.e.* with the pore size). In effect, high selectivities

arise from the exclusion of hydrogen from the pore by the adsorption of methane. On the other hand, pores of about 6 Å are filled exclusively by hydrogen due to molecular size restrictions (*i.e.* methane molecules are too big to enter in pores smaller than about 6.3 Å).

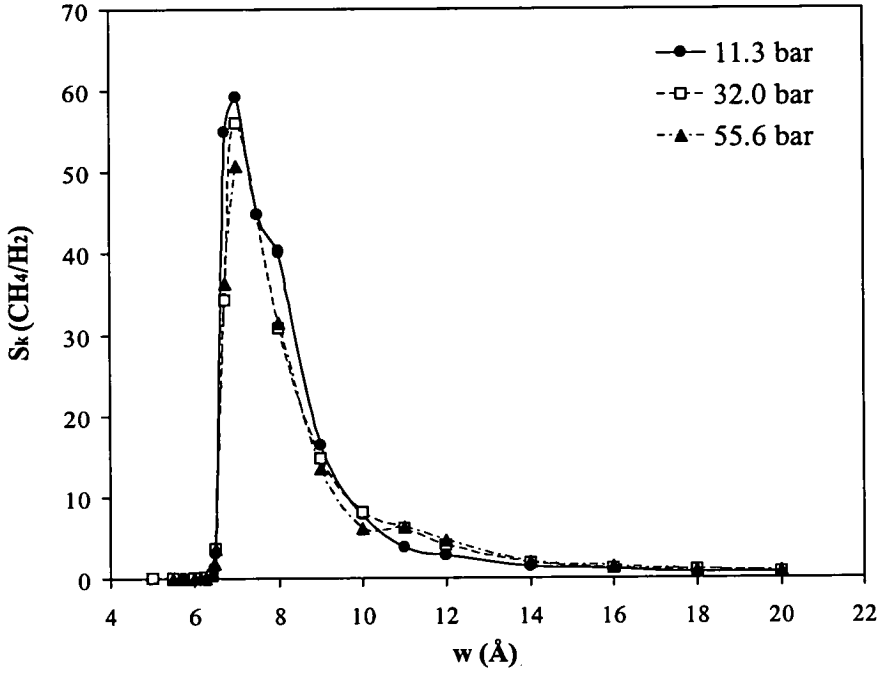

Figure 4.5 – Simulated gas selectivities in a 50 % hydrogen/ 50 % methane feed mixture as function of pore width at 295 K, with feed pressure as a parameter

4.3 Determination of Pore Size of the SSF Membrane

Pore sizes in which the simulated permeability and selectivities bound the experimental results define the SSF carbon membrane pore size range (*i.e.* provides a good agreement with experimental data). Our pores are represented by an array of identical and non-intersecting pores. Figure 4.6 shows a detail of the simulated selectivities and experimental selectivities (shown in Figure 1.4). Here it is clear that there is only one pore size region, between 6.4 to 6.5 Å, where the simulated selectivity matches the experimental values at all three pressures (the selectivity

curves for the three pressures overlap each other in this region). The Air Products experimental results (reported previously in Chapter 1) showed that increasing the pressure causes a decrease in the separation selectivity. Similarly, we observe that the permeabilities and the kinetic selectivity decreases with increasing pressure in pores of around 6 to 7 Å (because more hydrogen is forced into the pores at high pressure, while the methane loading hardly changes as the pores are already substantially full of methane). Additionally, small changes in the pore width, at this pore range, cause big variations in the separation selectivities. This explains the significant variation in the pure-component selectivities between different batches of the same membrane material described in Chapter 1. On the other hand, such good agreement with the experiment in pores larger than 12 Å is not observed (for example, the simulated selectivity at 55.6 bar intersects the experimental selectivity only in pores larger than 20 Å). Thus, according to these simulation results, the SSF experimental pore size is expected to be between 6.4 to 6.5 Å.

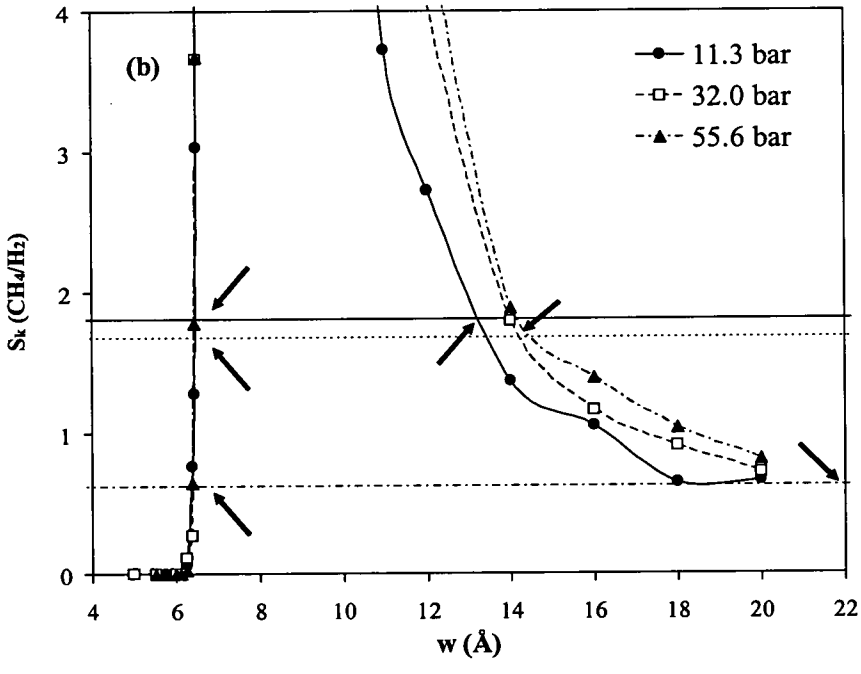

Figure 4.6 – A detail of the simulated gas selectivities in a 50 % hydrogen/ 50 % methane feed mixture as function of pore width at 295 K, with feed pressure as a parameter. Horizontal lines represent experimental SSF selectivities, and the arrows point to pore sizes at which the simulated and experimental data agree.

In Chapter 1, we have seen that the porous structure in the SSF membrane is formed during thermal treatment in an atmosphere of inert gas, due to small gas molecules channelling their way out of the solid during the latex pyrolysis (Rao & Sircar, 1993b; Rao, Sircar & Golden, 1992). According to Soffer, Koresh & Saggy (1987), the pore size of a carbon membrane can be further optimised, for a particular separation, by carefully controlling the oxidation at an elevated temperature. The experimental permeability shows a maximum as a function of the degree of oxidation (Rao, Sircar & Golden, 1995), and by implication as a function of pore width, behaviour which is also observed in the simulations (see Figure 4.5). It thus appears that the maximum in the experimental methane/hydrogen selectivity at about 1.5 hours, shown in Figure 1.5, corresponds to a pore width between 6.5 Å and 7.5 Å in our simulations. Therefore, the original unoxidised pore size on the SSF membranes reported in references (Rao & Sircar, 1993b, 1996; Rao, Sircar & Golden, 1995) must be smaller than about 7 Å. Moreover, the experimental pore width cannot be higher than 12 Å, contrary to the suggestion of Seo, Kum & Seaton (2002a, 2002b), based on less realistic dynamic Monte Carlo simulations, because our simulations do not show the increase in methane selectivity (kinetic or equilibrium) with increasing pore width that is observed experimentally (Rao, Sircar & Golden, 1995). In addition, simulations show an increase in methane selectivity (kinetic and equilibrium) with increasing pressure (in pores lager than 12 Å) while experimentally a marked decrease is observed. [Note that 14 Å is a possible solution at low pressure, but not at high pressure (see Figure 4.6).] In conclusion, there is very strong evidence to support the realism of the simulations presented here, with all the evidence pointing to the gas separation in the SSF membrane being carried out in pores of around 6.4 – 6.5 Å. We note also that the simulated pore size has the same order of magnitude as the experimental pore size reported by Rao and Sircar (1993a, 1993b, 1995). Of course, the real membrane has a more disordered structure than our simple model, so this pore size should be interpreted as the size of the critical constrictions in the pore network, rather than the width of regularly-shaped pores; this aspect is considered in more detail in the next chapter.

4.4 Summary

The simulation results have shown that the pore width has a crucial role in the effectiveness of the separation process because it defines the adsorption capacity and the transport properties of the membrane material. Three distinct regions have been identified in the range of pore sizes:

i) Pores smaller than 6 Å have a sieving effect. The separation here is based on molecular size differences (*i.e.*, methane molecules are too big to enter and the small hydrogen molecules pass preferentially through the small pores of the membrane), and is the opposite of what is desired from an SSF membrane in industrial applications.

ii) Pores between about 6.3 and 10 Å show significant selective adsorption of methane. Here, high methane permeabilities and therefore high selectivities are achieved because methane molecules form a dense, but not tightly bound, adsorbed phase. An increase in pressure has relatively little effect on the methane density because the pores are close to their capacity. On the other hand, an increase in the pressure causes a significant decrease in the methane permeability as the adsorbed layer gets more compacted and less mobile. A maximum in the selectivity is observed at about 7 - 8 Å while the maximum in the permeability is observed at about 9 Å.

iii) In pores bigger than 10 – 12 Å, a preferential methane adsorption is observed close to the surface while hydrogen is restricted to the low-density region in the middle of the pore. In this pore size range, the separation is poorer because the hydrogen is able to diffuse effectively through the low-density region.

The SSF membrane depends for its separation performance on having pores in the second range. Despite using a simple model (with regular, slit-shaped pores) our

results show an excellent agreement between simulation and experiment. The real membrane has, of course, a network of interconnected pores, with the pores having a range of sizes. Effects due to the pore size distribution and pore network connectivity effects are addressed in the next chapter. The experimental selectivities and permeabilities (Golden, 2002) are bounded simultaneously by our simulation results in a narrow pore size range (*i.e.*, between 6.4- 6.6 Å). The equilibrium and kinetic selectivity show similar dependencies on the pore width. However the kinetic selectivity is smaller than the equilibrium selectivity as the greater mobility of the hydrogen molecules compensates for their lower density. Thus, the permeation selectivity is essentially determined by the selective adsorption at the feed side of the membranes as Rao & Sircar (1993b) suggested.

5. Pore Network Connectivity Effects on Gas Separation in a Microporous Carbon Membrane

Simulated transport in an SSF carbon membrane using a single-pore model was presented in the previous chapter. There, the membrane was represented by an array of identical, non-intersecting pores, providing a good agreement with experimental data for the purification of a refinery hydrogen stream. In this chapter, a critical path analysis (CPA) of transport through an SSF membrane operating in a hydrogen purification application is presented. Using experimental mixture permeability data as an input, the CPA allows us to estimate the structural parameters of the membrane. In addition, the CPA gives insight into the role of network connectivity, showing that the species selectively transported through the membrane (methane, in this case) and the species which it is intended the membrane should not transport (hydrogen) pass through essentially distinct sub-networks within the pore network of the membrane.

5.1 Percolation Theory

Although our single-pore model has provided a good agreement with experimental data, a real membrane contains pores of different sizes, connected together in a pore network, allowing the possibility of connectivity effects that are not accommodated by the single-pore model. In this chapter, a pore size distribution (PSD) and a mean coordination number define the pore network model. The pore network connectivity is a measurement of the internal topology of the membrane (*i.e.*, it accounts for the fact that the pores in a real pore network are interconnected).

5.1.1 Pore Network Connectivity and Mean Coordination Number

The connectivity of a pore network can be quantified in terms of the mean co-ordination number, which is the average number of pores that meet at each pore intersection. As an example, Figure 5.1 shows a two-dimensional simplified dimensional pore network in which the mean coordination number is 3.

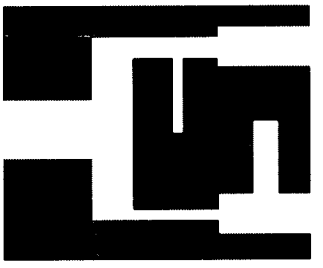

Figure 5.1 - Schematic representation of a simplified fragment two-dimensional pore network.

Liu & Seaton (1994) and Seaton (1991) have developed a method to estimate the mean coordination number based on equilibrium adsorption measurements and concepts of percolation theory for mesoporous materials. A method to estimate the mean coordination number in microporous materials was later proposed by López-Ramón *et al.*, (1997). The effect of the pore network connectivity in gas separation can be investigated by using the critical path analysis (CPA) of Ambegaokar, Halperin & Langer (1971).

5.1.2 Critical Path Analysis

The CPA of Ambegaokar, Halperin & Langer (1971), which was originally applied to hopping conduction in semiconductors, shows that, for a sufficiently broad distribution of conductances, transport is dominated by controlling conductances of a certain critical value, with conductances much larger or smaller than the critical value having little impact on the transport rate. MacElroy, Seaton & Friedman (1997) and Seaton *et al.*, (1997) applied the CPA to diffusion in the pore network of

carbon molecular sieves, in which the critical conductance of the original analysis of Ambegaokar, Halperin & Langer (1971) corresponds to a critical pore size (with larger pores having a higher diffusive "conductance"). To illustrate the application of the CPA to transport in a pore network, let us consider a "thought experiment" illustrated by the simplified fragment of the membrane shown in its two-dimensional analogue in Figure 5.2a. The transport direction is from left to right.

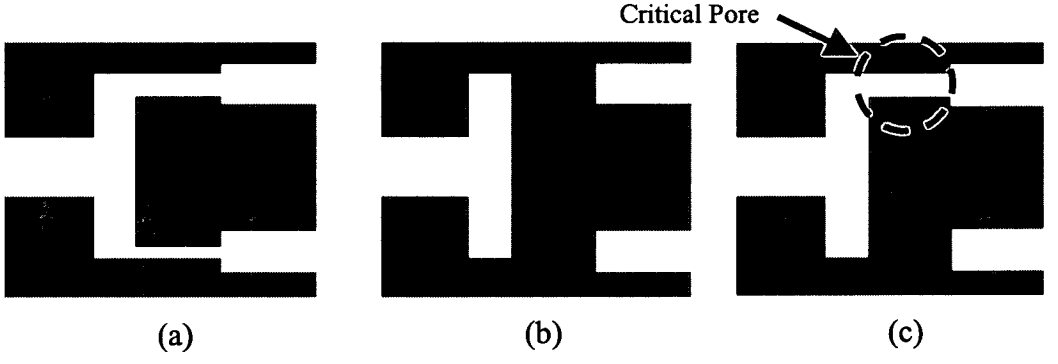

Figure 5.2 - Schematic representation of the critical path analysis.

To determine the critical pore one should first remove all of the pores from the network and then restore them, in their original positions, beginning with the pore that offers the least transport resistance to the flow. For the moment, it is assumed that the largest pores offer the least resistance to diffusion (i.e. that they have the highest diffusional conductance). This would be the case for molecular diffusion, as the cross-section available for transport increases with pore width, and also for Knudsen diffusion in which, in addition, the diffusion coefficient increases with pore width. [However, as we will see later, an interesting feature of the hydrogen/hydrocarbon membrane separation is that while the large pores do have the highest conductance for hydrocarbons, the picture is more complicated for hydrogen.] Figure 5.2b shows a partially restored network, in which some of the larger pores have been replaced, but not sufficient to re-establish a percolating network, in which transport can again occur. When one places the pore that re-establishes a percolating network, allowing transport between both sides, one has located the critical pore size, indicated by a dashed circle in Figure 5.2c. Replacing the remaining pores restores the complete network shown in Figure 5.2a. It is helpful here to consider the pore network, in its various stages of reconstruction, as a

network of conductors, analogous to an electrical circuit. Let us consider the network just after the critical pore has been replaced (Figure 5.2c). At this stage, all the other pores have larger conductances than the critical pore, and all the molecules that diffuse through the other pores also pass through the critical pore, as it is the one that has re-established the percolating network. The just-percolating network of Figure 5.2c is thus effectively one of conductances in series; the critical pore is in series with a network of pores with higher conductances. For a wide distribution of conductances, as in the analogous electrical circuit, transport is controlled by the smallest conductance (or, equivalently, the highest resistance) – the critical pore.

What happens when the rest of the pores (all smaller than the critical pore, and having lower conductances) are replaced to restore Figure 5.2a? The remaining conductances are effectively in parallel with the critical pore, and so (again for a wide distribution of conductances) may be neglected. Thus, diffusion through the network, and separation selectivity, is determined not by the PSD as a whole, or by the mean pore size, but by the critical pore size. In the context of molecular sieving, CPA gives the initially counter-intuitive result that even solids with wide PSDs can carry out sieving (MacElroy, Seaton & Friedman, 1997; Seaton *et al.*, 1997); this explains, for example, how carbon molecular sieves can separate oxygen from air when oxygen and nitrogen have very similar kinetic diameters. In that case, it turns out that the critical pore size (but not the other pores in the PSD) are the right size to allow rapid diffusion of oxygen relative to nitrogen. The application of CPA to gas separation in surface-flow membranes is more complex, and very insightful, as we shall see below.

5.1.3 Percolation Threshold

The percolation threshold, p_c, is the minimal fraction of pores needed to establish the flow between both sides of the membrane (Sahimi, 1994). A percolating cluster of pores is formed when the cumulative fraction of the pores that have conductance higher than the critical conductance, g_c, reaches the percolation threshold of the

network (*i.e.* the fraction of the pores that have to be "present" in order to form a connected path across the material).

$$p_c = \int_{g_c}^{\infty} h(g)\, dg \tag{5.1}$$

where $h(g) = \frac{d\mathcal{N}}{dg}$ is the normalised conductance distribution function (here, $\mathcal{N}$ is the number of pores, normalised to unity) and g_c is the critical conductance (*i.e.* the conductance of the critical pore). Equivalently, one can integrate over the normalised PSD, $f(w) = \frac{d\mathcal{N}}{dw}$, for pores which have a size such that $g > g_c$. Thus,

$$p_c = \int_{w:\, g(w) > g_c} f(w)\, dw \tag{5.2}$$

The percolation threshold depends on the topology on the network, and in particular on its coordination number (Z). The percolation thresholds of all three-dimensional networks can be approximated by the following empirical equation (Sahimi, 1994):

$$p_c \approx \frac{3}{2Z} \tag{5.3}$$

The normalised PSD of the surface-flow membrane is approximated by a lognormal distribution:

$$f(w) = \frac{1}{w\sigma\sqrt{2\pi}}\, e^{-\frac{(\ln(w)-\mu))^2}{2\sigma^2}} \tag{5.4}$$

where μ and are σ parameters. The lognormal distribution is asymmetrical, having an initial sharp increase and a long tail; this is characteristic of PSDs in many microporous solids, reflecting the fact that the PSD is bounded by $w = 0$ on the left, and effectively unbounded on the right.

5.1.4 Pore Conductances

In an electrical circuit, Ohm's law relates the electrical conductance, g_i^e, with electrical current, I_i^e, and the electrical potential difference, ΔV_i^e by the equation:

$$I_i^e = g_i^e \, \Delta V_i^e \tag{5.5}$$

By analogy, the molar flow, F_i, can be related to the variation of bulk gas density, ΔC_i, by the pore conductance, $g_i(w)$, in each individual pore:

$$F_i(w) = g_i(w) \, \Delta C_i, \quad C_i = \frac{P_i}{RT} \tag{5.6}$$

The pore conductances in each individual pore, $g_i(w)$, can be either calculated from the simulated fluxes (reported in Chapter 4) using Equation 5.6 or by relating the permeability, K, to the pore conductance:

$$g_{c,i} = K_i \left(\frac{w \times L_y}{L_x} \right) RT \tag{5.7}$$

where w, L_y and L_x are respectively the width, breadth and length of the simulated pore (so that $w \times L_y$ is the cross-sectional area). [In the NEMD simulations, periodic boundary conditions are applied in the direction at right angles to the width and length of the pore, so that although the pore has a defined breadth, there is no physical boundary in this direction.] In the NEMD simulations, L_x = 40.47 Å and L_y = 39.35 Å, so:

$$g_{c,i} = 0.97238 K_i \; w \; RT \tag{5.8}$$

Figure 5.3 shows the variation of the pore conductance with pore width. While the conductance for methane increases monotonically with pore width, the behaviour of

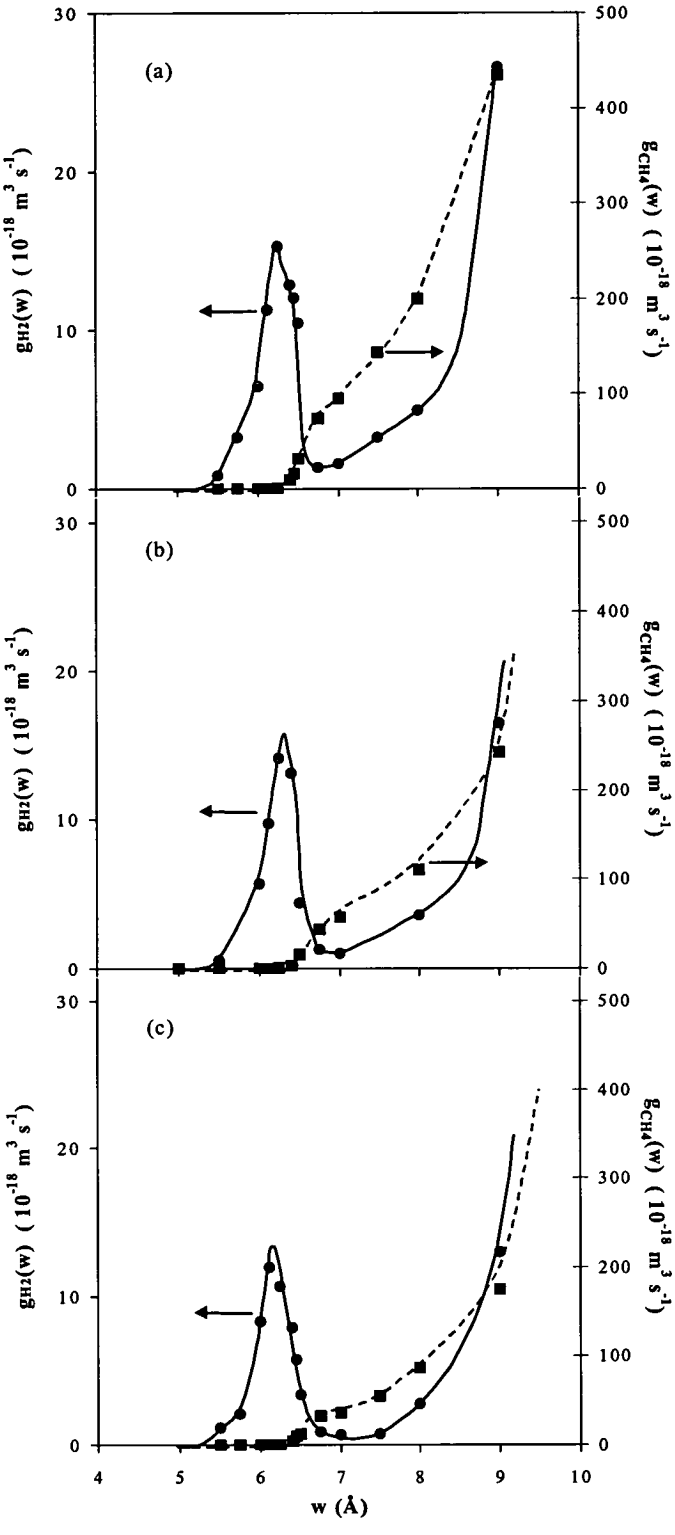

Figure 5.3 - Variation of the pore conductance with the pore width. The feed-side pressures studied are (a) 11.3 bar; (b) 32.0 bar; and (c) 55.6 bar. The solid line and the circles represent hydrogen and dashed line and the squares represent methane.

hydrogen is more complicated. In pores large enough to allow the adsorption of methane (above about 6.3 Å), the diffusion of hydrogen is hindered by the presence of adsorbed methane, which is itself able to diffuse preferentially across the membrane. In larger pores, where the adsorbed methane layers do not occupy the whole pore space, hydrogen is again able to diffuse more freely, giving the minimum in the hydrogen diffusional conductance as a function of pore width.

5.1.5 Critical Pore Size

In this work, the critical pore size is defined as the pore size where the simulated permeability equals the experimental permeability. Table 5.1 shows the critical pore sizes used in this work. Linear interpolation between the simulated permeabilities that bound the experimental permeability is used to calculate w_c^i. The critical pore size is found to be essentially independent of pressure, as it should be, given that it is a characteristic of the pore network. [Since w_c represents the pore widths where the simulated permeability matches the experimental value, and the conductance is proportional to both the permeability and the pore width, the critical conductance increases linearly with the value of w_c^i.] The experimental conditions studied are a 50 % methane/hydrogen mixture; temperature of 295 K; and effluent pressure of 1.7 bar. The feed side pressures studied are 11.3 bar, 32.0 bar and 55.6 bar (Golden, 2002).

Table 5.1 – Critical pore sizes and the corresponding critical conductances.

Species	$w_c^{i\,\prime}$ (1) (Å)	Feed-side pressure (bar)					
		11.3		32.0		55.6	
		K_i (2)	g_c (3)	K_i (2)	g_c (3)	K_i (2)	g_c (3)
hydrogen	6.0 ± 0.05	4.0	5.8	3.7	5.2	5.6	8.6
	6.5 ± 0.3	4.0	6.2	3.7	5.7	5.6	9.3
	8.5 ± 1.0	4.0	8.1	3.7	7.4	5.6	12.2
methane	6.4 ± 0.06	7.3	11.2	6.1	9.4	3.5	15.5

(1) average over all three feed-side pressures. The error is calculated using the t-test with a confidence level of 95 %.

(2) Values of experimental pore permeabilities. Units of permeability are 10^{-12} mol m^{-1} s^{-1} Pa^{-1}.

(3) Units of pore conductance are 10^{-18} m^3 s^{-1}

5.2. Pore Size Distribution

5.2.1 Implementation of the CPA

The application of the CPA to our pore network model is illustrated by considering a pore network having a coordination number, Z = 6 (corresponding, from Equation 5.3, to p_c = 0.25) and for a feed pressure of 11.3 bar. For methane, the conductance increases with pore width so one needs to integrate between a single critical pore size, $w_{c1}^{CH_4}$, and $w = \infty$ (indicated graphically by the shaded area in Figure 5.4a). Thus, for methane Equation 5.2 becomes:

$$\int_{w_{c1}^{CH_4}}^{\infty} f(w)\,dw = \frac{3}{2Z} \tag{5.9}$$

Because, for hydrogen, the pore conductance has a minimum as a function of pore width, the calculation is more complicated. Now, there are different three critical pore sizes corresponding to the same permeability, $w_{c1}^{H_2}$, $w_{c2}^{H_2}$ and $w_{c3}^{H_2}$ (Figure 5.4b). Equation 5.2 becomes:

$$\int_{w_{c1}^{H_2}}^{w_{c2}^{H_2}} f(w)\,dw + \int_{w_{c3}^{H_2}}^{\infty} f(w)\,dw = \frac{3}{2Z} \tag{5.10}$$

The pore network model has three parameters - μ, σ and Z – while the CPA provides two equations – 5.9 and 5.10. It is thus not possible to obtain a unique solution for the model parameters. By fixing Z, however, a unique PSD is obtained. This is shown for Z = 6 in Figure 5.5, along with the areas of the PSD corresponding to the solution of Equation 5.9 and Equation 5.10.

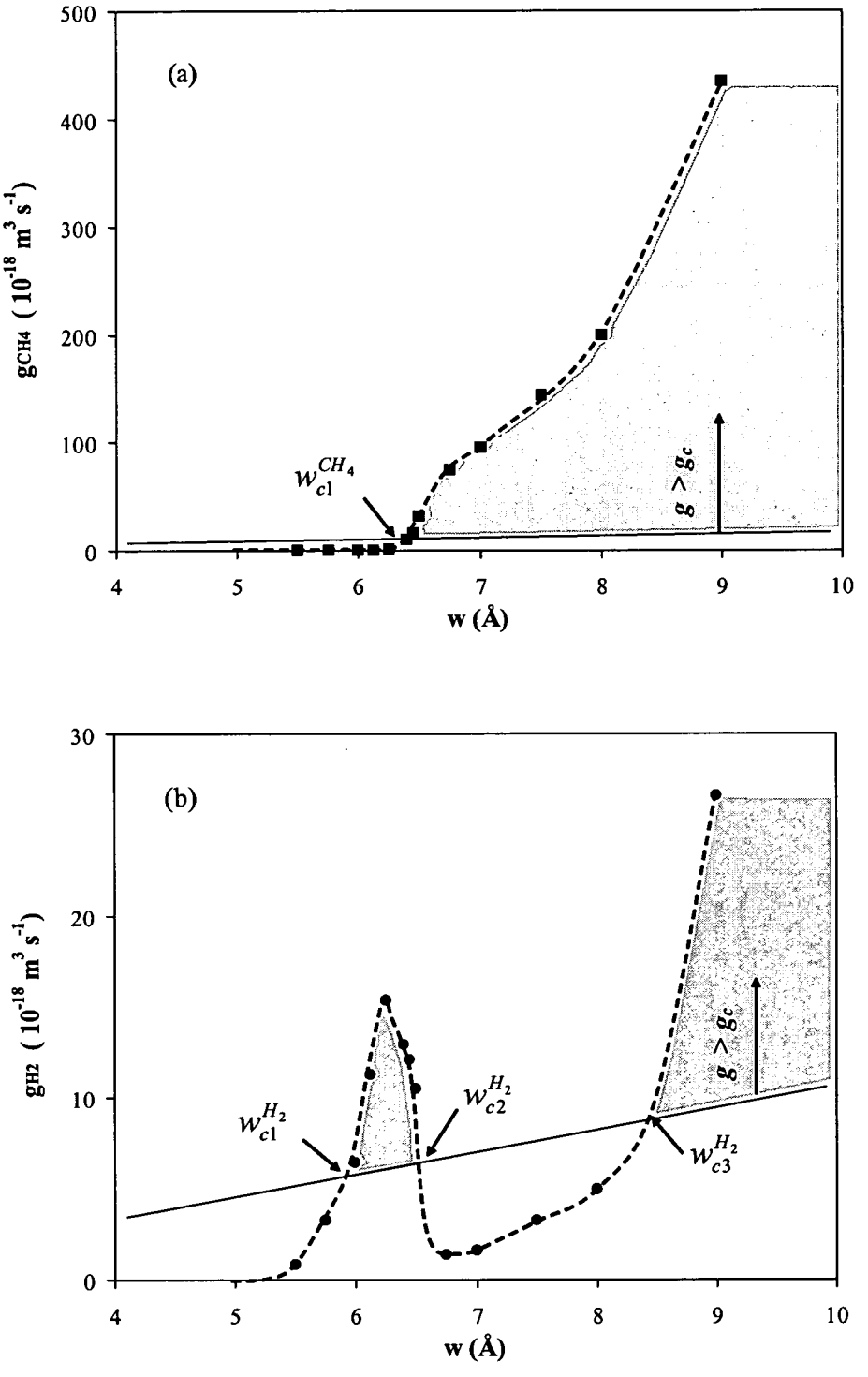

Figure 5.4 – Example of the variation of the pore conductance with the pore size: (a) methane and (b) hydrogen for the feed pressure of 11.3 bar. Solid line demarks conductances that have the same permeability. The critical pore sizes (w_c^i) for each species are also indicated.

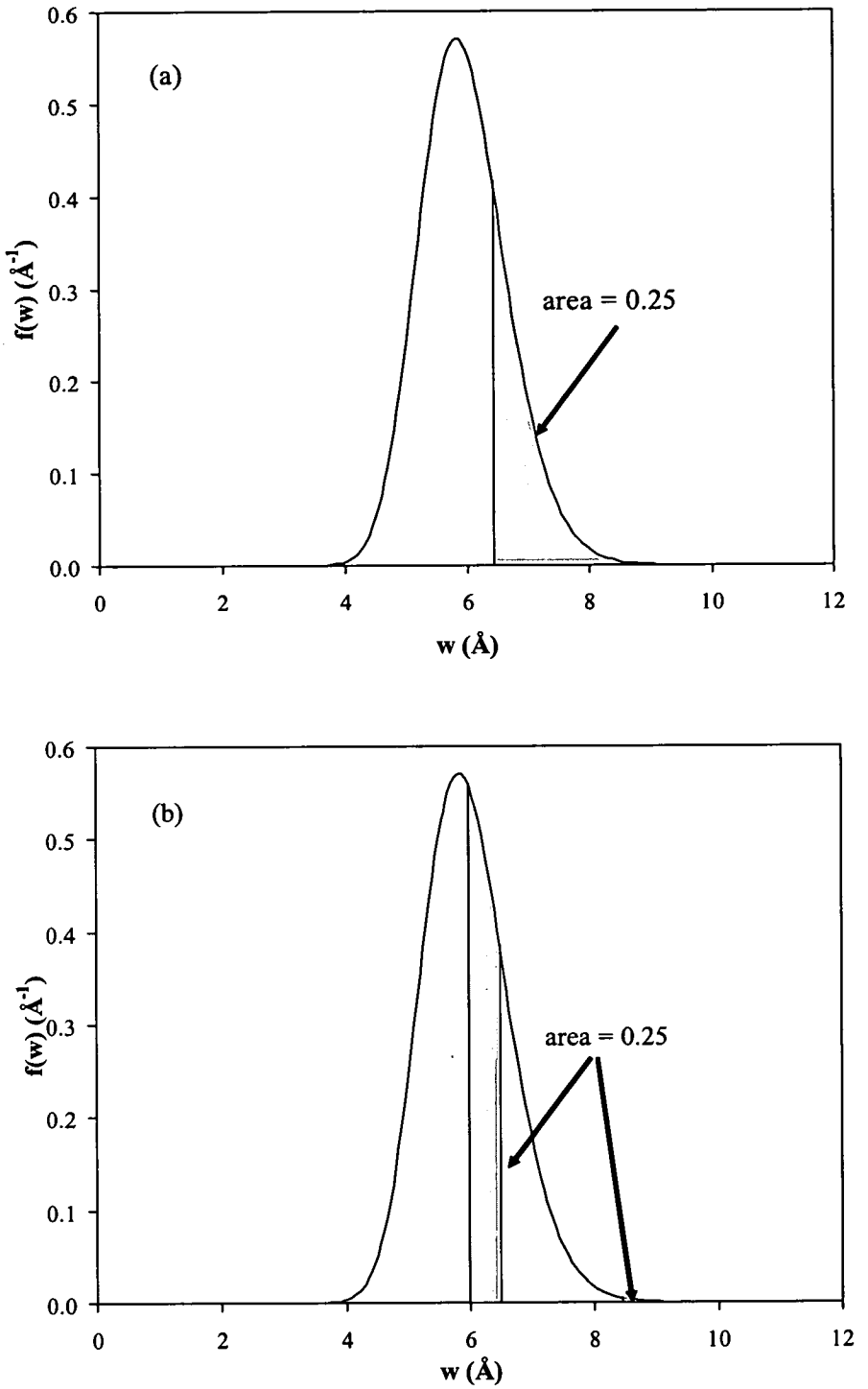

Figure 5.5 – PSD obtained from the CPA for $Z = 6$, showing the area corresponding to the integral of Equation 5.4 (a) for methane and (b) hydrogen.

From Figure 5.5, it can be seen that the diffusion of methane occurs primarily in pores larger than $w_{c1}^{CH_4}$ = 6.4 Å, while almost all the hydrogen flows through pores between $w_{c1}^{H_2}$ = 6.0 and $w_{c2}^{H_2}$ = 6.5 Å. [The contribution from the few pores larger than $w_{c3}^{H_2}$ = 8.5 Å is negligible.] Thus, the CPA result shows that hydrogen and methane are mostly diffusing through different sub-networks within the overall network (sharing only pores in the size range 6.4 - 6.5 Å). The physical picture, then, is of two three-dimensional sub-networks, each containing a proportion of the pores (25% for Z = 6), but interconnecting only occasionally in their occupation of the overall pore network. It is worth emphasising that this physical insight, and the quantification of the critical pore sizes, can only be obtained by applying the CPA to the pore network model; a single-pore model, however realistic at an atomic level, completely misses this phenomenon.

5.2.2 Pore Network and Connectivity Effects

The effect of different pore network coordination numbers, Z, on the PSD is shown in Figure 5.6. The modal pore size decreases and the width of the PSD increases with increasing Z. The number of pores larger than 8 Å is very small for all the PSDs. However, the PSD obtained from the CPA, which is determined by an analysis of steady-state diffusion, does not probe the size distribution of dead-end pores, which make no contribution to transport (see Figure 5.7b). It is thus, in principle, different from a PSD measured by an equilibrium-based method such as gas adsorption (see Figure 5.7a).

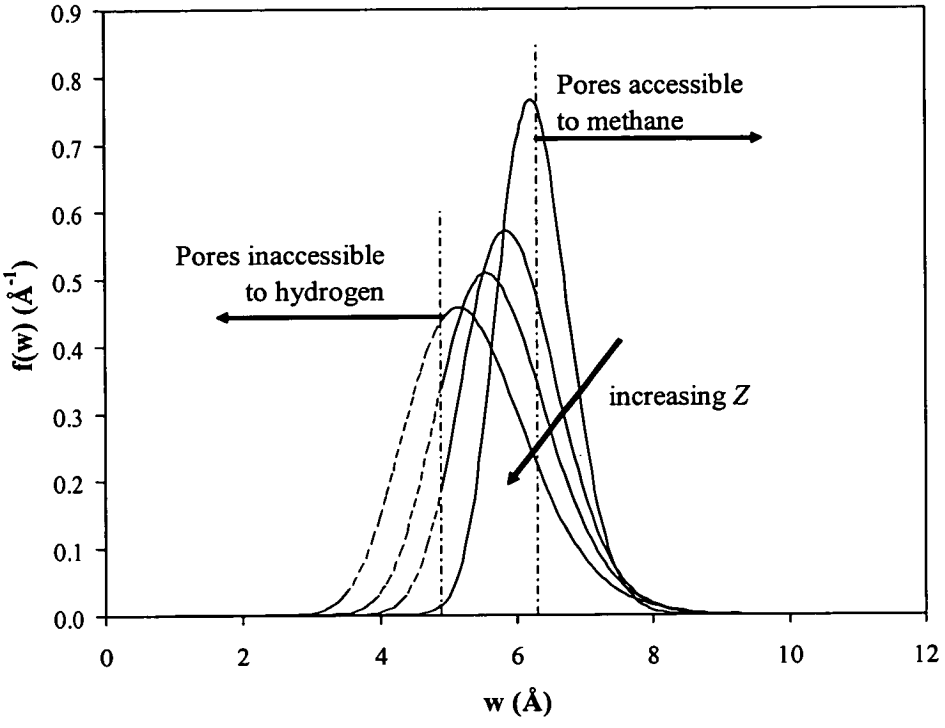

Figure 5.6 – Effect of the pore network structure (Z = 4, 6, 8, 12) on the PSD. The pore sizes that delimit the accessibility of each species are also indicated.

Thus, if the PSD is represented, as an example, by the two dimensional pore network shown in Figure 5.7a the CPA does not take into account the dead-end pores because there do not contribute to the flow. Thus, our PSD represents an open-pore size distribution, in which the gas mixture can flow (Figure 5.7b), which can be different from the PSD obtained from equilibrium measurements. However, if the dead-end pores have the same size distribution as the pores that contribute to transport, in other words that geometry and local connectivity are uncorrelated (which is likely to be a reasonable assumption for many materials) the two PSDs are equivalent.

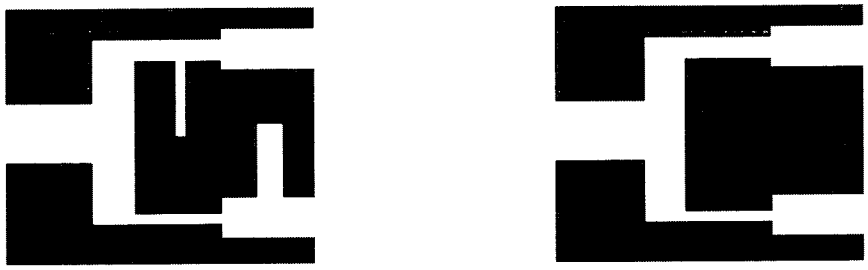

(a) (b)

Figure 5.7 – Schematic representation of (a) a simple two-dimensional pore network and (b) the same network showing only the pores that contribute to the flow.

5.3. Summary

In the previous chapter, experimental observations in an SSF membrane were described in terms of a single-pore model. In this chapter, the effect of the pore network connectivity in gas separation by using the CPA is investigated. Our pore network model is characterised by a PSD (based on assumed values of the coordination number Z) that reproduces the experimentally observed permeabilities for methane and hydrogen in a hydrogen purification application; according to our results, the exprimental PSD is between about 4 and 8 Å. Our results are supported by the experimental measurements of the pore size made by Rao & Sircar (1993a; 1993b; 1995). In addition, the shape of the PSD calculated with a coordination number of 4 is the PSD is very close to the experimental PSD (see Figure 1.3) reported by Rao & Sircar (1995). The permeability data for two species are not sufficient to simultaneously fit Z and the PSD. However, with permeability data for a third species, it would have been possible to fit all the structural parameters; this is generally true for a molecular simulation/CPA analysis. The match between the CPA and experiment is, overall, extremely good, demonstrating that our model presented here can quantitatively describe the performance of the SSF membrane.

The CPA provided a physical insight into an intrinsically connectivity related effect that cannot be studied using a single-pore model. The two species flow in separate sub-networks, consisting of largely independent populations of pores, with methane

in pores wider than 6.4 Å and hydrogen in pores between 6.0 and 6.5 Å. This has implications for the design and synthesis of SSF membranes because it suggests that a selective pore blockage of small pores, by appropriate methods, would reduce the permeability to hydrogen, while leaving the methane permeability unaffected, and thereby produce a significant increase in the separation selectivity. The success of the molecular simulation/CPA approach in this application suggests that it might be a more generally useful tool for the design of membranes for gas separation.

6. Conclusions

This research involves the mathematical modelling, at molecular level, of adsorption and diffusion in microporous carbon materials and in particularly the SSF carbon membrane developed by Air Products and Chemicals, Inc. We have a particular interest in hydrogen recovery from a hydrogen/hydrocarbon refinery waste mixture. Molecular simulation methods are used to predict the performance for hydrogen/hydrocarbon mixture separation. Equilibrium diffusion is calculated by MD, in which the molecular positions are obtained by numerically solving Newton's differential equations of motions, while adsorption is calculated using the GCMC method, in which the positions are generated stochastically and are not temporally dependent. DCV-GCMD method is uniquely suited to the direct measurement of transport diffusion in the presence of a gradient of concentration or pressure (because the real experiment is reproduced by choosing two different pressures, or concentrations and therefore the driving force across the simulation pore can be defined).

The GMS diffusion equations of Krishna (1990) are used to calculate diffusion coefficients. The cross-diffusion coefficients and viscous flow are found to be negligible. In addition, the Maxwell-Stefan diffusion coefficients are also found to be composition independent, providing evidence that supports the applicability of the GMS equations to describe mass transport. The simulation results have shown that the pore width has a crucial role in the effectiveness of the separation process because it defines the adsorption capacity and the transport properties of the membrane material. Three distinct regions have been identified in the range of pore sizes:

- Pores smaller than 6 Å have a sieving effect. The separation here is based in molecular size differences (*i.e.*, small hydrogen molecules pass preferentially through the small pores of the membrane).

- Pores between about 6.3 and 10 - 12 Å show significant selective adsorption of methane (blocking hydrogen molecules from adsorbing and diffusion into the pore). Here, high methane permeabilities and therefore high selectivities are achieved because methane molecules form a dense, but not tightly bound, adsorbed phase. Both hydrogen fluxes and permeabilities are strongly affected by the presence of methane (because methane adsorbs more strongly in the pore, thereby excluding the hydrogen molecules. However, the methane properties (adsorbed densities and diffusivities) are not affected significantly by the presence of hydrogen in the mixture. An increase in pressure has relatively little effect on the methane density because the pores are close to their capacity. On the other hand, an increase in the pressure causes a significant decrease in the methane permeability as the adsorbed layer gets more compact and less mobile. A maximum in the selectivity is observed at about 7 - 8 Å while the maximum of permeability is observed at about 9 Å.

- In pores bigger than 10 – 12 Å, a preferential methane adsorption is observed close to the surface while hydrogen is restricted to the low-density region in the middle of the pore. As the pore width increases, the void space between walls increases allowing hydrogen molecules to enter more easily. In this pore size range, the separation is poorer because the hydrogen is able to diffuse effectively through the low-density region. This results in a decrease in selectivity resulting in the loss of kinetic selectivity. Hydrogen fluxes and permeabilities are proportional to the pore size, denoting Knudsen diffusion. The methane molecules are mainly located at the pore surface while the hydrogen molecules are more located at the centre of the pore. Methane transport occurs mainly due to the flow of the methane adsorbed layers on the surface. In the middle region of the pore, the flow pore follows the Knudsen theory.

The SSF membrane separation performance depends on having pores in the second range. Although we are using a simple model (with regular, slit-shaped pores) the results shows an excellent agreement between simulation and experiment. The experimental selectivities and permeabilities (Golden, 2002) are bounded

simultaneously by our simulation results in a narrow pore size range (*i.e.*, between 6.4- 6.6 Å). However, these results presented are described in terms of a single-pore model and the assumption that all pores are open to the surface is unlikely to occur in a real material (because the pores in a real pore network are interconnected). A real membrane (or adsorbent) contains pores of different sizes, connected together in a pore network, allowing the possibility of connectivity effects that are not accommodated by a single-pore model. The effect of the pore network connectivity in gas separation was investigated by the critical path analysis (CPA) of Ambegaokar, Halperin & Langer (1971). We have found that the match between the CPA and experiment is, overall, extremely good, demonstrating that the pore model presented in this thesis can quantitatively describe the performance of the SSF membrane. In addition, methane and hydrogen flow in separate sub-networks, consisting of largely independent populations of pores, with methane in pores wider than 6.4 Å and hydrogen in pores between 6.0 and 6.5 Å. Thus, the CPA provided a physical insight into an intrinsically connectivity related effect that cannot be studied using a single-pore model

We have shown in this thesis that molecular simulations can provide us with an efficient tool to investigate the behaviour of a given system for different porous structures, and for different operating conditions. Furthermore, molecular simulations can serve as a tool for the design of new adsorbents and membranes with higher selectivities. For example, the success of the molecular simulation/CPA approach in this application suggests that the selective pore blockage of small pores in the SSF membrane, by appropriate methods, would reduce the permeability to hydrogen, producing a significant increase in the separation selectivity.

We have identified that the transport mechanism in the middle region of pores follows the Knudsen theory in pores larger than about 14 – 16 Å. However, little investigation of the flow near the walls was made to fully characterise the transport flow. We have shown that the dependence on temperature of this diffusion is similar to activated diffusion in *e.g.* zeolites. However, additional analyses would be needed to be carried out to fully characterise the flow near the wall.

Given the recent increase of carbon materials importance (due to their highly porosity and relative inertness) it is important to develop molecular-level simulations tools, which can be applied in the design of new materials. In the future, the current work should be extended, in a first step, to higher molecular weight hydrocarbons (up to C_4H_{10}) and then to polar components (*e.g.* CO_2 and H_2S). The diffusion molecules should be initially assumed to be Lennard-Jones spheres and later the molecular structure should be taken into consideration (see *e.g.*, Heuchel *et al.* 1999; Smit, 1995 and Toxvaerd, 1990). The importance of the entrance and exit effects (see *e.g.* MacElroy & Boyle, 1999) should also be evaluated and addressed in the continuation of this research. The PSD and the pore network coordination number can be determined by analysis of equilibrium adsorption data (see *e.g.*, López-Ramón *et al.*, 1997 and Seaton, 1991). The results obtained could be then compared with the PSD obtained from the CPA of Ambegaokar, Halperin & Langer (1971) described in this work. In the longer term, by understanding the factors that effect a particular separation we may optimise existent materials (or create new materials) by appropriate methods to a particular separation (Sircar & Rao, 1993b).

Appendix I. – Air Products Experimental Data

The experimental results shown in Chapter Four and Chapter Five were obtained from the Air Products and Chemical Inc. laboratories (Golden, 2002). A schematic representation of the Air Products experimental Selective Surface Flow (SSF) membrane is shown in Figure I.1. There, F is the feed flow rate, F_e is the high pressure effluent (HPE) flow rate, F_p is the low pressure permeate effluent (LPE) flow rate and P_H and P_L are the pressure on the feed side and on the permeate side. The compositions are the following: $\{y_{fi}\}$ in the feed, $\{y_{ei}\}$ in the high-pressure effluent and $\{y_{pi}\}$ in the permeate. A full description of Air Products experimental apparatus set-up can be found described in detail elsewhere (Anand, 1995).

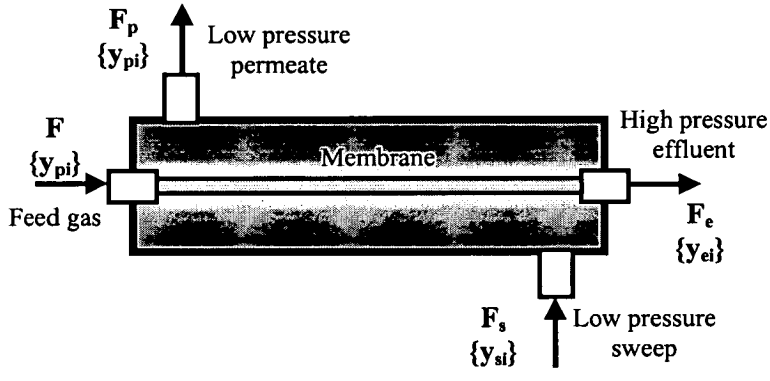

Figure I.1 – Schematic representation of the SSF membrane.

The permeability of each component through the membrane can be calculated using the steady-state values of flow rates and compositions by the following equation:

$$F_{pi} = \left(A_m\ \varepsilon_p\right)\frac{K_i}{L_x}\frac{\Delta P_i\big|_I - \Delta P_i\big|_{II}}{\ln\left(\dfrac{\Delta P_i\big|_I}{\Delta P_i\big|_{II}}\right)} \tag{I.1}$$

where F_{pi} is the steady state permeate molar flow rate of component i. $\Delta P_i\big|_I$ is the partial pressure difference between the high and low pressure sides of the membrane at the high-pressure gas entrance. $\Delta P_i\big|_{II}$ is the partial pressure difference between the high and low pressure sides of the membrane at the high-pressure gas exit. A is the membrane area and L_x is the membrane thickness. To be able to compare directly the experimental permeabilities with our simulation results we multiply the total area by the membrane porosity, ε_p. Air Products and Chemicals provided us with the raw data - *i.e.* operating conditions, flows and compositions - and we calculated the transport properties shown in this thesis using the above equation.

Rao & Sircar (1993a; 1993b) have estimated porosity of about 0.36 for the SSF membranes. In addition, the membrane is 50.38 cm^2 (Golden 2002) and total membrane thickness 2.5 μm (Rao & Sircar, 1993b). The experimental values of the pore permeability (calculated via Equation I.1) and selectivity (calculated via Equation 3.25) are complied in Table I.1.

Table I.2 – Air Products experimental results for the SSF membrane.

run	T	F_{CH4} (mmol s^{-1})			F_{H2} (mmol s^{-1})			P (Bar)		K (10^{-12} × mol m^{-1} s^{-1} Pa^{-1})		S
#	(°C)	Feed	HPE	LPE	Feed	HPE	LPE	HPE	LPE	CH4	H2	[-]
1a	22.4	4.77	2.48	2.40	4.52	2.97	1.58	11.5	1.7	7.16	4.11	1.74
2a	23.3	7.90	5.52	2.47	7.60	6.05	1.52	11.5	1.7	7.36	4.08	1.80
3a	23.3	16.45	13.82	2.57	15.32	13.82	1.38	11.5	1.7	7.54	3.95	1.91
4a	22.4	2.45	0.38	2.22	2.33	0.65	1.72	11.5	1.7	7.08	3.99	1.78
1b	19.2	10.88	4.87	6.42	10.42	6.30	4.22	32.0	1.7	6.06	3.50	1.73
2b	20.4	7.63	1.80	6.20	7.42	2.90	4.55	32.0	1.7	6.10	3.64	1.68
3b	20.4	5.45	0.10	5.70	5.25	0.35	5.13	32.0	1.7	5.97	3.76	1.59
4b	24.1	12.22	6.07	6.55	12.38	7.77	4.27	32.0	1.7	6.34	3.71	1.71
1c	20.8	15.17	7.80	7.15	15.73	6.00	10.58	56.3	1.8	3.40	5.49	0.62
2c	20.8	11.93	3.75	7.85	12.37	2.88	10.73	56.3	1.7	3.63	5.43	0.67
3c	20.2	9.62	1.58	8.60	9.98	0.53	10.18	56.3	1.8	3.43	5.90	0.58

Appendix II. - Nomenclature

a ..... Acceleration.

A ..... Pore cross-section area.

A_m ..... Membrane total area.

b ..... Langmuir adsorption constant.

B_o ..... Pore permeability.

$\bar{c}$ ..... Average molecular speed.

d ..... Dimensionality of the system.

$\mathcal{D}_i$ ..... Self diffusion.

$Đ$ ..... Maxwell Stefan diffusion.

D ..... Transport diffusion (total).

D^s ..... Surface diffusion.

D^k ..... Knudsen diffusion.

D^{kp} ..... Total Knudsen diffusion.

D^p ..... Contribution of the Knudsen diffusion and molecular diffusion.

E ..... Total energy.

E_a ..... Activation energy.

f ..... Fugacity.

$f(w)$ ..... Normalised pore size distribution.

F ..... Force.

g ..... Pore conductance.

g_c ..... Critical pore conductance.

g_i^e ..... Electrical conductance.

$h(w)$ ..... Conductance function.

H ..... Henry's constant.

I_i^e ..... Electrical current intensity.

J ..... Diffusive flux.

K ..... Pore permeability.

$\mathcal{K}$ ..... Dimensionless adsorption equilibrium constant.

K_b ..... Boltzmann constant.

Kn ..... Knudsen number.

L ..... Phenomenological coefficients.

L_x ..... Thickness of the simulated membrane or pore.

L_y ..... Breadth of the simulated pore.

M ..... Molecular weight.

m_o ..... Langmuir pore nonolayer capacity.

n ..... Number of species.

$\mathcal{N}$ ..... Number of molecules.

N ..... Net flux.

N_a ..... Avogadro number.

P ..... Bulk pressure.

$\mathcal{P}$ ..... Probability of acept/reject Monte Carlo trial.

p_c ..... Percolation threshold.

q ..... Quadrapole charge.

r ..... Position (scalar).

$\boldsymbol{r}$ ..... Position (vector).

R ..... Ideal gas constant.

S^{eq} ..... Equilibrium selectivity.

S^{k} ..... Kinetic selectivity.

t ..... Time.

t ..... Monolayer thickness.

T ..... Temperature.

U ..... Total potential energy.

v ..... Velocity.

V ..... Volume.

w ..... Pore width.

w_0 ..... Smallest pore in which diffusion takes place.

w_c ..... Critical pore size.

W ..... Pore deep.

x ..... Mole fraction of the adsorbed phase.

x, y, z ..... Cartesian co-ordinates.

z ..... Total number of collisions per second.

y ..... Mole fraction of the bulk phase.

Z ..... Mean coordination number.

Greek letters

β ..... Reciprocal of the absolute temperature.

ε ..... Potential well-depth in the Lennard-Jones Interaction potential.

ε_p ..... Membrane porosity.

ε_0 ..... Vacuum permittivity.

σ ..... Diameter of the interaction site in the Lennard-Jones interaction potential.

Δ ..... Spacing of the sheets of graphite used in the Steele potential.

Δt ..... Sample time.

ΔV_i^e ..... Electrical potential difference.

Γ ..... Darken thermodynamic factor.

ρ ..... Adsorbed density.

ρ^K ..... Adsorbed density in the middle of the pore.

ρ^S ..... Adsorbed layer density.

ρ_s ..... Surface density of carbon atoms used in the Steele potential.

μ ..... Chemical potential.

δt ..... Simulation time step.

θ ..... Surface coverage.

η ..... Viscosity.

λ ..... Mean free path.

ω ..... Knudsen flow probability factor.

Appendix III. - References

Alder, B. J. & Wainwright, T. E. (1959) Studies in Molecular Dynamics. I. General Method, *Journal of Chemical Physics*, **31**, 459-466.

Allen, M. P. & Tildesley, D. J. (1989). *Computer Simulation of Liquids*. Oxford: Clarendon Press.

Ambegaokar, V., Halperin, B. I. & Langer, J. S. (1971). Hopping conductivity in disordered systems. *Physical review B*, 4 (8), 2612-2620.

Anand, M. (1995). Novel selective surface flow membranes for the recovery of H_2 from waste gas streams. Phase I: exploratory development; Final report to Department of Energy (US).

Anand, M. & Ludwig, K. (1996). Novel selective surface flow membranes for the recovery of H_2 from waste gas streams. Phase II: technology development; Final report to Department of Energy (US).

Andersen, H. C. (1980). Molecular dynamics at constant pressure and or temperature . *Journal of Chemical Physics*, 72, 2384-2393.

Arya, G., Chang, H.C. & Maginn, E. J. (2001). A critical comparison of equilibrium, non-equilibrium and boundary-driven molecular dynamics techniques for studying transport in microporous materials. *Journal of Chemical Physics*, 115 (17), 8112-8124.

Atkins, P. W. (1994). *Physical Chemistry*. 5th Edition. London: Oxford University Press.

Bell, W. B. & Brown, L. F. (1974). Kinetic theory approach to simultaneous gas and surface diffusion in capillaries. *The Journal of Chemical Physics*, 61 (2), 609-618.

Clausing, P. (1931). Über die Strömunf sehr verdünnter Gase durch Röhren von beliebiger Länge. Annal der Physik, 5 (12), 961-989.

Clausing, P (1971). The flow of highly rarefied Gases through Tubes of Arbitrary length. Journal of Vacuum Science and Techonology, 8 (5), 636-646. [English translation from the original German paper Clausing (1931).]

Cracknell, R. F. (2001). Molecular simulation of hydrogen adsorption in graphitic nanofibres. *Physical Chemistry Chemical Physics*, 3 (11), 2091-2097.

Cracknell, R. F., Nicholson, D. & Gubbins, K. E. (1995). Molecular dynamics study on the self-diffusion of supercritical methane in slit-shaped graphitic micropores. *Journal of the Chemical Society. Faraday transactions*, 91 (9), 137-1383.

Cracknell, R. F., Nicholson, D. & Quirke, N. (1993). A grand canonical Monte Carlo study of Lennard-Jones mixtures in slit shaped pores. *Molecular Physics*, 80 (4), 4885-897.

Cussler, E. L. (1997). *Diffusion – mass transfer in fluid systems*. 2nd Edition. London: Cambridge University Press.

Darkrim, F. & Levesque, D. (1998). Monte Carlo simulations of hydrogen adsorption in single-walled carbon nanotubes. *Journal Chemical Physics*, 109 (12), 4981-4984.

Davies, G. M (1999). *Molecular simulation of adsorption equilibrium in microporous solids: model development and performance prediction.* PhD thesis, University of Cambridge.

Davies, G. M. & Seaton, N. A. (1999). Development and validation of pore structure models for adsorption in activated carbons. *Langmuir*, 15 (19), 6263-6276.

Do, D. D. (1998). *Adsorption analysis: equilibria and kinetics*. London: Imperial College Press.

Frenkel, D. & Smit, B. (1996). *Understanding Molecular Simulation - From Algorithms to Applications*. London: Academic Press.

Furukawa, S. S., Hayashi, K. & Nitta, T. (1997). Effects of surface heterogeneity on gas permeation through slit-like carbon membranes by non-equilibrium molecular dynamics. *Journal Chemical Engineering of Japan*, 30 (6), 1107-1112.

Furukawa, S. S. & Nitta, T. (1997). Computer simulation studies on gas permeation through nanoporous carbon membranes by non-equilibrium molecular dynamics. *Journal Chemical Engineering of Japan*, 30 (6), 116-122.

Furukawa, S. S., Shigeta, T. & Nitta, T. (1996). Non-equilibrium molecular dynamics for simulation permeation of gas mixtures through nanoporous carbon membranes. *Journal Chemical Engineering of Japan*, 29 (4), 725-728.

Glicksman, M. E. (2000). *Diffusion in solids – field theory, solid-state principles and applications*. London: John Wiley.

Gregg, S. J. & Sing, K. S. W. (1982). *Adsorption, surface area and porosity*. 2nd Edition. London: Academic Press.

Golden, T. C. (2002). Air Products and Chemicals Inc. Personal Communication.

Haile, J. M. (1992). *Molecular Dynamics Simulations - Elementary Methods*, New York: John Wiley & Sons.

Heffelfinger, G. S. & van Swol, F. (1994). Diffusion in Lennard-Jones fluids using dual control volume grand canonical molecular-dynamics simulation (DCV-GCMD). *Journal Chemical Physics*, 100 (10), 7548-7552.

Hill, T. L. (1962) *An introduction to statistical thermodynamics*. London: Addison-Wesley publishing company.

Hirschfelder, J. O., Curtiss, C. F. & Bird, R. B. (1954). *Molecular Theory of Gases and Liquids*. New York: John Wiley & Sons, Inc.

Hecht, C. E. (1990). *Statistical thermodynamics and kinetic theory*. New York: Freenan and Company.

Heung, L. K. (2003). Separation Membrane Development, Annual Report to the Department of Energy (US).

Heuchel, M., Davis, G. M., Buss, E. & Seaton, N. A. (1999). Adsorption of carbon dioxide and methane and their mixtures on an activated carbon: simulation and experiment. *Langmuir*, 15 (), 8695.

Kärger, J. & Ruthven, D. M. (1992). *Diffusion in Zeolites and Other Microporous Solids*. New York: John Wiley & Sons, Inc.

Karimi, I. A. & Farooq, S. (2000). Effect of sorbate-sorbate interaction on micropore diffusion in steady-state adsorption processes. *Chemical Engineering Science*, 55, 3529-3541.

Kapteijn, F., Moulijn, J. A. & Krishna, R. (2000). The generalized Maxwell-Stefan model for diffusion in zeolites: sorbate molecules with different saturation loading. *Chemical Engineering Science*, 55 (15), 2923-2930.

Krishna, R. (1990). Multicomponent surface diffusion of adsorbed species: A description based on the generalized Maxwell-Stefan equations. *Chemical Engineering Journal*, 45 (7), 1779-1791.

Krishna, R. (1992). Problems and Pitfalls in the use of the Fick formulation for interparticule diffusion. *Chemical Engineering Science*, 48 (5), 845-861.

Krishna, R. (1993). A unified approach to the modelling of interparticle diffusion in adsorption processes. *Gas Separation & Purification*, 7 (2), 91-104.

Krishna, R. & van den Broeke, L. J. P. (1995). The Maxwell-Stefan description of mass transport across zeolite membranes. *Chemical Engineering Journal*, 57, 155-162.

Koresh, J. E. & Soffer, A. (1987). The carbon molecular sieve membranes. General properties and the permeability of CH_4/H_2 mixture. *Separation Science and Technology*, 22 (2&3), 973-982.

Lide, D. R. & Kehiaian, H. V. (1994). *CRC Handbook of Thermophysical and Thermochemical Data*. London:CRC Press.

Liu, H. & Seaton, N. A. (1994). Determination of the connectivity of porous solids from nitrogen sorption measurements – III. Solids containing large mesopores. *Chemical Engineering Science*, 49 (11), 1869-1878.

Levenspiel, O. (1984). *Engineering flow and heat exchange.* New York: Pelum Press.

López-Ramón, M., Jagiello, J., Bandosz, T. J. & Seaton, N. A. (1997). Determination of the pore size distribution and network connectivity in microporous solids by adsorption measurements and monte carlo simulation. *Langmuir*, 13 (16), 4435-4445.

MacElroy, J. M. D. (1994). Nonequilibrium Molecular-Dynamics simulation of diffusion and flow in thin microporous membranes. *Journal Chemical Physics*, 101 (15), 5274-5280.

MacElroy, J. M. D. (2000). Computer simulation of diffusion within and through membranes. *Korean Journal of Chemical Engineering*, 17 (2), 129-142.

MacElroy, J. M. D. & Boyle, M. J. (1999). A non-equilibrium molecular dynamics simulation of a model carbon membrane separation of CH_4/H_2 mixtures. *Chemical Engineering Journal*, 74 (1-2), 85-97.

MacElroy, J. M. D., Seaton, N. A. & Friedman, S. P. (1997). Sorption rate processes in carbon molecular sieves, *Equilibria and Dynamics of Gas Adsorption on Heterogeneous Solid Surfaces*, 104, 837-880.

Mason, E. A. & Malinauskas, A. P. (1983). *Gas Transport in Porous Media: The Dusty-Gas Model.* Amsterdam: Elsevier.

Mason, E. A. & Viehland, L. A (1978). Statistical-mechanical theory of membrane transport for multicomponent systems: Passive transport through open membranes. *Journal of Chemical Physics,* 68 (8), 3562-3573.

McQuarrie,, D. A. (1976). *Statistical mechanics*. New York: Harper and Row.

Metroplis, N., Rosenbluth, A. W., Rosenbluth, M. N., Teller, A. H. & Teller, E. (1953) Equation of state calculations by fast computing machines. *Journal of Chemical Physics*, 21, 1087.

Nicholson, D. (1997). The transport of adsorbate mixtures in porous materials: basic equations for pores with simple geometry. *Journal of Membrane Science*, 129 (2), 209-219.

Nicolson, D. (1998a). Computer modelling of adsorbate transport in nanospaces. *Supramolecular Science*, 5, 275-280.

Nicholson, D. (1998b). Simulation studies of methane transport on model graphite micropores. *Carbon*, 26 (10), 1511-1531.

Nicolson, D. & Cracknell R. (1996). A transition in the diffusivity of adsorbed fluid through micropores. *Langmuir*, 12 (16), 4050-4052.

Nicholson, D. & Parsonage, N. G. (1982). *Computer simulation and the statistical mechanics of adsorption*. London: Academic Press.

Nosé, S. (1984a). A molecular dynamics method for simulation in the canonical ensemble. *Molecular Physics*, 52, 255-268.

Nosé, S. (1984b). A unified formulation of the constant temperature molecular dynamics method. *Journal of Chemical Physics*, 81, 511-519.

Onsager, L. (1931a). Reciprocal relations in irreversible processes I. *Physical Reviews*, 37 (4), 405-426.

Onsager, L. (1931b). Reciprocal relations in irreversible processes II. *Physical Reviews*, 38 (12), 2265-2279.

Press, W. P., Flannery, B. P., Teukolsky, S. A. & Vetterling, W. T. (1986). *Numerical Recipes – The art of scientific computing*. London: Cambridge University Press.

Peng, D. Y. & Robinson, D. B. (1976). A new two-constant equation of state. *Industrial & Engineering Chemistry Fundamentals*, 15 (1), 59-64.

Rao, M. B. (1991). Diffusion through carbon micropores – 4 years later. *Carbon*, 29 (6), 813-815.

Rao, M. B. & Sircar, S. (1993a). Nanoporous carbon membrane for gas separation. *Gas Separation & Purification*, 7 (4), 279-284.

Rao, M. B. & Sircar, S. (1993b). Nanoporous carbon membranes for separation of gas mixtures by selective surface flow. *Journal Membrane Science*, 85 (3), 253-264.

Rao, M. B. & Sircar, S. (1995). Performance and pore characterization of nanoporous carbon membranes for gas separation. *Journal Membrane Science*, 110 (1), 109-118.

Rao, M. B. & Sircar, S. (1996). Performance and pore characterisation of nanoporous carbon membranes for gas separation. *Journal Membrane Science*, 110 (1), 09-118.

Rao, M. B., Sircar, S. & Golden, T. C. (1992). Gas separation by adsorbent membranes. US Patent 5,104,425.

Rao, M. B., Sircar, S. & Golden, T. C. (1995). Method of making composite porous carbonaceous membranes. US Patent 5,431,864.

Reid, R. C., Prausnitz, J. M. & Toling, B. E. (1987). *The Properties of Gases & Liquids*. New York: McGraw-Hill, Inc.

Rouqerol, F., J., Rouquerol & K., Sing (1999). *Adsorption by Powders and Porous Solids: Principles, Methodology and Applications*, London: Academic Press.

Ruthven, D. M. (1984). *Principles of adsorption and adsorption processes*. New York: John Wiley.

Sahimi, M. (1994). *Applications of percolation theory*. London: Taylor & Francis.

Sandler, S. I. (1999). *Chemical and Engineering Thermodynamics*. London: John Wiley & Sons.

Seader, J. D. & Henley, E. J. (1998). *Separation process principles*. New York: John Wily.

Seaton, N. A. (1991). Determination of the connectivity of porous solids from nitrogen sorption measurements. *Chemical Engineering Science*, 46 (8), 1895-1909.

Seaton, N. A., Friedman, S. P., MacElroy, J. M. D. & Murphy, B. J. (1997). The molecular sieving mechanism in carbon molecular sieves: A molecular dynamics and critical path analysis. *Langmuir*, 13 (5), 1199-1204.

Sedigh, M. G., Xu, L., Tsotsis, T. T. & Sahimi, M. (1999). Transport and morphological characteristics of polytherimide-base carbon molecular sieve membrane. *Industrial and Engineering Chemistry Research*, 38 (9), *3367-3380.*

Seo, Y. G., Kum, G. H. & Seaton, N. A. (2002a). Monte Carlo simulation of transport diffusion in nanoporous carbon membranes. *Journal Membrane Science*, 195 (1), 65-73.

Seo, Y. G., Kum, G. H. & Seaton, N. A. (2002b). Simulation of transport diffusion of hydrogen and alkanes in nanoporous carbon membranes using united-atom model. *Proceedings for the Fundamentals of Adsorption 7*, Japan, 385-392.

Shusen, W., Meiyun, Z. & Zhizhong, W. (1996). Asymmetric molecular sieve carbon membranes. *Journal of Membrane Science*, 109 (2), 267-270.

Sircar, S. (1991). Influence of adsorbate size and adsorbent heterogeneity on IAST. *A.I.Ch.E. Journal*, 41 (5), 1135-1145.

Sircar, S. & Golden, T. C. (2000). Purification of hydrogen by pressure swing adsorption. *Separation Science and Techonoly*, 35 (5), 667-687.

Sircar, S., Rao, M. B. & Thaeron, C. M. A. (1999). Selective surface flow membrane for gas separation. *Separation Science and technology*, 34, 2081-2093.

Smit, B. (1995). Grand canonical monte carlo simulations of chain molecules: adsorption isotherms of alkanes in zeolites. *Molecular Physics*, 85 (1), 153-172.

Soffer, A., Koresh, J. E. & Saggy, S. (1987). Separation device. US Patent 4,685,940.

Steele, W. A. (1974). *The interactions of gases with solid surfaces*. Oxford: Pergamon.

Swope, W. C., Andersen, H. C., Berens, P. H. & Wilson, K. R. (1982). A computer simulation method for the calculation of equilibrium constants for the formation of physical clusters of molecules: application to small water clusters. *Journal Chemical Physics*, 76 (1), 637-649.

Taylor, R. & Krishna, R. (1993). *Multicomponent Mass Transfer*. New York: John Willey & Sons, Inc.

Travis, K. P. & Gubbins, K. E. (2000). "Transport diffusion of oxygen-nitrogen mixtures in graphite pores: a NEMD study", *Langmuir*, 15, 6050-6059.

Thompson, A. P., Ford D. M. & Heffelfinger, G. S. (1998). Journal of Chemical Physics, 109, 6406-6414.

Toxvaerd, S. (1990). Molecular dynamics calculations of the equation of state of alkanes. *Journal of Chemical Physics*, 93 (6), 4290-4295.

Verlet, L. (1967). Computer "Experiments" on Classical Fluids. I. Thermodynamical Properties of Lennard-Jones Molecules. *Physical Review,* 159 (1-5), 98-103

Yang, R. T. (1987). *Gas separation by adsorption processes*. London: Butterworths.

Wesselingh, J. A. & Krishna, R. (1992). The Maxwell-Stefan approach to mass transfer. *Chemical Engineering Science*, 52, 861-911.

Wesselingh, J. A. & Krishna, R. (2000), *Mass Transfer in Multicomponent Mixtures*. Delft: Delft University Press.

Whysall, M. & Picioccio, K. W. (1999). Selection and revamp of hydrogen purification processes. Presented at the AIChE Spring Meeting, Houston (Texas).